UNIVERSIDADE ESTADUAL DE CAMPINAS
Faculdade de Engenharia Elétrica e de Computação

Ruby Stella Bravo Ospina

Impact of Laser Imperfections on Coherent Optical Receivers with High-Order Modulation Formats

Impacto de Imperfeições do Laser em Receptores Ópticos Coerentes com Formatos de Modulação de Alta Ordem

Campinas

2018

UNIVERSIDADE ESTADUAL DE CAMPINAS
Faculdade de Engenharia Elétrica e de Computação

Ruby Stella Bravo Ospina

Impact of Laser Imperfections on Coherent Optical Receivers with High-Order Modulation Formats

Impacto de Imperfeições do Laser em Receptores Ópticos Coerentes com Formatos de Modulação de Alta Ordem

Dissertation presented to the School of Electrical and Computer Engineering of the University of Campinas in partial fulfillment of the requirements for the Master's degree in Electrical Engineering, in the area of Telecommunications and Telematics.

Dissertação apresentada à Faculdade de Engenharia Elétrica e de Computação da Universidade Estadual de Campinas como parte dos requisitos exigidos para a obtenção do título de Mestra em Engenharia Elétrica, na Área de Telecomunicações e Telemática.

Supervisor: Prof. Dr. Darli Augusto de Arruda Mello

Este exemplar corresponde à versão final da tese defendida pela aluna Ruby Stella Bravo Ospina, e orientada pelo Prof. Dr. Darli Augusto de Arruda Mello

Campinas

2018

Agência(s) de fomento e nº(s) de processo(s): CAPES; FUNCAMP

Ficha catalográfica
Universidade Estadual de Campinas
Biblioteca da Área de Engenharia e Arquitetura
Luciana Pietrosanto Milla - CRB 8/8129

B739i

Bravo Ospina, Ruby Stella, 1992-
Impact of laser imperfections on coherent optical receivers with high-order modulation formats / Ruby Stella Bravo Ospina. – Campinas, SP : [s.n.], 2018.

Orientador: Darli Augusto de Arruda Mello.
Dissertação (mestrado) – Universidade Estadual de Campinas, Faculdade de Engenharia Elétrica e de Computação.

1. Comunicações ópticas. 2. Processamento digital de sinais. 3. Lasers semicondutores. I. Mello, Darli Augusto de Arruda, 1976-. II. Universidade Estadual de Campinas. Faculdade de Engenharia Elétrica e de Computação. III. Título.

Informações para Biblioteca Digital

Título em outro idioma: Impacto de imperfeições do laser em receptores ópticos coerentes com formatos de modulação de alta ordem
Palavras-chave em inglês:
Optical communications
Digital signal processing
Semiconductor lasers
Área de concentração: Telecomunicações e Telemática
Titulação: Mestra em Engenharia Elétrica
Banca examinadora:
Darli Augusto de Arruda Mello [Orientador]
Marcelo Luís Francisco Abbade
Evandro Conforti
Data de defesa: 27-04-2018
Programa de Pós-Graduação: Engenharia Elétrica

COMISSÃO JULGADORA - DISSERTAÇÃO DE MESTRADO

Candidato: Ruby Stella Bravo Ospina RA: 163653

Data da Defesa: 27 de abril de 2018

Título da Tese: "Impact of Laser Imperfections on Coherent Optical Receivers with High-Order Modulation Formats (Impacto de Imperfeições do Laser em Receptores Ópticos Coerentes com Formatos de Modulação de Alta Ordem)".

Prof. Dr. Darli Augusto de Arruda Mello (Presidente, FEEC/UNICAMP)

Prof. Dr. Marcelo Luís Francisco Abbade (UNESP)

Prof. Dr. Evandro Conforti (FEEC/UNICAMP)

A ata de defesa, com as respectivas assinaturas dos membros da Comissão Julgadora, encontra-se no processo de vida acadêmica do aluno.

To my parents Luis and Rubiela.
To my sisters Claudia, Diana and Ana.
To my nephews Jose, Felipe, Samuel, and Santiago.

Acknowledgements

"But by the grace of God I am what I am, and his grace toward me was not in vain. On the contrary, I worked harder than any of them, though it was not I, but the grace of God that is with me". (1 Corinthians 15:10).

In the first place, I want to express my infinite gratitude to my parents, Luis and Rubiela two wonderful people who always have been my engine, my strength, and my support. I thank my sisters Claudia, Diana, and Ana for being my accomplices and confidants together with my loved nephews who are my inspiration. I would like to thank emotionally my godmother Milta Chacón for her perseverance, confidence and love for me. A deep feeling of gratitude for my advisor Dr. Darli A. Mello whose help was totally valuable during my Master's degree. Thank so much to the professor Dr. Dalton Soares for his academic and emotional support. I wish to thank Claudio, Melissa, and Yalena for their unconditional friendship and my laboratory's colleagues for welcoming me, helping me, and motivating me every day. I thank Dr. Jacklyn Dias Reis for his intellectual contribution. Finally, I will always take gratitude for the University of Campinas and for the BrPhotonics company for allowing to go through one of the best experiences of my life.

Vive como si fueras a morir mañana. Aprende como si fueras a vivir para siempre.
Mahatma Gandhi.

Abstract

Currently, coherent optical systems transmit large volumes of information thanks to the use of high-order modulation formats. However, such modulation formats are more susceptible to phase perturbations generated by imperfections in the lasers used in the transmitter and receiver. This work focused on an analysis of laser imperfections and their impact on the performance of coherent optical receivers with high-order modulation formats. In particular, the two main sources of phase perturbations were evaluated: laser phase noise and fluctuations in the operating frequency, an effect known as carrier frequency jitter. First, the impact of laser imperfections was evaluated by simulations. Phase noise was modeled as a Wiener process, and frequency jitter was assumed to be sinusoidal. The results allowed to evaluate the behavior of the system under different conditions of frequency and amplitude of the jitter signal. Later, the impact of phase perturbations was evaluated through experiments. It was observed that the laser linewidth calculated by existing methods is not sufficient to predict the behavior of the digital signal processing algorithms under intense jitter conditions. Alternatively, the work suggested a more convenient methodology for predicting the impact of laser perturbations on system performance, which takes into account the composition of phase noise and carrier frequency jitter.

Keywords: coherent optical systems; phase noise; phase perturbations; carrier frequency jitter; sinusoidal frequency jitter; linewidth estimation; digital signal processing.

Resumo

Atualmente, os sistemas ópticos coerentes transmitem grandes volumes de informação graças à utilização de formatos de modulação de alta ordem. No entanto, esses formatos de modulação são mais suscetíveis a perturbações de fase geradas por imperfeições nos lasers utilizados no transmissor e receptor. Este trabalho centrou-se em uma análise das imperfeições do laser e seu impacto sobre o desempenho de receptores ópticos coerentes com formatos de modulação de alta ordem. Em especial, avaliaram-se as duas fontes principais de perturbações de fase: o ruído de fase do laser e as flutuações na frequência de operação, efeito conhecido como jitter de frequência da portadora. Primeiramente, investigou-se o impacto das imperfeições do laser por meio de simulações. O ruído de fase foi simulado como um processo discreto de Wiener, e o jitter de frequência foi modelado como uma forma de onda senoidal. Os resultados permitiram avaliar o comportamento do sistema sob diversas condições de frequência e amplitude do sinal de jitter. Posteriormente, o impacto das perturbações de fase foi avaliado por meio de experimentos. Observou-se que parâmetro de largura de linha calculado por métodos existentes não é suficiente para prever o comportamento dos algoritmos de processamento digital de sinais sob condições intensas de jitter. Alternativamente, o trabalho sugeriu uma metodologia mais conveniente para prever o impacto das perturbações do laser no desempenho do sistema, que leva em consideração a composição de ruído de fase e jitter de frequência.

Palavras-chaves: sistemas ópticos coerentes; ruído de fase; perturbações de fase; jitter de frequencia da portadora; jitter de frequência senoidal; estimação de largura de linha, processamento digital de sinais.

Acronyms

ADC - Analog to digital converter.

AOM - Acousto-optic modulator.

ASE - Amplified spontaneous emission noise.

AWGN - Additive white Gaussian noise.

BER - Bit error rate.

BFS - Blind frequency search.

BPS - Blind phase search.

BPSK - Binary phase shift keying.

CD - Chromatic dispersion.

CFJ - Carrier frequency jitter.

CM - Constant modulus.

CMA - Constant modulus algorithm.

CMMA - Second multimodulus algorithm.

CPR - Carrier phase recovery.

DAC - Digital to analog converter.

DC - Direct current.

DCF - Dispersion compensating fibers.

DFB - Distributed feedback lasers.

DGD - Differential group delay.

DPLL - Digital phase-locked loop.

DSHI - Delayed self-homodyne interferometer.

DSHO - Delayed self-homodyne.

DSHT - Delayed self-heterodyne.

DSP - Digital signal processing.

DUT - Device under test.

ECL - External cavity lasers.

EDFA - Erbium doped fiber amplifiers.

FB - Fabry-Perot.

FDE - Frequency domain equalizer.

FEC - Forward error correction.

FFT - Fast Fourier transform.

FIR - Finite impulse response.

FM - Frequency modulation.

FWHM - Full width at half maximum.

FWM - Four wave mixing.

GSOP - Gram-Schmidt orthogonalization procedure.

GVD - Group-velocity dispersion.

ISI - Intersymbol interference.

IQM - In-phase and quadrature modulator.

LASER - Light amplification by stimulated emission of radiation.

LMS - Least-mean-square.

MA - Moving average.

MASER - Optical microwave amplification by stimulated emission of radiation.

MCA - Modified constant modulus algorithm.

MLM - Multi-longitudinal mode.

MMA - Multimodulus algorithm.

MSDE - Minimum mean square distance error.

MSR - Mode-suppression ratio.

MZM - Mach-Zehnder modulator.

NL - Noise loading.

OOK - On-off keying.

OSNR - Optical signal-to-noise ratio.

PBS - Polarization beam splitter.

PCS - Polarization beam combiner.

PC - Polarization controller.

PDL - Polarization dependent loss.

PM - Polarization multiplexing.

PMD - Polarization mode dispersion.

PMF - Polarization maintaining fibers.

PSD - Power spectral density.

QAM - Quadrature amplitude modulation.

QI - Quadrature imbalance.

QPSK - Quadrature phase shift keying.

RDE - Radius directed equalization.

RLS - Recursive least-square.

SLM - Single-longitudinal mode.

SPM - Self phase modulation.

SNR - Signal-to-noise ratio.

SSMF - Standard single mode fiber.

S-BPS - Symmetric blind phase search.

TDE - Time domain equalizer.

TIA - Transimpedance amplifier.

VCSEL - Vertical-cavity surface-emitting lasers.

VV - ViterbiViterbi.

WDM - Wavelength division multiplexing.

XPM - Cross phase modulation.

Symbols

$\alpha_{roll-off}$ - Excess bandwidth parameter.

V_{π} - External tension for π radians delay.

P_{outMod} - Output power of the optical modulator.

P_{inMod} - Input power of the optical modulator.

H - Transference function of 3 dB coupler.

$E(t)$ - Electrical field.

I_p - Photo-current.

R - Responsivity factor of a photo-detector.

P_{inpd} - Input power to photo-detector.

η - Conversion efficiency.

q - Electron charge.

h - Plank constant.

c - Speed of light.

$i_Q(t)$ - Current quadrature component.

$i_I(t)$ - Current in-phase component.

$E_r(t)$ - Electrical field of the received signal.

$E_{Lo}(t)$ - Electrical field of the local oscillator signal.

$A_s(t)$ - Optical signal amplitude.

$A_{Lo}(t)$ - Local oscillator signal amplitude.

ϕ_s - Optical signal phase.

ω_o - Angular frequency of the optical carrier.

ω_{Lo} - Angular frequency of the local oscillator signal.

η_s - Complex Gaussian noise of the optical signal.

η_{Lo} - Complex Gaussian noise of the local oscillator signal.

$\Re(.)$ - Real part.

$(.)^*$ - Complex conjugate.

Z - Complex numbers set.

ω_{IF} - Intermediate angular frequency.

P_{av} - Average optical power.

α - Attenuation coefficient.

z - Propagation distance.

P_{in} - Power launched at the fiber input.

P_{Out} - Power at the fiber output.

L - Fiber length.

$\Delta\omega$ - Spectral linewidth of a transmitted pulse.

T - Time delay of a spectral component.

v_g - Group velocity.

β - Propagation constant.

$\bar{n}$ - Effective index.

ΔT - Time of pulse broadening.

β_2 - Group-velocity dispersion parameter.

$\Delta\lambda$ - Range of wavelengths emitted by the optical source.

λ - Wavelength.

D - Dispersion parameter.

$E1$ - Atomic ground state.

$E2$ - Atomic excited state.

$S_{sp}(v)$ - Spectral density of spontaneous-emission-induced noise.

ν - Optical frequency.

n_{sp} - Spontaneous emission factor.

$N1$ - Atomic populations for the ground state.

$N2$ - Atomic populations for the excited state.

P_T - Total power of the signal in both polarization.

B_{ref} - Reference bandwidth for OSNR calculation.

E_s - Total signal energy.

$No/2$ - Noise spectral density.

$erfc$ - Complementary error function.

M - Modulation index.

p - Number of polarization modes.

R_s - Symbol rate.

L_b - Beat length.

$\Delta\beta$ - Difference between propagation constants of the two polarization states.

$\Delta\tau$ - Differential group delay.

P_{PMD} - Polarization mode dispersion parameter.

$\mathbf{J}$ - Jones Matrix.

σ^2 - Variance.

$E(.)$ - Expected value.

$E_{R,X}$ - Electric field of the signal received in polarization X.

$E_{R,Y}$ - Electric field of the signal received in polarization Y.

$E_{R,X}$ - Electric field of the signal transmitted in polarization X.

$E_{R,Y}$ - Electric field of the signal transmitted in polarization Y.

Δ_f - Frequency offset between transmitter laser and local oscillator laser.

$s(k)$ - Transmitted signal in discrete time.

$\theta(k)$ - Phase noise signal in discrete time.

$w(k)$ - Additive white Gaussian noise in discrete time.

Δ_Φ - Frequency offset-induced phase offset.

T_{sa} - Time between samples.

T_s - Symbol period.

T_{DSP} - Time period in DSP algorithms.

Δ_{F1} - Fixed frequency offset between transmitter and local oscillator lasers.

Δ_A - Peak-to-Peak amplitude of the carrier frequency jitter.

f_A - Oscillation frequency of the carrier frequency jitter.

Δ_k, Δ_m - Gaussian random variables.

Δ_ν - Sum of the transmitter laser linewidth and local oscillator laser linewidth.

$(.)^H$ - Hermitian operator.

$(.)^T$ - Transpose operator.

ξ_{Godard} - Godard cost function.

e_{Godard} - Godard error signal.

μ - Equalizer update step size.

ε - Error signal.

μ_f - Convergence parameter.

E_{Ave} - Constellation average energy.

$argmin(.)$ - Minimum argument.

$arg(.)$ - Argument function.

$\hat{()}$ - Estimate.

$Decision(.)$ - Hard-decision rules.

$floor(.)$ - Floor function.

$ceil(.)$ - Ceil function.

$UN(.)$ - unwrapping operation.

$mod(.)$ - Modulus operation.

f_k - Resonant frequencies of a fabry-perot filter.

n - Cavity refractive index.

l - Cavity length.

Λ - Grating period.

m - Order of Bragg diffraction.

λ_B - Bragg wavelengths.

δ_f - Spacing between resonant frequencies of a FP cavity.

$\Gamma_{EE}(\tau)$ - Optical field-autocorrelation function.

$<>$ - Expectation operator.

τ - Time delay.

Δ_{LW} - Lorentzian spectral linewidth.

β_c - Linewidth enhancement factor.

I - Laser average intensity.

P - Laser output power.

α_m - Facet loss.

g - Cavity gain .

α_L - Waveguide loss.

r_m - Facet reflectivity.

S_k^{tx} - Carrier signal of transmitter laser.

S_k^{LO} - Carrier signal of local oscillator.

ϕ_J - Phase shift between transmitter and local oscillator jitters.

$\Phi(t)$ - Laser phase noise in continuous time.

τ_d - Delay time introduced by delay fiber.

Ω - Frequency shift.

E_d - Detected field in TIA output.

$var(.)$ - Variance calculation.

$\mathfrak{F}(.)$ - Fourier transform.

$mean(.)$ - Average calculation.

ζ - Experimental phases sequence.

List of Figures

List of Tables

Contents

1 INTRODUCTION

1.1 CONTEXTUALIZATION

Currently, advanced coherent optical systems play a prominent role in the field of wired digital communications. Due to their efficiency and very high information capacity, they are able to transmit vast amounts of data at long distances with high system performance. For many years, direct detection optical systems supported the traffic demands using simple on-off keying (OOK) as modulation format. However, the massive increase in worldwide data flow, brought about by the increase in IP services and video streaming, has challenged the current (and expensive) telecommunication infrastructure. Therefore, advanced systems that are able to work under the current infrastructure are demanded, not just for longer link reaches, but also for higher transmission capacities. Ideally, it is necessary to drastically increase the capacity of optical systems without losing the huge investments in current infrastructure. The most convenient alternative to reach this goal is to raise the system spectral efficiency by incorporating high-order modulation formats, such as quadrature phase shift keying (QPSK) and quadrature amplitude modulation (QAM). These techniques are able to send a higher number of bits in a given spectral range when compared to the common OOK. Consequently, they are able to increase the bit transmission rate without increasing of the required bandwidth, or able to decrease the symbol rate (and therefore the required bandwidth) while maintaining the bit rate. Naturally, intermediate configurations between these two extremes are also possible.

The detection process of phase-modulated signals requires a considerable amount of computational effort and has to be carried out by means of a coherent detector. For this reason, innovations like wavelength division multiplexing (WDM), erbium doped fiber amplifiers (EDFA) and dispersion compensating fibers (DCF) have been implemented for maintaining the low complexity of OOK systems, since these approaches enhance the capacity and the link reach without the need of drastic changes in the receiver architecture (FARJADY; PARKER, 2002), (DESURVIRE *et al.*, 1991), (RAMACHANDRAN, 2007). Nevertheless, in reality, the information transmission requirements have been growing in such a way that the use of high-order modulation and coherent detection methods are mandatory to keep up with the exponential increase in Internet traffic.

Coherent detection is based on a coherent combination between the received modulated signal and a reference signal derived from a local oscillator through an optical-

to-electrical conversion device. Equally important is a subsequent digital signal processing (DSP) stage, which is incorporated for compensating fiber impairments. This kind of receiver brings important benefits into the system. First, it increases the optical receiver sensitivity which, by itself, allows for greater link span losses. Second, it enables the use of more spectrally efficient modulation formats. Finally, instead of implementing costly physical impairment compensation devices, coherent detection allows for significant digital signal processing gains. Such improvements embody DSP compensations for several transmission impairments, such as chromatic dispersion (CD), polarization mode dispersion (PMD), carrier signal offsets, spectrum narrowing, etc. (ZHANG, 2012). It should be emphasized, however, that coherent reception produces some additional impairments, which have to be compensated by specific DSP algorithms. Carrier phase noise, which is one of the most representative of these impairments, arises due to the non-monochromatic nature of the employed lasers. Phase noise appears as a random symbol phase variation that can result in a total reference loss of the quadrature and in-phase received components with respect to the transmitted constellation. Nevertheless, efficient DSP carrier recovery algorithms are able to restore the correct symbol phases before the decision stages.

The phase noise intensity is higher for wider linewidth lasers. Therefore, intense research efforts are focused on developing narrow-linewidth lasers in an attempt to raise the performance of phase-noise-sensitive systems. The need for narrow-linewidth lasers challenges manufacturers not just in the fabrication processes but also in the laser characterization. A new generation of narrow linewidth lasers requires more accurate measurement techniques, in consequence, a vast literature about semiconductor lasers characterization can be found. For instance, the work in (OKOSHI *et al.*, 1980) introduces a novel method able to increase the resolution of the existing linewidth estimation mechanisms. Here, the technique receives the name of delayed self-homodyne interferometer (DSHI) and the results show how a 50-kHz resolution can be obtained. Later, (TSUCHIDA, 1990) proposes an improvement on the DSHI. It is shown that a resolution increment can be obtained by the inclusion of a recirculating delay that allowed the same fiber segment to be used multiples times. However, the large losses limit the method contributions. In (DAWSON *et al.*, 1992), a new approach called the recirculating delayed self-heterodyne interferometer with loss compensation was developed, in order to relieve the limitations of the setup proposed in (TSUCHIDA, 1990). Other important techniques have been developed (LUDVIGSEN *et al.*, 1998), (KIM *et al.*, 1999), (DUTHEL *et al.*, 2009), (CHEN *et al.*, 2011), (MAHER; THOMSEN, 2011), (HUYNH *et al.*, 2012), (KOJIMA *et al.*, 2015), (SUTILI *et al.*, 2016), all with the target of providing robust techniques that allow estimating narrow linewidths for an accurate semiconductor laser characterization.

A second source of phase perturbation originates from the frequency deviation between the two lasers, which adds a phase shift between consecutive samples that is proportional to itself. Theoretically, this frequency drift is slowly varying, in which case the phase effects are compensated in two stages, consisting of frequency recovery, followed by a carrier phase recovery. In practical implementations, the inevitable mechanical vibrations modify the laser oscillation frequencies, resulting in a random variable for the frequency offset, (SELMI *et al.*, 2009), (HOFFMANN *et al.*, 2008a) a phenomenon which is known as carrier frequency jitter (CFJ). It has been recently shown that laser frequency variations caused by mechanical disturbances significantly degrade the performance of feedforward carrier phase recovery (CPR) algorithms (GIANNI *et al.*, 2011). Consequently, in order to avoid such degradations, the frequency offset should be compensated before the CPR block. Frequency fluctuations have been modeled as a low frequency sinusoid (KUSCHNEROV *et al.*, 2010), (PIYAWANNO *et al.*, 2010), (GIANNI *et al.*, 2013), an assumption that was supported by experimental measurements in (FERREIRA, 2017). However, in other laser architectures, different waveforms can be observed.

In (QIU *et al.*, 2013), a low complexity frequency recovery algorithm for tracking the frequency offset over time is proposed. Here, CPR is implemented by means of a digital phase-locked loop (DPLL) method. The suggested algorithm is evaluated in both serial and parallel contexts for QPSK and 16-QAM. The simulation results show that the described algorithm is capable of effectively compensating the frequency offset fluctuations. In (KUSCHNEROV *et al.*, 2010) and (PIYAWANNO *et al.*, 2010), the Viterbi&Viterbi (V&V) and DPLL performances against frequency offset drift are evaluated in a polarization multiplexing (PM) context for PM-QPSK and PM-16-QAM, respectively. The work in (GIANNI *et al.*, 2011) presents two carrier recovery architectures for QPSK, denoted as S-DPLL+VV and P-DPLL+VV, consisting in a serial DPLL and a parallel DPLL, respectively for frequency offset drift compensation and the V&V as phase recovery method for both cases. In (GIANNI *et al.*, 2013) the previous scheme is extended for 16-QAM.

1.2 CONTRIBUTIONS

This thesis first evaluates the impact of both phase noise and CFJ on the performance of high-order QAM systems by simulation. Phase noise is modeled as a discrete Wiener process, and CFJ is simulated as a sinusoidal waveform. The work reveals the relation between the system performance degradation and the intensity of transceiver imperfections. In a second stage of this thesis, the impact of laser imperfections is carried out from a practical perspective supported by experimental data. Is is shown that current

methods for linewidth estimation fail under intense CFJ levels. To circumvent this problem, we developed a methodology to combine CFJ and phase noise metrics for predicting the DSP performance with improved accuracy.

The rest of this work is structured as follows: Chapter 2 presents the basis of coherent optical systems as well as the main transmission impairments. Chapter 3, explains some semiconductor lasers fundamentals and highlights the phase perturbations generated by laser imperfections. Simulation results are presented in Chapter 4. Chapter 5 focuses on the processing of experimental data. Lastly, Chapter 6 concludes the thesis.

2 COHERENT OPTICAL COMMUNICATION SYSTEMS

A coherent optical communication system is composed of three general blocks, as illustrated in Figure 2.1. The transmitter is a set of optoelectronic devices that converts the information signal into the optical domain for fiber transmission. The physical channel is the optical path composed of optical filters, the optical fiber and amplifiers. The receiver is an arrangement of elements that translates the received signal to the electric domain and compensates eventual transmission impairments. The modules that compose these blocks are described in the following sections.

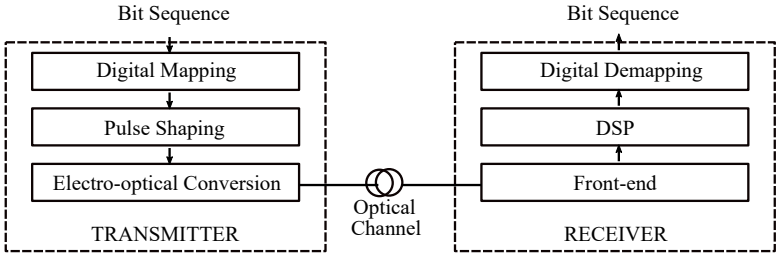

Figure 2.1 – An optical communication system.

2.1 TRANSMITTER

In the transmitter block, firstly, an input bit sequence is mapped into a specific constellation according to the digital modulation format. Then, the corresponding symbol sequence goes through a pulse shaping stage. Later, the electric analog signal modulates an optical carrier, which is injected into the optical fiber for transmission.

2.1.1 Digital mapping

The mapping of a binary sequence into a digital constellation allows increasing the system capacity. Multilevel modulation formats provide a higher spectral efficiency as they convey several bits using only one symbol. In a M-QAM system, with M denoting modulation order, each symbol corresponds to k bits, where k = $\log_2$M. According to (HAYKIN, 2001), the rule that governs the symbol construction is given by:

$$s_i = A_i + jBi \tag{2.1}$$

where $i = 1, 2, 3...M$ points the location of the symbol within the constellation. In Eq. 2.1, j is the imaginary unit and A and B are two integer vectors whose elements depend on the

modulation order. For 4-QAM $A, B \in \{\pm 1\}$, for 16-QAM $A, B \in \{\pm 1, \pm 3\}$, for 64-QAM $A, B \in \{\pm 1, \pm 3, \pm 5, \pm 7\}$ and for 256-QAM $A, B \in \{\pm 1, \pm 3, \pm 5, \pm 7, \pm 9, \pm 11, \pm 13, \pm 15\}$. Figure 2.2 presents the M-QAM constellation for M equal to 4, 16, 64 and 256.

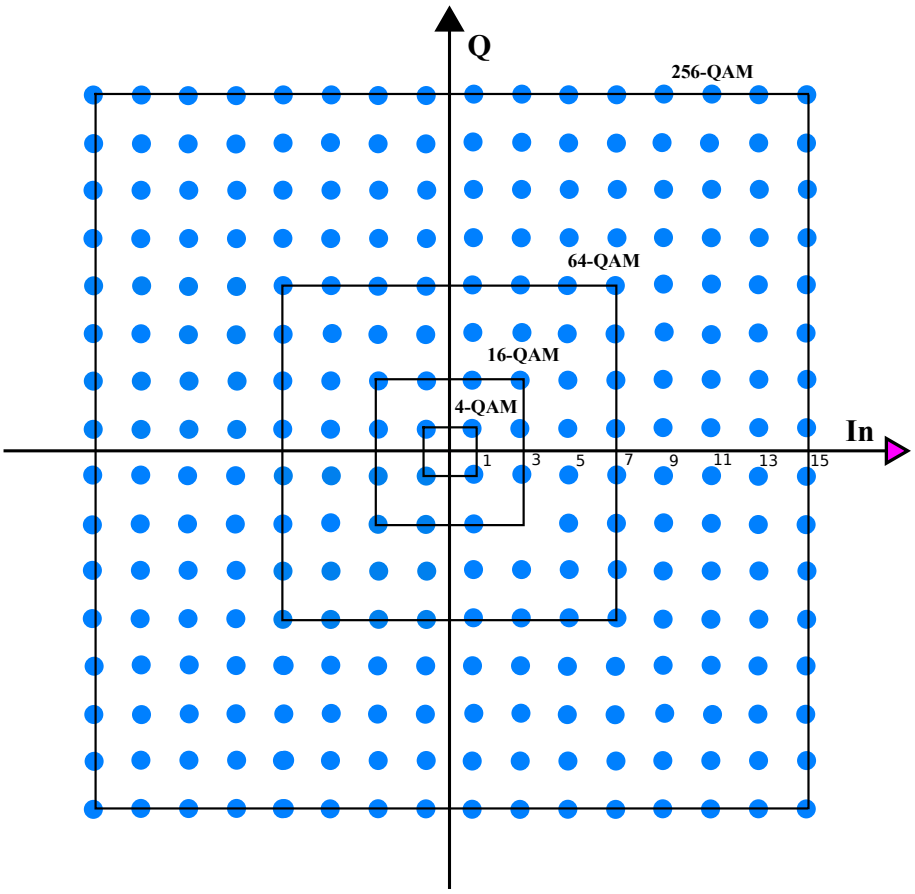

Figure 2.2 – M-QAM constellations.

The increment of the modulation format order raises the system spectral efficiency, nevertheless, the reduction of the distance among symbols makes the system less robust to additive noise and phase perturbations. Usually, the digital mapping is performed through the common Gray mapping, which, when employed in high-order modulation formats, is susceptible to high levels of phase perturbations. An intense phase perturbation can cause a significant rotation in the constellation and give rise to cycle slips (MEYR *et al.*, 1998). In square QAM constellations, the signal is invariant under a rotation of $2\pi/M$. Then, when random data is transmitted, the carrier synchronizer cannot distinguish between an angle θ and an angle θ plus an integer multiple of $2\pi/M$. This limitation produces catastrophic errors at reception as the symbols carry useful information in their phases. A better option for mapping bits to a digital constellation consists in generating a QAM sequence that does not convey information in the phases of the symbols, instead, use the difference of phase between two consecutive symbols. This approach is known as differential encoding. In a differential encoding context, the phase of the n^{th}

symbol is the phase difference between the transmitted symbols in instants $(n+1)$ and n (MEYR *et al.*, 1998). At the receiver, symbols are detected coherently, and the phase of the symbols is obtained as the phase difference between consecutively detected symbols. Figure 2.3 describes the encoding procedure for differential 16-QAM encoding.

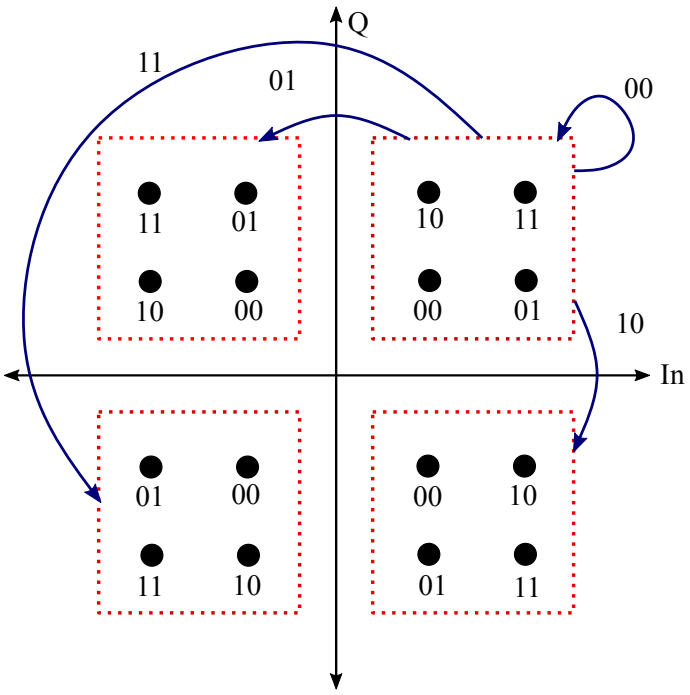

Figure 2.3 – 16-QAM bit to symbol assignment through differential encoding.

The binary sequence is first divided into sets of four bits. To assign to each set a point in the complex plane, the four bits have to be analyzed separately in groups of two. The first two bits indicate the quadrant, and the last two bits designate the position within the quadrant. After quadrant selection, the symbol distribution is carried out as shown in Figure 2.3 (PFAU *et al.*, 2009), (FATADIN *et al.*, 2010). In the 64-QAM case, the procedure is basically the same, nevertheless, the binary sequence is initially divided into groups of six bits. Thus, the first pair of bits defines the quadrant jump, while the last four the position within the quadrant. Figure 2.4 shows the differential encoding for 64-QAM deduced from Figure 2.3. At reception, differential decoding uses the same logic to revert the encoding process, generating the detected binary sequence that is ideally equal to the transmitted one. In general, differential encoding offers a higher robustness against phase perturbations, nevertheless, it causes a system performance penalty because of correlated neighboring errors.

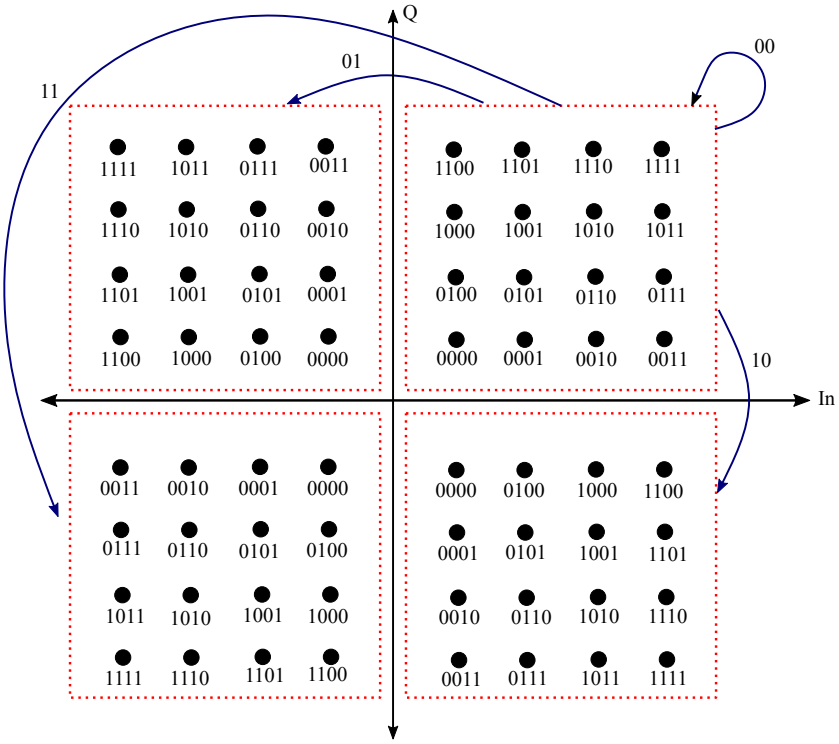

Figure 2.4 – 64-QAM bit to symbol assignment through differential encoding.

2.1.2 Pulse shaping

Once at the mapper output, the symbol sequence passes through a shaping filter. The pulse shaping block allows representing the symbol sequence in an electrical analog signal suitable for electro-optical conversion. There are several pulse shapes, but the highest spectral efficiency is achieved by Nyquist pulses.

2.1.2.1 Nyquist pulse shapes

According to Nyquist, bandwidth-limited systems present a restriction over their symbol transmission rate. The symbol rate of a system with bandwidth W cannot exceed 2W symbols per second without intersymbol interference (ISI) (BARRY *et al.*, 2004). The restriction of a symbol rate to 2W symbols per second is known as Nyquist rate. Thus, the minimum bandwidth required to avoid ISI is half the symbol rate, however, not just any pulse with this bandwidth will do. The pulse spectrum that satisfies the Nyquist criterion is illustrated in Figure 2.5, where T is the symbol period. As the frequency response of the Nyquist pulse is a rectangular waveform, its impulse response is given by:

$$g(t) = \frac{\sin(\pi t/T)}{\pi t/T}, \tag{2.2}$$

and corresponds to the sinc function shown in Figure 2.6. The minimum bandwidth ($W = 1/2T$) is desirable, but the ideal band-limited pulse is impractical. Because of that,

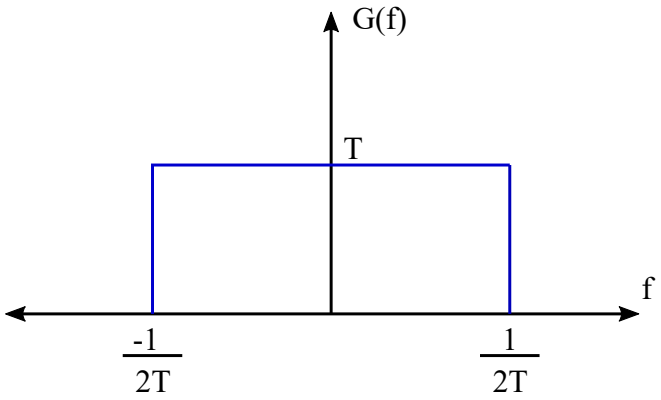

Figure 2.5 – Rectangular Nyquist filter.

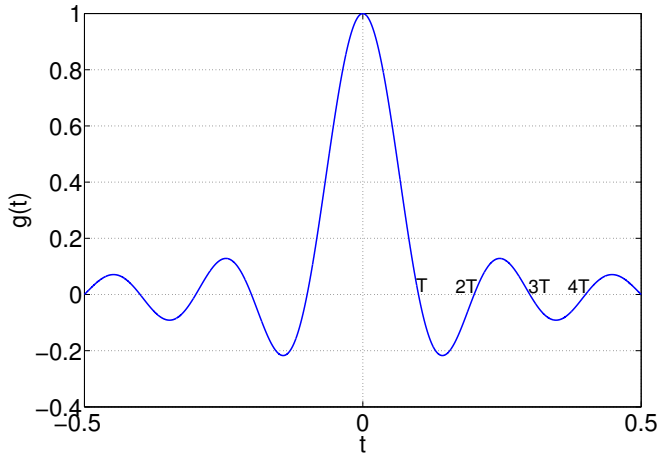

Figure 2.6 – Nyquist pulse in time domain.

new pulse shapes are suggested for practical implementation. This is the case of the raised cosine filter, in which the bandwidth W is larger than its minimum value by a factor of $1 + \alpha_{roll-off}$ as:

$$W = \frac{1 + \alpha_{roll-off}}{2T}, \tag{2.3}$$

where $\alpha_{roll-off}$ is the excess bandwidth parameter or roll-off parameter. For the ideal case, $\alpha_{roll-off} = 0$ and there is no excess-bandwidth. Increasing the excess-bandwidth simplifies implementation but, of course, transmission requires more channel bandwidth. The impulse response of a raised cosine filter is given by (HAYKIN, 2001):

$$g(t) = \left(\frac{\sin(\pi t/T)}{\pi t/T}\right)\left(\frac{\cos(\alpha_{roll-off}\pi t/T)}{1 - (2\alpha_{roll-off}t/T)^2}\right) \tag{2.4}$$

and its frequency response corresponds to:

$$G(f) = \begin{cases} T & \text{for} \quad |f| \leq \frac{1-\alpha_{roll-off}}{2T} \\ T\cos^2\left[\frac{\pi T}{2\alpha_{roll-off}}\left(|f| - \frac{1-\alpha_{roll-off}}{2T}\right)\right] & \text{for} \quad \frac{1-\alpha_{roll-off}}{2T} < |f| < \frac{1+\alpha_{roll-off}}{2T} \\ 0 & \text{for} \quad \frac{1+\alpha_{roll-off}}{2T} < |f|\,. \end{cases} \tag{2.5}$$

Figure 2.7 shows the frequency response of the raised cosine filter for different $\alpha_{roll-off}$ values.

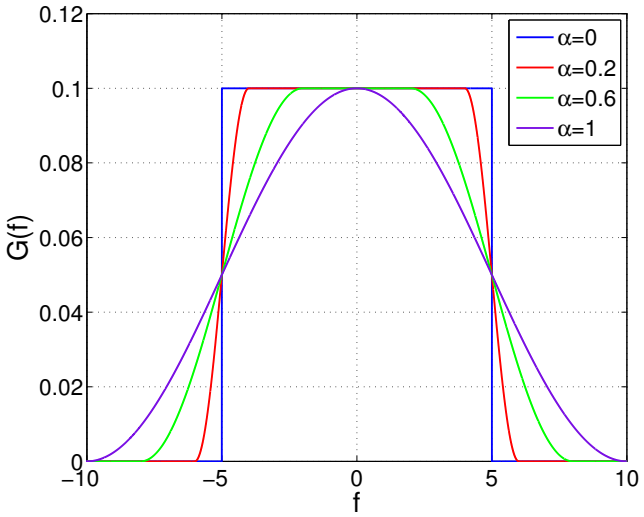

Figure 2.7 – Frequency response of the raised cosine filter.

Raised cosine filters are commonly used in current communications systems, however, the most used configuration to avoid ISI consists in implementing a root raised cosine filter in transmission and a root raised cosine filter as a matched filter at reception. On the other hand, the matched filter can also be implemented by an adaptive filter for tracking the eventual dynamicity of the channel (BARRY *et al.*, 2004).

2.1.3 Electro-optical conversion

Electro-optical conversion is carried out through an optical modulator. The optical modulator modulates an optical carrier by an electric signal that contains the information to be transmitted. The modulation process is usually realized in one of two ways, by direct modulation of a light source, or by using an external modulator. Direct modulation is characterized by the interrupted operation of the optical source (on-off) depending on the information signal. This operation principle makes direct modulation simple and inexpensive, however, it does not allow generating multi-level signals and

the resulting pulses are considerably chirped (RAMASWAMI *et al.*, 2010). On the other hand, external modulation consists in modulating a continuously operated light source using an additional device. The need for more components makes external modulation more expensive, but it has the advantage of minimizing undesirable effects, particularly chirp.

Within external optical modulators, the Mach-Zehnder modulator (MZM) is an interferometric structure that performs intensity modulation using the principle of the interference. The MZM is illustrated in Figure 2.8 (RAMASWAMI *et al.*, 2010), (AGRAWAL, 2002).

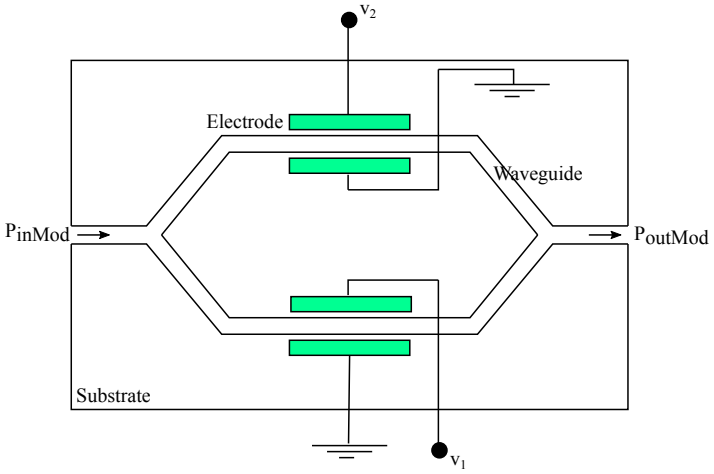

Figure 2.8 – Mach-Zhender modulator. P_{inMod}: input signal. P_{outMod}: output signal

The light entering the MZM is divided into two paths. Each path presents a phase modulator whose phase modulation depends on the waveguide refractive index. Then, varying the refractive index by means of the application of an external voltage allows to control the phase shift between paths. In this way, after the recombination of the two electric fields, the interference varies between constructive and destructive, depending on the relative phase delay between the two arms. In practice, there is a voltage V_π which, when applied to the signal, causes a phase delay of π radians. The pull-push configuration consists in applying two voltages such that $v_1 = -v_2 = V$, where V is related to the output power according to:

$$P_{outMod} = P_{inMod} \cos^2\left(\frac{\pi V}{2V_\pi}\right), \tag{2.6}$$

that is, always that v_1 and v_2 make V be $(2k+1) \times V_\pi$ with $l \in 0, 1, 2, ...$, then, the interference between arms is totally destructive and there is no any output power. Otherwise, when V is $(2k) \times V_\pi$ with $k = 0, 1, 2, ...$, both arms interfere constructively and the output power is maximum. Figure 2.9 shows the MZM output with respect to voltage V. Note that, with this modulator configuration, it is possible to obtain binary phase shift keying (BPSK) modulation.

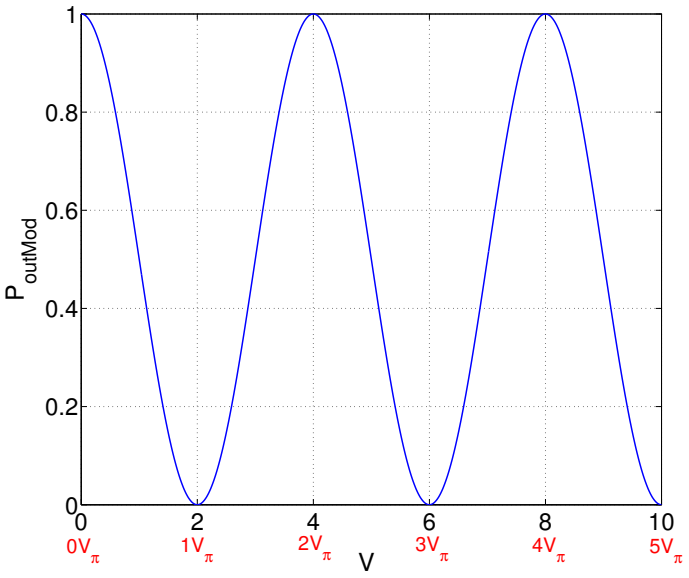

Figure 2.9 – Output power of the MZ modulator.

For higher order modulation formats, a new structure is constructed from the combination of two MZM. The in-phase and quadrature modulator (IQM) is shown in Figure 2.10. In this modulator, the input signal is equally divided between the in-phase (I) and quadrature (Q) arms. The signal of the quadrature arm passes through a phase modulator and experiences a delay of $\pi/2$ radians, so that the signal modulated in the MZM of arm Q is orthogonal to the signal modulated in the MZM of arm I. Finally, the signals from these two arms are recombined at the output of the modulator. As each MZM generates a signal that carries information in only one component (I, Q), the combination of the two signals carries information in both.

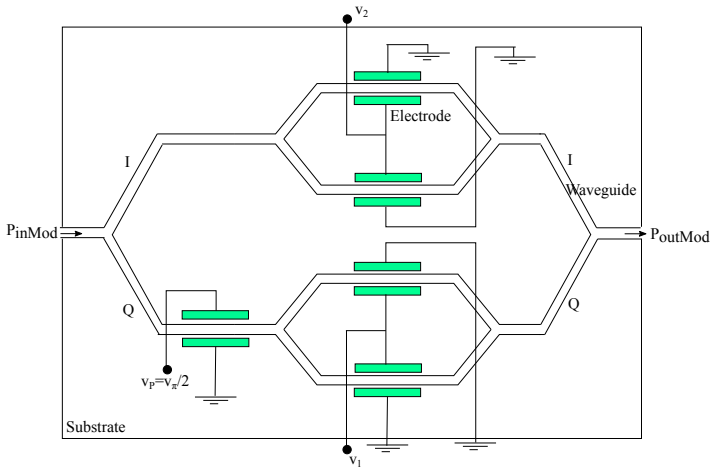

Figure 2.10 – IQ modulator.

In a polarization multiplexing system, the optical modulator integrates two IQM, as illustrated in Figure 2.11. Besides, it integrates a polarization beam splitter (PBS)

for splitting the input signal. After the modulators, the signals in both arms are again recombined through a polarization beam combiner (PBC).

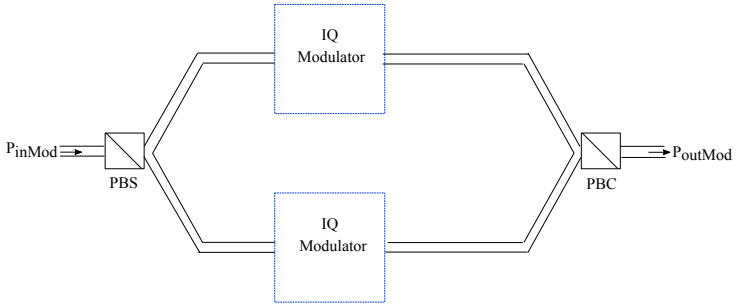

Figure 2.11 – IQ modulator with polarization multiplexing.

2.2 OPTICAL CHANNEL

The optical fiber imposes several perturbations to the signal, such as fiber loss, CD, PMD, and non-linear effects (AGRAWAL, 2002), leading to a received signal which is a corrupted version of the transmitted one. In addition, in amplified systems, another source of perturbation appears from amplified spontaneous emission noise (ASE).

2.2.1 Amplified spontaneous emission (ASE)

In an amplified system, stimulated emission is the physical principle behind signal amplification. As it was initially studied by Einstein (PAULI, 1994), stimulated emission refers to photon generation due to the atom transition from its higher energy level E2 (excited state) to its lower energy level E1 (ground state) in the presence of an electromagnetic field. The generated photons through stimulated emission not only have the same energy as the incident photons, but also the same direction of propagation, phase, and polarization (AGRAWAL, 2002), (RAMASWAMI *et al.*, 2010), (DEMTRöDER, 2005). Therefore, the amplification process is the result of the contribution of generated photons that add constructively to the incident field. On the other hand, in spontaneous emission, photons are emitted in random directions, polarizations, and phases (RAMASWAMI *et al.*, 2010). Consequently, amplified spontaneous emission appears as noise at the output of the amplifier and becomes a source of degradation of the system performance.

The power spectral density (PSD) of spontaneous-emission-induced noise $S_{sp}(v)$ is nearly constant in the signal bandwidth. Thus the ASE noise can be treated as additive white Gaussian noise. According to (AGRAWAL, 2002), $S_{sp}(v)$ is given by:

$$S_{sp}(v) = (G-1)n_{sp}h\nu, \tag{2.7}$$

where h is Planck's constant, ν is the optical frequency, and the parameter n_{sp} is the spontaneous emission factor, defined as:

$$n_{sp} = \frac{N_2}{N_2 - N_1}, \tag{2.8}$$

where N_1 and N_2 are the atomic populations for the ground and excited states, respectively.

In optical systems, the optical signal-to-noise ratio (OSNR) is an important metric for system characterization. The OSNR is related to the ASE PSD (AGRAWAL, 2002) as:

$$\text{OSNR} = \frac{P_T}{2S_{sp}B_{ref}}, \tag{2.9}$$

where P_T is the total power of the signal considering two polarization orientations and B_{ref} is the reference bandwidth, whose typical value is 12.5 GHz, corresponding to a 0.1 nm resolution bandwidth of optical spectrum analyzers at 1550 nm.

The most popular measure of communications systems performance is the bit error rate (BER), which corresponds to the ratio between the number of bits detected with error and the total amount of transmitted bits. Relating BER and OSNR allows analyzing the robustness of the system against different sources of degradation. For deriving a mathematical expression that relates these two parameters, it is necessary to user another well-known parameter, the signal-to-noise ratio (SNR). The SNR is a measure of the signal level with respect to the noise level in the electric domain. Specifically, SNR is defined as (HAYKIN, 2001):

$$\text{SNR} = \frac{E_s}{N_0}, \tag{2.10}$$

where E_s is the total signal energy and N_0 is the noise PSD. The relation between SNR and BER for QPSK is given by (BARRY *et al.*, 2004):

$$\text{BER} = \frac{1}{2}\text{erfc}\sqrt{\frac{\text{SNR}}{\log_2(M)}}, \tag{2.11}$$

for 16-QAM:

$$\text{BER} = \frac{3}{8}\text{erfc}\sqrt{(6 \times 15)\frac{\text{SNR}}{\log_2(M)}}, \tag{2.12}$$

and for 64-QAM:

$$\text{BER} = \frac{2}{\log_2(M)} \times \left(1 - \frac{1}{\log_2(M)}\right)\text{erfc}\sqrt{\frac{3\,\text{SNR}}{2\log_2(M) - 2}}, \tag{2.13}$$

where erfc denotes the complementary error function. Finally, for a system with additive white Gaussian noise (AWGN) and Nyquist pulse shaping, it is possible to relate SNR and OSNR as (ESSIAMBRE *et al.*, 2010), (ESSIAMBRE; TKACH, 2012):

$$\text{SNR} = \frac{2B_{ref}}{pR_s}\text{OSNR}, \tag{2.14}$$

where p is the number of polarization modes and R_s refers to the symbol rate. Therefore, from Eqs. 2.11, 2.12, 2.13 and 2.14 a theoretical bond amidst BER and OSNR is obtained.

2.2.2 Fiber losses

One of the most important limitations of optical fiber transmission is the signal attenuation during its propagation as result of fiber losses. Consequently, at the end of the link, the signal experiences a power reduction that can hamper its detection (KEISER, 2000). The sensitivity parameter determines the minimum amount of power required in reception for recovering the signal for a certain BER, limiting the distance between transmitter and receiver. This condition gives rise to the need of amplifiers in order to compensate for accumulated losses. However, each amplification stage contributes to additional system costs (AGRAWAL, 2002) and noise.

For fiber losses characterization, the attenuation coefficient α is defined in Np/km as (SALEH, 1991), (AGRAWAL, 2002):

$$\frac{dP_{av}}{dz} = -\alpha P_{av}, \tag{2.15}$$

where P_{av} is the average optical power and z the propagation distance. Thus, if P_{In} is the power launched at the input of a fiber with length L, the output power P_{Out} is given by:

$$P_{Out} = P_{In}\, e^{-\alpha L}. \tag{2.16}$$

From Eq. 2.16, the attenuation coefficient in dB/km is:

$$\alpha_{[dB/km]} = -\frac{10}{L}\, log_{10}\, \frac{P_{Out}}{P_{In}}. \tag{2.17}$$

Two of the main sources of fiber losses are material absorption and Rayleigh scattering. Absorption losses are related to the materials that compose the fiber. On the other hand, scattering losses take place because of microscopic variations in the material density, producing a fluctuation in the refractive index (BAGAD, 2007). Figure 2.12, shows the attenuation profile for the wavelength window between 1100 nm and 1700 nm in a standard single mode fiber (SSMF).

It can be observed in Figure 2.12 that the region with lower attenuation, and consequently the most suitable for long-haul transmission, is approximately between 1530 nm and 1625 nm that, according to (NAGAYAMA *et al.*, 2002), corresponds to the C (1530 nm – 1565 nm) and the L (1565 nm – 1625 nm) bands.

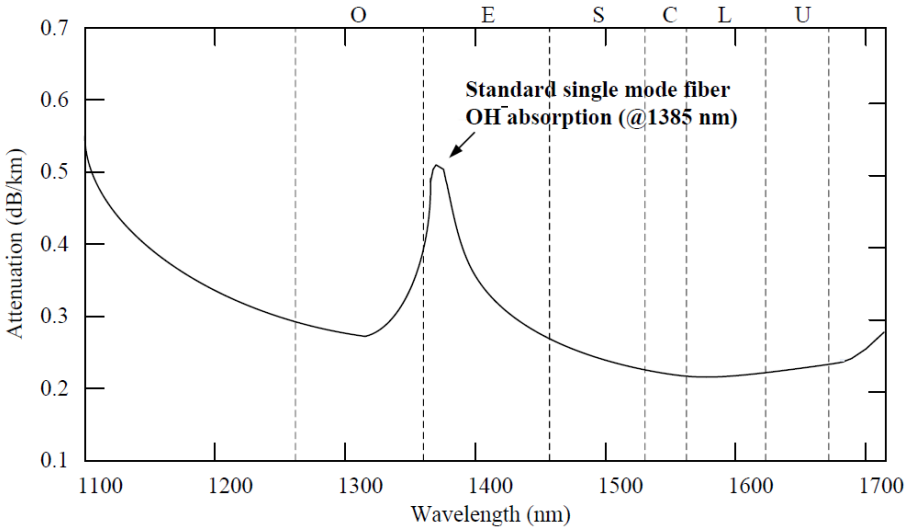

Figure 2.12 – Attenuation value for SSMF over optical channels. Adapted from (ZHANG, 2012).

2.2.3 Chromatic dispersion

In an optical fiber, the refractive index is wavelength dependent. Then, as the light pulse propagating through the fiber is composed of different spectral components, groups of wavelengths travel with a different velocities, arriving at different times at the receiver. This phenomenon generates pulse broadening, an effect known as chromatic dispersion (CD) (SHAPIRO, 1975), (SABRA, 1981), (CANTOR, 1983). CD is the result of two main contributions. First, material dispersion arises because the refractive index of silica is frequency dependent. The second CD component is called waveguide dispersion and takes place because the pulse energy does not propagate entirely in the core. The power distribution between core and cladding is wavelength dependent, and the effective index depends on the power distribution (RAMASWAMI *et al.*, 2010).

For mathematical modeling of CD, one can consider a single-mode fiber of length L and a transmitted pulse with spectral linewidth $\Delta\omega$. A specific spectral component at the frequency ω arrives at the output end of the fiber after a time delay $T = L/v_g$, where v_g is the group velocity, defined as (AGRAWAL, 2002):

$$v_g = (d\beta/d\omega)^{-1}. \tag{2.18}$$

The propagation constant β can be related to the angular frequency ω, speed of light c and effective index $\bar{n}$ as follows:

$$\beta = \bar{n}(\omega/c). \tag{2.19}$$

Then, the extent of pulse broadening for the fiber ΔT is given by:

$$\begin{aligned}\Delta T &= \frac{dT}{d\omega}\,\Delta\omega \\ &= \frac{d}{d\omega}\left(\frac{L}{v_g}\right)\Delta\omega \\ &= L\,\frac{d^2\beta}{d\omega^2}\,\Delta\omega \\ &= L\beta_2\,\Delta\omega,\end{aligned} \tag{2.20}$$

where $\beta_2 = d^2\beta/d\omega^2$ is known as the group-velocity dispersion (GVD) parameter. Eq. 2.20 can be rewritten in terms of the bandwidth of the transmitted signal $\Delta\lambda$ (AGRAWAL, 2002) as:

$$\Delta T = \frac{d}{d\lambda}\left(\frac{L}{v_g}\right)\Delta\lambda = DL\Delta\lambda. \tag{2.21}$$

The dispersion parameter D is expressed in units of $ps/(km\,nm)$, and is given by:

$$D = \frac{d}{d\lambda}\left(\frac{1}{v_g}\right) = -\frac{2\pi c}{\lambda^2}\,\beta_2. \tag{2.22}$$

Dispersion compensating fibers (DCF) are often used to mitigate CD (GRUNER-NIELSEN *et al.*, 2005). Theses special fibers are designed to have the opposite D parameter than the SSMF, therefore, they are able to revert the dispersive effect experienced by the signal after transmission for compensating the accumulated dispersion. Nevertheless, DCFs contribute to additional insertion losses. Therefore, chromatic dispersion compensation through digital signal processing has been widely used in coherent optical systems.

2.2.4 Polarization mode dispersion (PMD)

In a single-mode optical fiber, the fundamental mode is composed of two orthogonally polarized components known as vertical and horizontal polarizations, or also referred as X and Y polarizations. Over ideal conditions, through an optical fiber without imperfections and with circular symmetry, both polarizations propagate with identical group velocities. In practice, however, the fiber cross-section deviates from circular to elliptical due to external stresses or fabrication irregularities, resulting in birefringence. In a birefringent fiber, orthogonal polarizations travel with different group velocities, giving rise to the concept of fast and slow axis. Under this condition one of the polarizations arrives earlier at the link end, generating a pulse broadening known as polarization mode dispersion (PMD) (RASHLEIGH; ULRICH, 1978), (POOLE; WAGNER, 1986), (GALTAROSSA, 2005). Figure 2.13 illustrates the PMD effect.

In fibers used for optical transmission links, birefringence is a random phenomenon since the variations in the core format are not constant, therefore, the delay

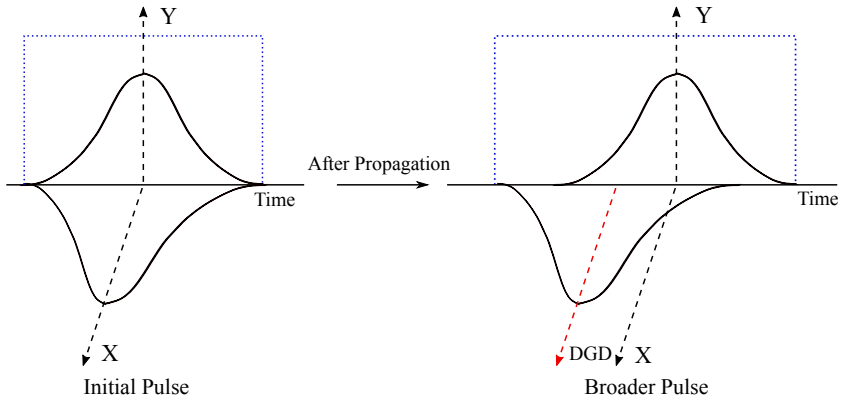

Figure 2.13 – Polarization mode dispersion.

between both polarizations will be random too. Thus, the differential group delay (DGD) $\Delta\tau$ is given by (HUTTNER, 1998):

$$\Delta\tau = P_{PMD}\sqrt{L}, \tag{2.23}$$

where P_{PMD} is the PMD parameter of a fiber with length L, measured in $ps/\sqrt{km}$.

The energy interchange between both polarization modes causes information coupling, resulting in polarization interference. In consequence, the fields at end of the link are an altered version of the originals ones. Linear effects on the polarization suffered by the optical signal when propagating through the fiber can be represented using Jones formalism (JONES, 1942). According to Jones formalism, the electric fields received at the output of a fiber are given by:

$$\begin{bmatrix} E_{R,X} \\ E_{R,Y} \end{bmatrix} = \mathbf{J} \begin{bmatrix} E_{T,X} \\ E_{T,Y} \end{bmatrix}, \tag{2.24}$$

where $E_{R,X}$ and $E_{R,Y}$ are the electric fields of the signals received in polarizations X and Y, respectively, while $E_{T,X}$ and $E_{T,Y}$ are the transmitted electric fields. Matrix $\mathbf{J}$ is defined in frequency domain as:

$$\mathbf{J} = \begin{bmatrix} H_{XX} & H_{XY} \\ H_{YX} & H_{YY} \end{bmatrix}. \tag{2.25}$$

In Eq. 2.25, H_{ij} $i, j \in (X, Y)$, is the influence of the input signal in polarization j on the output signal in polarization i. In order to compensate for the effect of PMD in digital form, the Jones inverse matrix must be estimated and its evolution over time must be tracked. The above procedure is implemented by means of an equalizer, whose coefficients are dynamically updated in order to keep up with the time-varying characteristics of the transmission medium.

2.2.5 Nonlinearities

This thesis does not intend to go into details about non-linear perturbations. However, it is important to remark that during its propagation through the optical fiber, the signal is disturbed by mainly two kinds of non-linear effects, inelastic light scattering and phase modulations. Two examples of inelastic scattering are Brillouin scattering (BRILLOUIN, 1922) and Raman scattering (RAMAN, 1928). In both phenomena, the frequency of a photon propagating through the optical fiber is shifted to a lower frequency so that the energy difference appears in the form of a phonon. These scattering processes result in a loss of power at the incident frequency, however, that loss is negligible at low power levels. On the other hand, at high powers levels, the scattering becomes important. As Brillouin scattering occurs only in the backward direction, it not only decreases the power in the incident frequency, but it can also cause damage to the transmitter. Raman scattering, in turn, takes places in both, backward and forward directions. Although scattering may affect the performance of the system, Raman scattering can be used to amplify an optical signal by transferring energy to it from a pump beam.

Nonlinear phase modulation appears with a nonlinear dependence of the refractive index with power, a phenomenon known as Kerr effect (KERR, 1875), (DZIEDZIC *et al.*, 1981), (WEINBERGER, 2008). The Kerr effect can give rise to three types of nonlinear effects, self phase modulation (SPM), cross phase modulation (XPM) and four wave mixing (FWM). SPM only has impact in single channel systems with high levels of CD. On the other hand, XPM is significative in WDM systems because the phase modulation of a specific channel depends not only on the optical power in this channel but also on the optical power in all channels. Finally, FWM arises in systems that transmit information on several frequencies. FWM consists in the generation of new frequencies due to the mixing of existing frequencies. These new frequencies can cause interference with other existing signals (AGRAWAL, 2002), (RAMASWAMI *et al.*, 2010).

2.3 RECEIVER

After the optical channel, the receiver must carry out opposite processes on the received sequence for recovering the transmitted signal. In systems in which the spectral efficiency is raised by means of phase-modulated formats, a coherent receiver is required, giving rise to coherent optical systems (OKOSHI; KIKUCHI, 1988). A coherent receiver is composed of a set of building blocks as follows.

2.3.1 Front-end

The front-end uses a local oscillator laser and a photo-detector arrangement for obtaining the electric signals that correspond to the in-phase and quadrature components. The resulting analog electrical signal needs to be further converted to the digital domain and processed for recovering the transmitted information. Figure 2.14 shows the structure of an optical front-end.

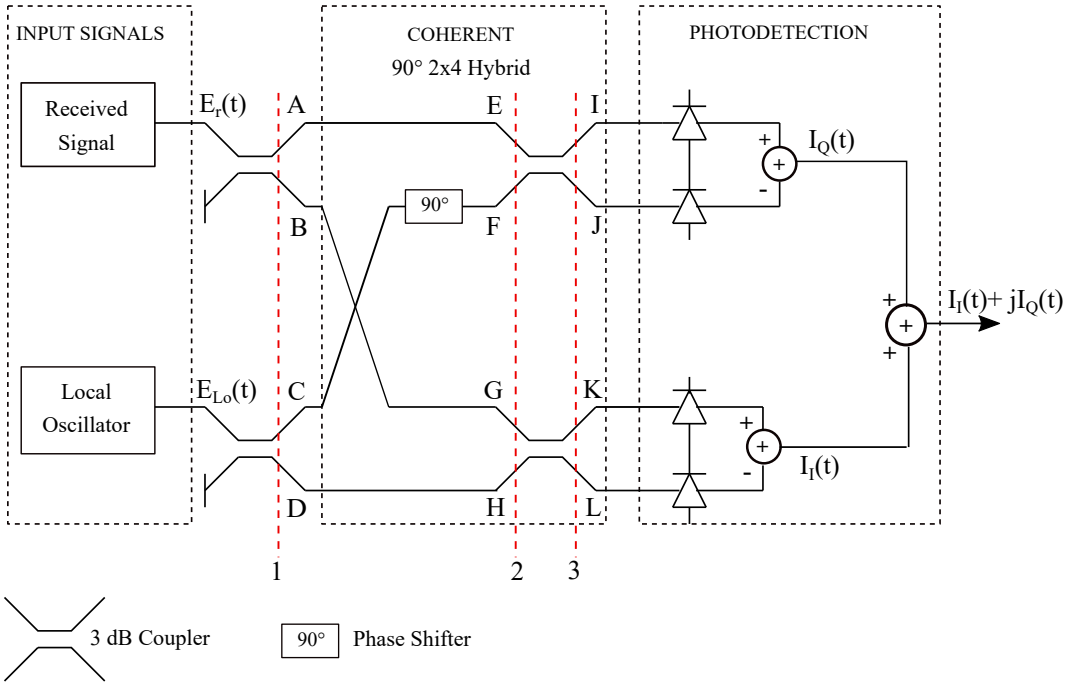

Figure 2.14 – Block diagram of a front-end with balanced detection for a single polarization system.

As shown in Figure 2.14, the optical front-end contains a local oscillator which generates the reference signal for the coherent mixing. The receivers can be classified as homodyne, heterodyne or intradyne, depending on the degree of similarity between the nominal central frequencies of the transmitter laser and the local oscillator laser. In a homodyne receiver, the lasers central frequencies are nominally identical, while in a heterodyne both frequencies differ by a large value, which is typically about twice the received signal baseband bandwidth. Practical implementation of these two kinds of coherent receivers is quite challenging regarding complexity and cost constraints. On the other hand, the intradyne receiver compensates the disadvantages of complexity, cost, sensitivity and bandwidth requirements of other architectures by using DSP algorithms. In this type of receiver, the center frequencies of the signals are not exactly the same, but similar, presenting a small offset which can be compensated by means of advanced algorithms in the DSP stage (LEVEN *et al.*, 2007).

The 90° 2x4 hybrid promotes the linear combination between the received

signal and the reference signal. It is composed of four 3 dB couplers and one 90° phase shifter. The mathematical process that describes the generation of its four outputs is primarily based on the transference function of a 3 dB coupler **H** which, according to (AGRAWAL, 2002), is given by:

$$\mathbf{H} = \frac{1}{\sqrt{2}} \begin{bmatrix} 1 & 1 \\ 1 & -1 \end{bmatrix}. \tag{2.26}$$

Thereby, the expressions for the fields at boundary **1** in Figure 2.14 are:

$$E_A(t) = \frac{1}{\sqrt{2}} E_r(t), \tag{2.27}$$

$$E_B(t) = \frac{1}{\sqrt{2}} E_r(t), \tag{2.28}$$

$$E_C(t) = \frac{1}{\sqrt{2}} E_{Lo}(t), \tag{2.29}$$

$$E_D(t) = \frac{1}{\sqrt{2}} E_{Lo}(t), \tag{2.30}$$

where $E_r(t)$ and $E_{Lo}(t)$ are the fields of received signal and local oscillator signal, respectively.

At boundary **2**, due to the 90° phase shifter, the fields become:

$$E_E(t) = \frac{1}{\sqrt{2}} E_r(t), \tag{2.31}$$

$$E_F(t) = \frac{1}{\sqrt{2}} E_{Lo}(t) e^{j\frac{\pi}{2}}, \tag{2.32}$$

$$E_G(t) = \frac{1}{\sqrt{2}} E_r(t), \tag{2.33}$$

$$E_H(t) = \frac{1}{\sqrt{2}} E_{Lo}(t). \tag{2.34}$$

Finally, after passing through the next two couplers, the fields at boundary **3** are described by:

$$E_I(t) = \frac{1}{2} E_r(t) + \frac{1}{2} E_{Lo}(t) e^{j\frac{\pi}{2}}, \tag{2.35}$$

$$E_J(t) = \frac{1}{2} E_r(t) - \frac{1}{2} E_{Lo}(t) e^{j\frac{\pi}{2}}, \tag{2.36}$$

$$E_K(t) = \frac{1}{2} E_r(t) + \frac{1}{2} E_{Lo}(t), \tag{2.37}$$

$$E_L(t) = \frac{1}{2}E_r(t) - \frac{1}{2}E_{Lo}(t). \tag{2.38}$$

From Eqs. 2.35-2.38, the transfer function that relates the inputs and outputs of a 90° 2x4 Hybrid can be obtained as:

$$\begin{bmatrix} E_I(t) \\ E_J(t) \\ E_K(t) \\ E_L(t) \end{bmatrix} = \frac{1}{2}\begin{bmatrix} 1 & e^{j\frac{\pi}{2}} \\ 1 & -e^{j\frac{\pi}{2}} \\ 1 & 1 \\ 1 & -1 \end{bmatrix}\begin{bmatrix} E_r(t) \\ E_{Lo}(t) \end{bmatrix}. \tag{2.39}$$

Signal mixing is carried out by the photo-detection process. The photo-detection block is formed by two pairs of balanced photo-detectors which carry out the optical-electrical conversion. In simple terms, a photo-detector generates a current I_p that is proportional to the input power P_{inpd} as indicated by (AGRAWAL, 2002):

$$I_p = RP_{inpd}, \tag{2.40}$$

where R is the responsivity factor. The responsivity of a photo-detector is an indicator of its conversion efficiency η and can be derived as:

$$\eta = \frac{\text{Electron Generation Rate}}{\text{Photon Incidence Rate}} = \frac{I_p/q}{P_{inpd}/h\nu}, \tag{2.41}$$

where q, h and ν are the electron charge, Planck's constant and optical frequency, respectively. Then from Eqs. 2.40 and 2.41, R is:

$$R = \frac{\eta q}{h\nu}. \tag{2.42}$$

Subsequently, based on Eqs. 2.35-2.38 and 2.40, the photo-currents corresponding to in-phase and quadrature components of the detected electrical signal are given by:

$$\begin{aligned} i_Q(t) &= R|E_I(t)|^2 - R|E_J(t)|^2 \\ &= R|\frac{1}{2}E_r(t) + \frac{1}{2}E_{Lo}(t)e^{j\frac{\pi}{2}}|^2 - R|\frac{1}{2}E_r(t) - \frac{1}{2}E_{Lo}(t)e^{j\frac{\pi}{2}}|^2 \\ &= R|\frac{1}{2}E_r(t) + \frac{1}{2}E_{Lo}(t)e^{j\frac{\pi}{2}}|^2 - R|\frac{1}{2}E_r(t) + \frac{1}{2}E_{Lo}(t)e^{j\frac{3\pi}{2}}|^2, \end{aligned} \tag{2.43}$$

and

$$\begin{aligned} i_I(t) &= R|E_K(t)|^2 - R|E_L(t)|^2 \\ &= R|\frac{1}{2}E_r(t) + \frac{1}{2}E_{Lo}(t)|^2 - R|\frac{1}{2}E_r(t) - \frac{1}{2}E_{Lo}(t)|^2 \\ &= R|\frac{1}{2}E_r(t) + \frac{1}{2}E_{Lo}(t)|^2 - R|\frac{1}{2}E_r(t) + \frac{1}{2}E_{Lo}(t)e^{j\pi}|^2. \end{aligned} \tag{2.44}$$

The electric fields of the received and local oscillator signal can be then defined as (HO, 2005):

$$E_r(t) = [A_s(t)e^{j\phi_s(t)} + \eta_s(t)]e^{j\omega_o t}, \tag{2.45}$$

and

$$E_{Lo}(t) = [A_{Lo} + \eta_{Lo}(t)]e^{j\omega_{Lo} t}, \tag{2.46}$$

where A_s and A_{Lo} are the amplitudes of the received signal and the local oscillator signal, respectively. One can note that while the optical signal amplitude is variant over time, the amplitude of the signal coming from the local oscillator is constant. In addition, ϕ_s is the optical signal phase and ω_o and ω_{Lo} are the angular frequencies of the optical carrier and the local oscillator signal, respectively. Finally, η_s is the complex Gaussian noise of the optical signal and η_{Lo} the local oscillator noise.

Using relationship:

$$|a+b|^2 = |a|^2 + |b|^2 + 2\,\Re\,\{ab^*\}, \quad a, b \in Z, \tag{2.47}$$

the photo-currents of Eqs. 2.43 and 2.44 as redefined as:

$$i_Q(t) = R\,A_{Lo}\,A_s(t)\,sin(\omega_{IF} + \phi_s) + R\,\Re\left\{\left[A_{Lo}\eta_s(t) + A_s(t)\eta_{Lo}(t)e^{j\phi_s(t)}\right]e^{j\left(\omega_{IF}+\frac{\pi}{2}\right)}\right\}, \tag{2.48}$$

and

$$i_I(t) = R\,A_{Lo}\,A_s(t)\,cos(\omega_{IF} + \phi_s) + R\,\Re\left\{\left[A_{Lo}\eta_s(t) + A_s(t)\eta_{Lo}(t)e^{j\phi_s(t)}\right]e^{j\omega_{IF}}\right\}, \tag{2.49}$$

where ω_{IF} is the intermediate frequency corresponding to the difference between angular frequencies of the carrier signal and local oscillator:

$$\omega_{IF} = \omega_o - \omega_{Lo}. \tag{2.50}$$

Considering homodyne coherent detection, the intermediate frequency becomes zero and the photo-currents can be expressed through equations (HO, 2005):

$$i_Q(t) = R\,A_{Lo}\,A_s(t)\,sin(\phi_s) + R\,\Re\left\{\left[A_{Lo}\eta_s(t) + A_s(t)\eta_{Lo}(t)e^{j\phi_s(t)}\right]e^{j\frac{\pi}{2}}\right\}, \tag{2.51}$$

$$i_I(t) = R\,A_{Lo}\,A_s(t)\,cos(\phi_s) + R\,\Re\left\{\left[A_{Lo}\eta_s(t) + A_s(t)\eta_{Lo}(t)e^{j\phi_s(t)}\right]\right\}. \tag{2.52}$$

After the optical front-end, the electrical signal is digitized for later being processed in the DSP stage. Further details of DSP block are presented in next section.

It is clear that the higher the order of the modulation format the greater the spectral efficiency of the system. Moreover, polarization diversity also significantly improves spectral efficiency, since it allows the system to transmit two independent signals using the same optical fiber in the same frequency. For this case, in which two orthogonally polarized signals are sent at the same time in the same frequency, the receiver has to be properly designed to correctly recover the in-phase and quadrature components of the X and Y polarization signals. In a dual polarization front-end, it is necessary to incorporate two 90° 2x4 hybrids and four pairs of balanced photo-detectors, as well as a PBS for dividing the optical signal and local oscillator signal into two orthogonally polarized branches. Figure 2.15 illustrates a dual polarization front-end.

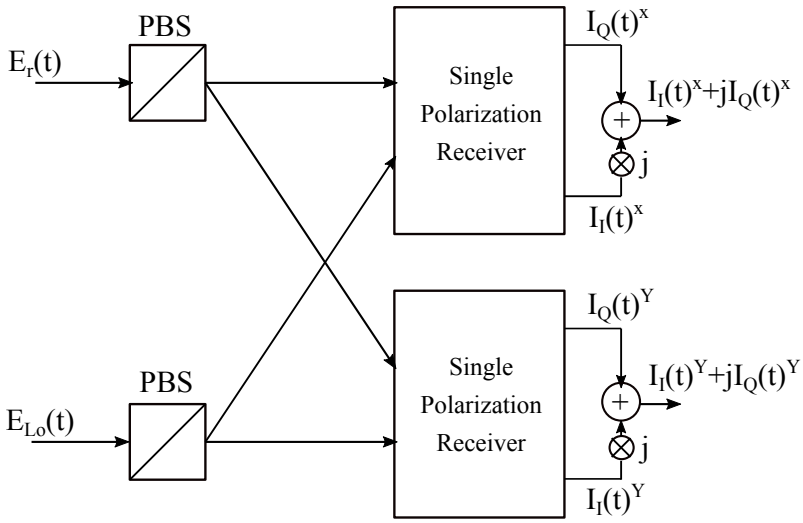

Figure 2.15 – Block diagram of a front-end for a dual polarization system.

Such as in a coherent receiver of a single polarization, in a dual polarization coherent receiver, after optical-to-electric conversion, the analog signals in X and Y polarizations have to be digitized. After that the signals are digitally processed for reverting the eventual perturbations experienced during modulation, propagation, and reception.

2.3.2 Digital signal processing (DSP)

Once the signals have been converted from electric to optical domain, they are digitized and processed for compensating transmission impairments. In this section, the main DSP algorithms for this task are presented.

2.3.2.1 Quadrature imbalance (QI)

In practical coherent receivers, imperfections on hybrids, phase shifter or photodetectors can produce loss of orthogonality between in-phase and quadrature components of the signal, a phenomenon known as quadrature imbalance (QI). The QI effect can be

clearly observed in the constellation diagram of the signal after digitization. Figure 2.16 shows a QPSK constellation with QI.

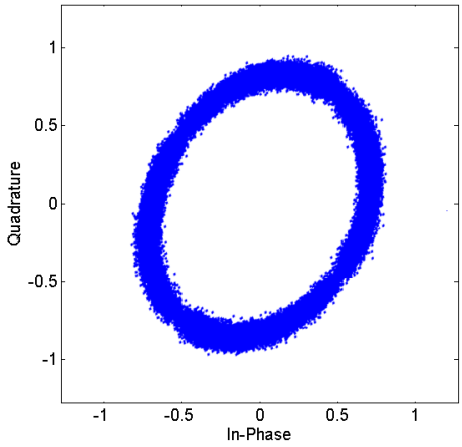

Figure 2.16 – Quadrature imbalances on QPSK constellation.

The system performance can be significantly degraded if QI is not compensated by the receiver DSP for high-order modulation formats (FARUK; SAVORY, 2017). The Gram-Schmidt orthogonalization procedure (GSOP) is a well-known technique for orthogonalization of two non-orthogonal vectors. Therefore, GSOP is often incorporated in the DSP stage for QI compensation. From (FATADIN *et al.*, 2008), given two non-orthogonal components of the received signal denoted by $I'(t)$ and $Q'(t)$, the GSOP results in a new pair of orthonormal components $I(t)$ and $Q(t)$. The procedure is as follows: first, $I(t)$ is calculated from $I'(t)$ as:

$$I(t) = \frac{I'(t)}{\sqrt{\bar{P}_I}}, \tag{2.53}$$

and later, an intermediate variable $Q^o(t)$ is obtained using $Q'(t)$ and $I'(t)$:

$$Q^o(t) = Q'(t) - \frac{\rho\, I'(t)}{\bar{P}_I}, \tag{2.54}$$

then, $Q(t)$ is given by:

$$Q(t) = \frac{Q^o(t)}{\sqrt{\bar{P}_Q}}, \tag{2.55}$$

where $\rho = E[I(t)Q(t)]$ and $\bar{P}_I$ and $\bar{P}_Q$ are the average power of the respective component:

$$\bar{P}_I = E[I^2(t)], \tag{2.56}$$

$$\bar{P}_Q = E[Q^2(t)]. \tag{2.57}$$

In simple terms, the Gram-Schmidt orthogonalization is based on defining a new vector that is orthogonal to the initially selected vector. This makes the two vectors orthogonal as shown in Figure 2.17.

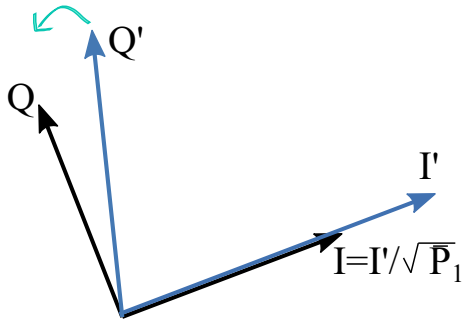

Figure 2.17 – GSOP orthogonalization.

Figure 2.18 shows an example in which the GSOP has been applied to a non-orthogonal constellation. After normalization, the constellation presents again its characteristic shape, without distortions introduced in the optical front-end.

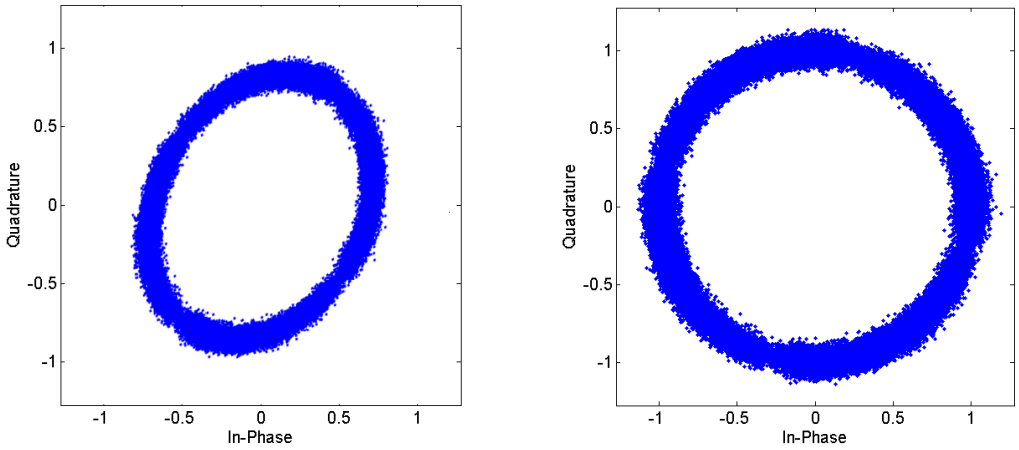

(a) Constellation before GSOP (b) Constellation after GSOP

Figure 2.18 – Constellation before and after GSOP.

2.3.2.2 CD compensation

As CD varies slowly over time (SALEH, 1991), the digital signal processing tasks for its compensation can be performed by a static equalizer (XU *et al.*, 2010). In (SAVORY, 2008) and (KUSCHNEROV *et al.*, 2009b) a frequency domain transfer function that models the signal propagation through the fiber in the absence of fiber nonlinearity, is defined as:

$$G(z,\omega) = exp\left(-j\,\frac{D\lambda^2}{4\pi c}\,\omega^2\,z\right), \tag{2.58}$$

where ω is the signal angular frequency. The dispersion compensating filter is therefore given by the all-pass filter $1/G(z,\omega)$, which can be approximated using for instance nonrecursive methods as time domain equalizer (TDE) (SAVORY, 2008), (KUSCHNEROV *et al.*, 2009b) and frequency domain equalizer (FDE) (KUSCHNEROV *et al.*, 2009b). On the other hand, some approaches try to invert the transfer function of the fiber by means of adaptive filters, this is the case of the works in (SPINNLER *et al.*, 2008), (KUSCHNEROV *et al.*, 2009a), (GOLDFARB; LI, 2007) and (XU *et al.*, 2010).

2.3.2.3 Equalization

On ideal conditions, in a system with polarization diversity, both Y and X polarizations remain unaltered after fiber propagation. Nonetheless, in a real context, the fiber link introduces some effects on the signals, distorting the transmitted signal. Polarization mode dispersion corresponds to a critical perturbation experienced by the signal in a birefringent fiber (WINFUL, 1986). Birefringence leads to a periodic power exchange between the two polarization components. Then, at the receiver, the signal received in one polarization is a mixture between the original information sent in each independent polarization by the transmitter (AGRAWAL, 2002). The above condition can be understood as a polarization interference, a phenomenon that has to be compensated by means of digital signal processing.

The technique able to accurately recover the two original signals is equalization. An equalizer is a filter whose task is to apply over the signal the opposite effect of the channel for compensating PMD and residual CD. In polarization demultiplexing, an adaptive equalizer composed of four linear filters is required. The filter coefficients must be dynamically updated for tracking channel variations in time. Within the mechanisms for filter adaptation, there are supervised adaptive algorithms, as the least-mean-square (LMS) and the recursive least-square (RLS), whose working principle is based on the use of a training signal as described in (ROMANO *et al.*, 2010) and (HAYKIN, 2014). On the other hand, non-supervised adaptive techniques, such as the constant modulus algorithm (CMA) and the radius directed equalization (RDE), do not require a training signal for operating. Hence, non-supervised algorithms are known as blind algorithms. Now, the CMA and RDE fundamentals are presented as well as some variants found in literature.

- **Constant modulus algorithm (CMA)**

The CMA belongs to an extended family of blind adaptive-filtering algorithms that minimizes the distance between the modulus of the equalizer output and some specific constant values, without using a training signal (GODARD, 1980). Mathematically, if $\mathbf{x}(k)$, $\mathbf{h}(k)$

and $y(k)$ are the input vector, filter impulse response and output of the equalizer, then, the general objective of the Godard algorithm is to minimize the cost function given by:

$$\begin{aligned}\xi_{Godard} &= E\Big[(|\mathbf{h}^H(k)\mathbf{x}(k)|^q - r_q)^p\Big], \\ &= E\Big[(|y(k)|^q - r_q)^p\Big], \\ &= E\Big[e^p_{Godard}(k)\Big],\end{aligned} \tag{2.59}$$

with,

$$r_q = \frac{E\Big[|s(k)|^{2q}\Big]}{E\Big[|s(k)|^q\Big]}, \tag{2.60}$$

where q and p are positive integers. The r_q parameter defines the value that $|y(k)|^q$ should attain and e^p_{Godard} denotes the error offset between them, raised to the power of p. The expression that governs the coefficient updates of a Godard equalizer filter is given by (GODARD, 1980), (SAYED, 2008):

$$\begin{aligned}\mathbf{h}(k+1) &= \mathbf{h}(k) - \frac{1}{2}\mu\, p\, q\, (|y(k)|^q - r_q)^{p-1}\, |y(k)|^{q-2}\, y^*(k)\mathbf{x}(k), \\ &= \mathbf{h}(k) - \frac{1}{2}\mu\, p\, q\, e^{p-1}_{Godard}(k)\, |y(k)|^{q-2}\, y^*(k)\mathbf{x}(k),\end{aligned} \tag{2.61}$$

where μ is the step size and $e(k)$ is the error function. Setting $q = p = 2$ corresponds to the constant modulus (CM) criterion. Thus, from Eq. 2.59, the objective function of CM criterion becomes:

$$\begin{aligned}E\Big[e^2_{CMA}(k)\Big] &= E\Big[(|\mathbf{h}^H(k)\mathbf{x}(k)|^2 - r_2)^2\Big], \\ &= E\Big[(|y(k)|^2 - r_2)^2\Big],\end{aligned} \tag{2.62}$$

in this case,

$$r_2 = \frac{E\Big[|s(k)|^4\Big]}{E\Big[|s(k)|^2\Big]}. \tag{2.63}$$

Eqs. 2.62 and 2.63 evidence that whenever the input symbols have constant modulus, the target of the error minimization based on CM is to keep $|y(k)|^2$ as close as possible to the constant value of r_2. From (GODARD, 1980), (SAYED, 2008) and (FATADIN *et al.*, 2009), the updating equation for CMA is given by:

$$\begin{aligned}\mathbf{h}(k+1) &= \mathbf{h}(k) - 2\mu\, (|y(k)|^2 - r_2)\, y^*(k)\mathbf{x}(k), \\ &= \mathbf{h}(k) - 2\mu\, e_{CMA}(k)\, y^*(k)\mathbf{x}(k).\end{aligned} \tag{2.64}$$

Clearly, for PSK signals, CM is the optimal criterion in the sense that for perfect equalization, the error $e_{CMA}(k)$ becomes zero as the whole symbol sequence lies on a circle.

In (JOHNSON *et al.*, 1998), the CM criterion cost function is examined through several illustrative examples and the results confirm the characteristic of non-convexity what was already observed by Godard. The CM cost function presents not only a global

minimum but local minima, a condition that makes the initialization of CMA a critical step for accurate convergence. Center-spike initialization is the most recommended technique in the literature (SJOLANDER, 2011). In coherent optical systems, CMA carries out the polarization demultiplexing through the butterfly structure presented in Figure 2.19. The sequences of the received signals in both polarizations $\mathbf{x}_{in}(k)$ and $\mathbf{y}_{in}(k)$ are

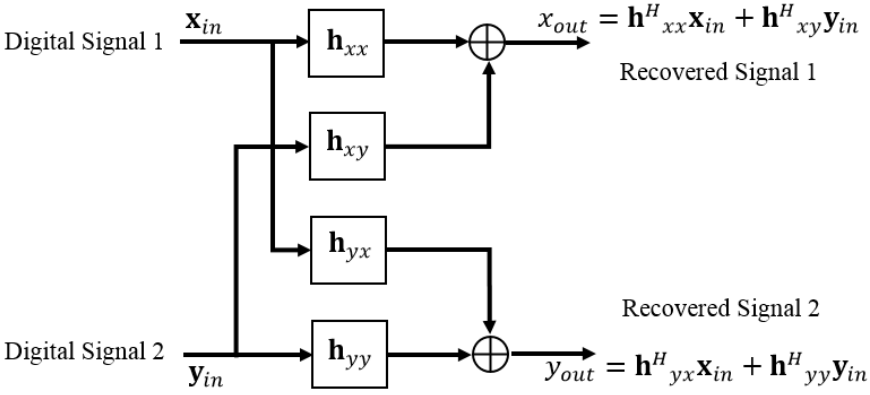

Figure 2.19 – Butterfly structure for adaptive equalization.

the input of the structure, while $\mathbf{h}_{xx}$, $\mathbf{h}_{xy}$, $\mathbf{h}_{yx}$, $\mathbf{h}_{yy}$ correspond to the four finite impulse response (FIR) digital filters of size (1 × N) and x_{out} and y_{out} are the equalized and demultiplexed signals. These variables are related as:

$$\begin{bmatrix} x_{out} \\ y_{out} \end{bmatrix} = \begin{bmatrix} \mathbf{h}_{xx}^H & \mathbf{h}_{xy}^H \\ \mathbf{h}_{Yx}^H & \mathbf{h}_{yy}^H \end{bmatrix} \begin{bmatrix} \mathbf{x}_{in} \\ \mathbf{y}_{in} \end{bmatrix}, \tag{2.65}$$

where H denotes hermitian operation. The coefficient vectors of the four filters can be represented as:

$$\mathbf{h}_{xx}(k) = \begin{bmatrix} h_{xx}(k) & h_{xx}(k-1) & h_{xx}(k-2)\ldots h_{xx}(k-N+2) & h_{xx}(k-N+1) \end{bmatrix}^H, \tag{2.66}$$

$$\mathbf{h}_{xy}(k) = \begin{bmatrix} h_{xy}(k) & h_{xy}(k-1) & h_{xy}(k-2)\ldots h_{xy}(k-N+2) & h_{xy}(k-N+1) \end{bmatrix}^H, \tag{2.67}$$

$$\mathbf{h}_{yx}(k) = \begin{bmatrix} h_{yx}(k) & h_{yx}(k-1) & h_{yx}(k-2)\ldots h_{yx}(k-N+2) & h_{yx}(k-N+1) \end{bmatrix}^H, \tag{2.68}$$

$$\mathbf{h}_{yy}(k) = \begin{bmatrix} h_{yy}(k) & h_{yy}(k-1) & h_{yy}(k-2)\ldots h_{yy}(k-N+2) & h_{yy}(k-N+1) \end{bmatrix}^H, \tag{2.69}$$

and the input vectors are formed by the samples:

$$\mathbf{x}_{in}(k) = \begin{bmatrix} x_{in}(k) & x_{in}(k-1) & x_{in}(k-2)\ldots x_{in}(k-N+2) & x_{in}(k-N+1) \end{bmatrix}^T, \tag{2.70}$$

$$\mathbf{y}_{in}(k) = \begin{bmatrix} y_{in}(k) & y_{in}(k-1) & y_{in}(k-2)\ldots y_{in}(k-N+2) & y_{in}(k-N+1) \end{bmatrix}^T, \tag{2.71}$$

where T is the transpose operator.

Then, from Eq. 2.65, the equalizer outputs are:

$$x_{out} = \mathbf{h}_{xx}^H \mathbf{x}_{in} + \mathbf{h}_{xy}^H \mathbf{y}_{in}, \tag{2.72}$$

$$y_{out} = \mathbf{h}_{yx}^H \mathbf{x}_{in} + \mathbf{h}_{yy}^H \mathbf{y}_{in}. \tag{2.73}$$

Based on the above concepts, the taps of the four filters are updated according to (SAVORY, 2010):

$$\mathbf{h}_{xx}(k+1) = \mathbf{h}_{xx}(k) + \mu\varepsilon_x \mathbf{x}_{in} x^*_{out}, \quad (2.74)$$

$$\mathbf{h}_{xy}(k+1) = \mathbf{h}_{xy}(k) + \mu\varepsilon_x \mathbf{y}_{in} x^*_{out}, \quad (2.75)$$

$$\mathbf{h}_{yx}(k+1) = \mathbf{h}_{yx}(k) + \mu\varepsilon_y \mathbf{x}_{in} y^*_{out}, \quad (2.76)$$

$$\mathbf{h}_{yy}(k+1) = \mathbf{h}_{yy}(k) + \mu\varepsilon_y \mathbf{y}_{in} y^*_{out}, \quad (2.77)$$

where μ is the step size and ε_x and ε_y denote the error signals, given as:

$$\varepsilon_x = (1 - |x_{out}|^2), \quad (2.78)$$

$$\varepsilon_y = (1 - |y_{out}|^2). \quad (2.79)$$

Note that in Eqs. 2.78 and 2.79 the output signal modulus is being compared with the modulus 1.

The CMA was devised for modulation formats whose symbols have constant modulus. Accordingly, its performance degrades for higher-order constellations in which symbols present different amplitudes. Then, for extending the CM criterion to high-order modulations, some modifications on the algorithm are required. Several variants of the constant modulus algorithm can be found in literature. For instance, (BANOVIC *et al.*, 2006) presents three different approaches based on the CMA principle for 16-QAM and 64-QAM which outperform the original proposal. Reference (WEI *et al.*, 2010) presents the mathematical development of the so-called modified constant modulus algorithm (MCMA), in which they split the output of the equalizer into real and imaginary parts and estimate error signals for both components. In (ABRAR; NANDI, 2010), by generalizing and modifying some existing cost functions, two new generic and efficient multi-modulus families of blind equalization algorithms are presented. These new approaches receive the name of multimodulus algorithm (MMA) and second multimodulus algorithm (CMMA).

- **Radius directed equalization (RDE)**

While the CMA error criterion achieves good performance for PSK signals, it may not be accurate for square-M-QAM constellations with M greater than 4. CMA presents a poor performance in systems with high order modulation formats because the constellations do not exhibit constant modulus (READY; GOOCH, 1990). It has been demonstrated in (READY; GOOCH, 1990) and (FATADIN *et al.*, 2009) that the RDE algorithm outperforms CMA in coherent systems which do not present constant modulus constellations. The above is supported by the fact that high order square modulation formats even

without presenting a constant modulus are made up of sets of symbols with the same magnitude. Then, for RDE implementation, the total constellation is divided into regions, each one corresponding to a specific radius. Figure 2.20 shows the separation in regions of the 16-QAM constellation.

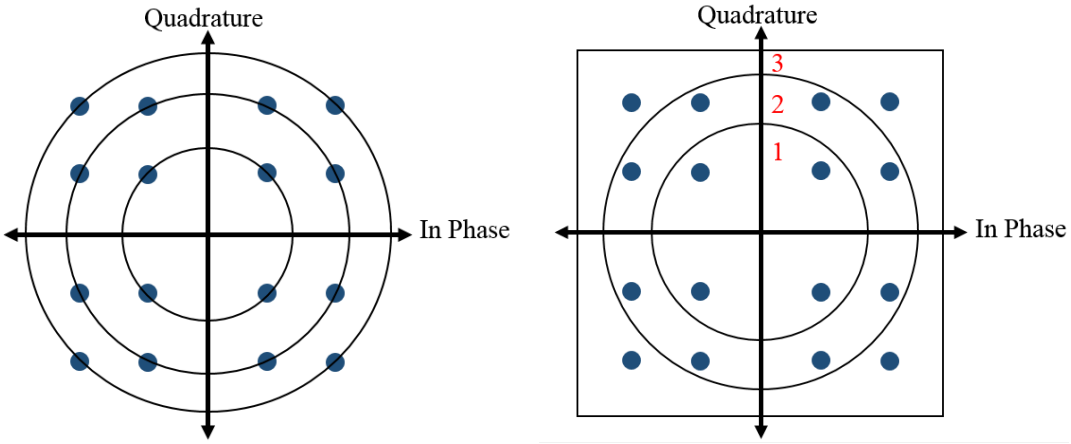

(a) RDE radii for 16-QAM (b) RDE regions for 16-QAM

Figure 2.20 – RDE regions for 16-QAM.

RDE algorithm uses an alternative error criterion that is based on the offset between the equalizer output and the nearest constellation radius. Its working principle consists in finding out the region that the equalizer output sample belongs to. Once the region is estimated, the appropriate radius R_k is selected for error signal calculation, as:

$$\varepsilon(k) = y(k)(R_k - |y(k)|^2). \tag{2.80}$$

After the error is calculated through Eq. 2.80, the RDE algorithm updates the filters taps according to Eqs. 2.74, 2.75, 2.76 and 2.77. The RDE algorithm has some interesting variants which try to increase the equalizer performance. For example, in (LAVERY *et al.*, 2015) a modified radius directed equalizer for high-order QAM, called probabilistic RDE is presented. In (FILHO *et al.*, 2011), it is remarked that, although the RDE error is smaller than for CMA case, a higher modulation order implies a smaller distance among radii, causing a decrement in the performance of the algorithm. Therefore, RDE can present slow convergence and high symbol error rates, which become unacceptable for low signal-to-noise ratios. Thus, a new version of RDE algorithm was presented.

3 PHASE PERTURBATIONS - FUNDAMENTALS AND COMPENSATION

3.1 PRINCIPLES OF SEMICONDUCTOR LASERS

3.1.1 Basic concepts

An optical transmitter converts the electric input signal into an optical signal for later injecting it into an optical fiber. An important transmitter element is the optical source that generates the light for posterior modulation and transmission. Semiconductor lasers are one of the main light sources and, therefore, are a major component of optical transmitters. In coherent optical communications, two light sources need to be incorporated into the system, a transmitter laser and a local oscillator laser. Techniques for semiconductor lasers manufacturing have evolved through the years. The predecessor of the laser received the name of optical microwave amplification by stimulated emission of radiation (MASER) and was brought to light by Schawlow e Townes in 1958 (SCHAWLOW; TOWNES, 1958). The inclusion of the word "light" to the device name was proposed first for Gordon Gould, who made important contributions with Townes as a partner. After these pioneering works, there were several papers which proved the feasibility of using semiconductors as an active medium for coherent light generation. For example, (HALL *et al.*, 1962) and (ARNOLD; MAYBURG, 1963) propose the first practical demonstrations of gallium arsenide-based lasers. Two other remarkable works are (RIPPER; LEITE, 1965) and (DYMENT; RIPPER, 1968), led by Ripper and Leite. On the other hand, the threshold current density required for the coherent emission of light was a critical aspect of concern. The first laser devices had impractical current density thresholds inhibiting light transmission in continuous mode. The migration of simple semiconductor junctions to more complex ones and the reduction of the active region of the laser allowed to decrease the threshold of current density for practical implementations (PANISH *et al.*, 1970), (ETTENBERG, 1975). In the telecommunications context, the migration of gallium arsenide to other semiconductor crystals based on indium phosphide provided the transition of the light wavelength to other bands (HSIEH *et al.*, 1976), (OE *et al.*, 1977), (KAMINOW *et al.*, 1979), (AKIBA *et al.*, 1979). Indeed, the advance of optical communications is linked to the development of high performance lasers. Therefore, from the first studies to the present, the goal has been to obtain lasers with optimized features, that is, low linewidths and high output powers.

Regarding laser operating principle, let us consider an atom and two of its en-

ergy levels, E1 and E2, known as ground state and excited state, respectively (DEMTRöDER, 2005). When an incident photon of the electromagnetic field has an energy equal to the energy difference between the two states, it is absorbed by the atom, inducing a transition from E1 to E2. After that, the atom returns to its ground state emitting light during the transition. There are two processes for light emission, stimulated emission and spontaneous emission. In the case of the spontaneous emission, the atom transition from E2 to E1 is independent of any external radiation, and resulting photons are emitted in random directions, polarization, and phase. On the other hand, in the stimulated emission process, after photon incidence, the emitted photons match with the incident one in energy, frequency, polarization and propagation direction. This is the amplification principle of the laser devices, which receive their name from light amplification by stimulated emission of radiation (LASER).

During the interaction between atoms and the electromagnetic field, there are three important quantities related to the atomic densities in the ground and the excited states and with the spectral density of the electromagnetic energy. R_{spon}, R_{Rstim}, R_{Rabs}, represent the spontaneous emission rate, stimulated emission rate and absorption rate, respectively. For coherent emission of light, stimulated emission rate has to dominate, thus, two conditions are strictly required for lasers operation. First, thermal equilibrium implies $R_{spon} > R_{Rstim}$. Therefore, all lasers must operate away from thermal equilibrium. On the other hand, even satisfying this condition, it is possible that $R_{Rstim} < R_{Rabs}$, thus, in order to the stimulated emission rate exceed absorption rate, the atomic density of the excited state has to be greater than the atomic density of the ground state. This requirement is known as population inversion and is a prerequisite for laser operation. Population inversion is usually achieved by means of an external pump that is typically performed by a polarization current.

The laser structure is commonly constructed by setting a Fabry-Perot (FB) cavity between two plane and parallel facets localized at the extremes. The cavity encloses a gain medium that in the case of semiconductor lasers is a semiconductor material. The idea of placing the gain medium in a FB cavity is to get a high gain for some specific wavelengths that correspond to resonant wavelengths. As population inversion must be satisfied, the p-type and n-type cladding layers are pumped with a polarization current until the active region exhibits a gain. Figure 3.1a displays the basic structure of a semiconductor laser while Figure 3.1b shows the cavity operation.

At the beginning, an input signal propagating inside the active layer reaches the right facet. A portion of light leaves the cavity and the rest is reflected in the direction of the left facet. Then, a part of the energy is again reflected and goes back to the right facet, and this process is repeated. For cavity resonant wavelengths, all the waves emitted

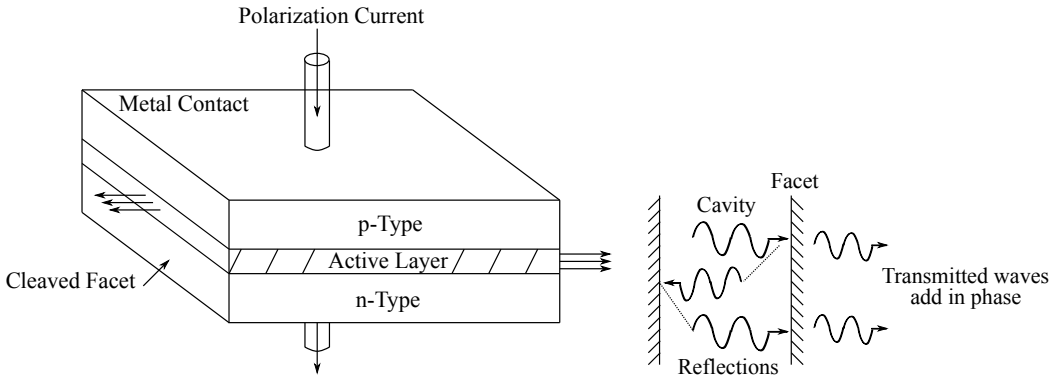

(a) Semiconductor laser structure (b) Cavity operation

Figure 3.1 – Semiconductor laser operation. Adapted from (AGRAWAL, 2002).

from the right facet are added in phase, this way, the amplitude of the transmitted wave is greater in these wavelengths in comparison with the other ones (RAMASWAMI *et al.*, 2010). Lasers do not need only a gain medium for working, but require a positive feedback. Before reaching the feedback state, the device acts as an amplifier. Consequently, the pumping current has to be incremented until the gain medium surpasses the cavity losses and the amplifier starts to oscillate. The current needed for reaching the laser threshold is known as threshold current. Beyond the threshold, the device is no longer an amplifier but an oscillator or laser and is able to produce coherent light.

3.1.2 Longitudinal modes

As it was remarked in the previous section, a FB laser oscillates simultaneously in all cavity resonant wavelengths. Resonant frequencies of a FB filter are described as (AGRAWAL, 2002):

$$f_k = \frac{k}{2\tau_{fp}}, \qquad k \in Z \tag{3.1}$$

where τ_{fp} is given by:

$$\tau_{fp} = \frac{nl}{c}, \tag{3.2}$$

where n is the cavity refractive index, l the cavity length and c is the speed of light.

All the wavelengths that satisfy the condition in Eq. 3.1 are called longitudinal modes of the laser. Therefore, a FB laser is known as a multi-longitudinal mode (MLM) laser. A MLM laser tends to present a large spectral width, a characteristic that limits its use in high-speed optical communications, where the spectral width of the source must be as narrow as possible to minimize the effects of chromatic dispersion and enable the use of high-order modulation formats (RAMASWAMI *et al.*, 2010).

Under ideal conditions, according to the gain and loss profile in semiconductor lasers presented in Figure 3.2, the mode closest to the gain peak becomes the dominant

mode. As the gain in the other modes does not exceed the cavity losses, they never reach the threshold. However, in practical contexts, the adjacent modes carry a considerable portion of the laser power, limiting the rate and reach of the system (AGRAWAL, 2002).

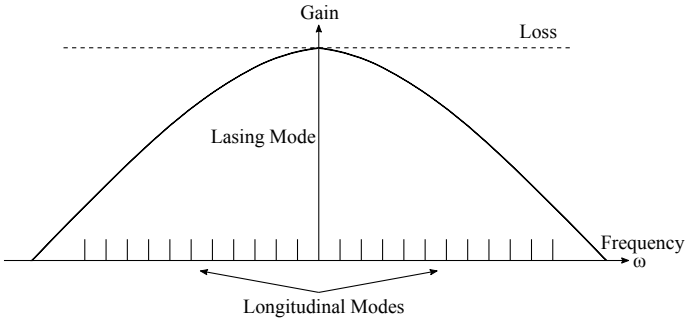

Figure 3.2 – Longitudinal modes profile. Adapted from (AGRAWAL, 2002).

The alternative for dealing with longitudinal modes is to design a single-longitudinal mode (SLM) laser, which emits light predominantly in only one mode. The common mechanism used for SLM laser construction is the manipulation of the cavity losses profile for getting the smallest loss for the desired wavelength and to discard the other wavelengths by applying them higher losses. The mode-suppression ratio (MSR) is a parameter for performance characterization of SLM lasers that determines the level to which longitudinal modes are suppressed regarding the main mode (AGRAWAL, 2002), (RAMASWAMI *et al.*, 2010).

3.1.2.1 Distributed feedback lasers (DFB)

In distributed feedback semiconductor lasers (DFB), the feedback is no longer originated from the reflectivity in the facets localized at the cavity extremes as described in FP lasers. Instead, in a DFB a set of reflectors are closely distributed throughout the cavity length forming an area known as corrugation or grating section. Figure 3.3 shows the DFB structure (KOGELNIK; SHANK, 1972), (YEN *et al.*, 1973), (MROZIEWICZ *et al.*, 2017).

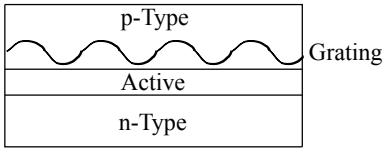

Figure 3.3 – DFB structure.

An incident wave experiences a series of reflections during its propagation. Reflected waves add in phase to the resulting transmitted wave only for the wavelengths

that satisfy the Bragg condition, given by (AGRAWAL, 2002):

$$\Lambda = m(\lambda_B/2\bar{n}), \tag{3.3}$$

where Λ is the grating period (corrugation period), $\bar{n}$ is the average mode index, and the integer m represents the order of Bragg diffraction. As several wavelengths accomplish Eq. 3.3, the condition for SML is readjusted so that the strongest transmitted wave occurs only for the wavelength for which the corrugation period is exactly equal to half the wavelength (RAMASWAMI *et al.*, 2010). The above requisite allows suppressing all other longitudinal modes. By varying the corrugation period, it is possible to obtain different operating wavelengths. DFBs are widely used in high-speed transmission systems.

3.1.2.2 External cavity lasers (ECL)

The principle of single-mode operation in external cavity lasers is based on coupling an extra cavity to the cavity where gain occurs (see Figure 3.4a). As the primary cavity has a set of resonant wavelengths, the same occurs with the coupled cavity. When a portion of light crosses the gain cavity facet, it propagates through the second cavity and suffers a reflection caused by its reflectivity facet, going back to the first cavity. Thus, the feedback is achieved only for the wavelengths that are simultaneously a longitudinal mode of both cavities. If the gain and the coupled cavities are accurately designed, only one wavelength satisfies this condition and, therefore, the laser oscillates in a single-longitudinal mode (FLEMING; MOORADIAN, 1981), (RAMASWAMI *et al.*, 2010).

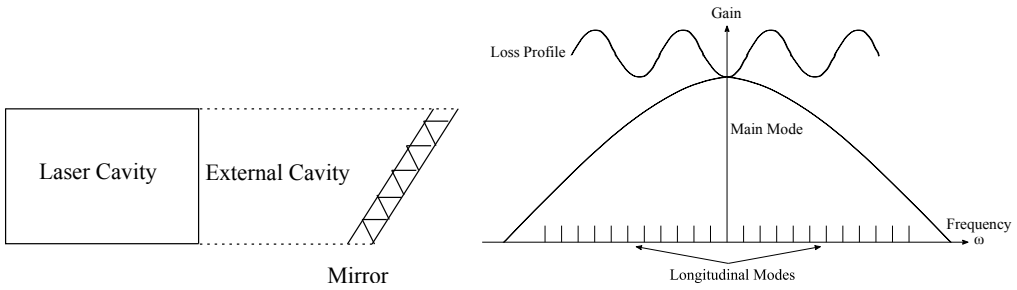

(a) ECL structure (b) ECL gain profile

Figure 3.4 – ECL structure and loss profile. Adapted from (AGRAWAL, 2002).

The coupling of cavities modifies the gain and loss profile of the laser. Figure 3.4b presents the profile for an external cavity laser in which it is observed how the longitudinal mode that is closest to the gain peak and has the lowest cavity loss becomes the dominant mode (AGRAWAL, 2002). When a diffraction grating is used in the coupled cavity, the laser receives the name of grating external cavity laser, and its tunability is obtained modifying the angle of the grating with regard to the primary cavity.

3.1.2.3 Vertical-cavity surface-emitting lasers (VCSEL)

According to Eq. 3.1, the spacing between resonant frequencies of a FP cavity is given by:

$$\delta_f = \frac{1}{2\tau_{fp}}, \tag{3.4}$$

therefore, the spacing between longitudinal modes can be manipulated controlling the cavity length. Hence, a laser with a very small cavity presents widely spaced longitudinal modes. As it can be observed in Figure 3.2, the gain of the medium has a specific bandwidth, consequently, if the laser is designed to make the length of the cavity sufficiently small, the mode spacing increases such that only one longitudinal mode occurs within the gain bandwidth. Due to the thin active layer of a vertical-cavity surface-emitting laser, two highly reflective mirrors are needed on the top and bottom of the gain region.

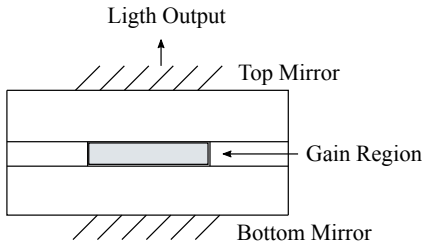

Figure 3.5 – VCSEL structure. Adapted from (RAMASWAMI *et al.*, 2010).

The VCSELs architecture presents a low cost and facilitates packaging. However, the reduced active region limits the VCSELs output power and leads to considerable heating of the device, generating the need for efficient thermal cooling (FAVRE *et al.*, 1986), (MOORADIAN, 1991), (TROPPER *et al.*, 2004), (AGRAWAL, 2002), (RAMASWAMI *et al.*, 2010).

3.1.3 Laser spectral linewidth

Ideally, a single-longitudinal mode laser should have a monochromatic nature and generates light in a single and precise frequency. However, spontaneous emission alters the phase and amplitude of the laser field. Firstly, photons generated from spontaneous emission contribute with random phases to the optical field. On the other hand, amplitude fluctuations induce relaxation oscillations, which cause additional phase changes while restoring the field amplitude to the steady state value. As consequence of phase perturbations, lasers emit light in a band of frequencies (HENRY, 1983).

The light emitted by a SLM has an spectrum $S(\omega)$ that, according to (AGRAWAL, 2002), is related with the field-autocorrelation function, $\Gamma_{EE}(\tau)$, through:

$$S(w) = \int_{-\infty}^{\infty} \Gamma_{EE}(t)\, exp[-j(\omega - \omega_o)\tau] \cdot d\tau, \tag{3.5}$$

with,

$$\Gamma_{EE}(\tau) =< E^*(t)E(t+\tau) >, \tag{3.6}$$

where $E(t)$ is the optical field, ω_o is the carrier angular frequency and τ is the delay. Symbol <> denotes the expectation operator.

Ideally, the spectrum of a SLM laser is found to be Lorentzian, and its spectral linewidth, Δ_{LW}, is defined as the full width at half maximum (FWHM). The Lorentzian spectrum is illustrated in Figure 3.6, and is given by (HENRY, 1986), (KRUGER; PETERMANN, 1988):

$$\Delta_{LW} = R_{spon}\frac{(1+\beta_c^2)}{4\pi\bar{I}}, \tag{3.7}$$

where R_{spon} is the rate of spontaneous emission into the lasing mode, and β_c is the

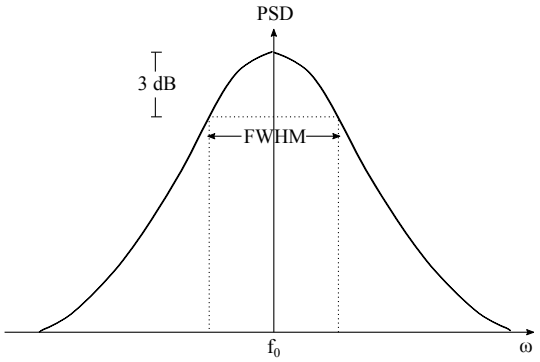

Figure 3.6 – Lorentzian spectrum.

linewidth enhancement factor, as it leads to an additional enhancement of the spectral width (HENRY, 1982). On its part, $\bar{I}$ is the average intensity related to the laser output power P, given by:

$$\bar{I} = \frac{2P}{hv\, v_g\, \alpha_m}, \tag{3.8}$$

where v_g is the cavity group velocity, hv is the photon energy and α_m is the facet loss. The average intensity is a function of the cavity gain g, waveguide loss α_L, facet reflectivity r_m and cavity length l. Eq. 3.7 evidences that a lower laser linewidth can be obtained by decreasing the R_{spon} through a reduction of the cavity length (AGRAWAL, 2002). Moreover, if in the laser design the β_c factor is adjusted for being small, a considerable reduction over laser linewidth is experienced. On the other hand, with regard to the average intensity, due to its relation of inverse proportionality with laser linewidth, an increment over the output power or over the cavity length causes a reduction of Δ_{LW}.

Contrary to what is expected, a constant increase of the lasing power is not necessarily assumed as a linewidth reduction. The laser linewidth could decrease as power increases until saturation point and then it can stay stable or even begin to rebroaden. This is a consequence of effects that generate a residual linewidth, for instance, the $1/f$ noise

and the excess spontaneous-emission noise (O'MAHONY; HENNING, 1983), (GOLDBERG *et al.*, 1991).

3.2 FREQUENCY OFFSET

In an intradyne coherent receiver, in which the operating frequencies of the transmitter laser and local oscillator laser are similar, but not identical, a perturbation in the phase of the received signal is generated as a consequence of the frequency offset Δ_f between them. The beating between two optical signals whose central frequencies are different results in a signal that oscillates in an intermediate frequency (SELMI *et al.*, 2009), (HOFFMANN *et al.*, 2008a). The receiver input signal in the presence of phase and frequency offset is expressed as (FARUK; SAVORY, 2017) (HOFFMANN *et al.*, 2008b):

$$r(k) = s(k)e^{j(\theta(k)+k\Delta_\Phi)} + w(k), \tag{3.9}$$

where $s(k)$ is the transmitted signal, $\theta(k)$ is the phase noise and $w(k)$ is the AWGN. Term Δ_Φ is the frequency offset-induced phase offset between the instants k and $k+1$, given by:

$$\Delta_\Phi = 2\pi\Delta_f T_{sa}, \tag{3.10}$$

where Δ_f is the difference between the central frequencies of the transmitter and the local oscillator lasers, and T_{sa} is the time between samples. Practical implementations show that lasers experience fluctuations on their central frequencies that are originated from mechanic vibrations, temperature changes or tuning mechanisms. Therefore, in practice, Δ_f varies over time, a phenomenon that receives the name of carrier frequency jitter (CFJ) (GIANNI *et al.*, 2011). Figure 3.7 illustrates the variation of the laser PSD over time.

CFJ can be modeled as random or deterministic process. In (SUNTER; ROY, 2004) and (OU *et al.*, 2004) the complete characterization of different types of digital jitter can be found. In a first attempt to study the CFJ effect, it is reasonable to assume the most simple approach, which consists in defining the jitter signal as a well-known waveform. Therefore, from experimental results in (FERREIRA, 2017), Δ_f can be modeled as a sinusoidal signal:

$$\Delta_f = \Delta_{F1} + \frac{\Delta_A}{2}\sin(2\pi f_A t), \tag{3.11}$$

where Δ_{F1} is the constant frequency offset between the two lasers, and Δ_A and f_A the peak-to-peak amplitude and the frequency of the sinusoidal jitter, respectively. The target of a frequency estimator is to identify the frequency offset that produces the phase shift experienced by the received symbols. Frequency recovery techniques can be widely classified as blind and training-aided methods. An interesting description of training-aided

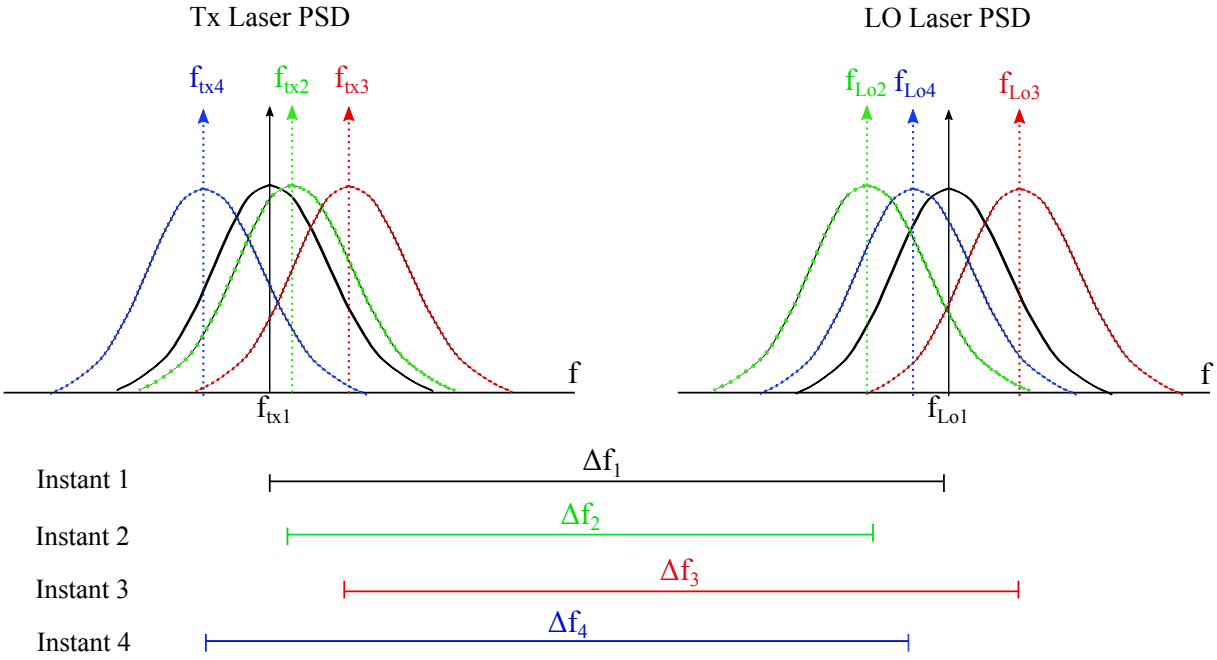

Figure 3.7 – Time variation of the frequency offset.

approaches is found in (FARUK; SAVORY, 2017) while three of the blind algorithms for frequency recovery are presented in the next sections.

3.2.1 Time-domain differential phase method

The time-domain differential phase technique consists in finding the average phase shift Δ_Φ between two consecutive samples. The average phase shift Δ_Φ that suffers two adjacent symbols is caused by the frequency offset between transmitter laser and local oscillator laser Δ_f:

$$\Delta_\Phi = 2\pi\Delta_f T_{sa}, \tag{3.12}$$

where T_{sa} is time between samples. Figure 3.8 shows a block diagram of the proposed estimator.

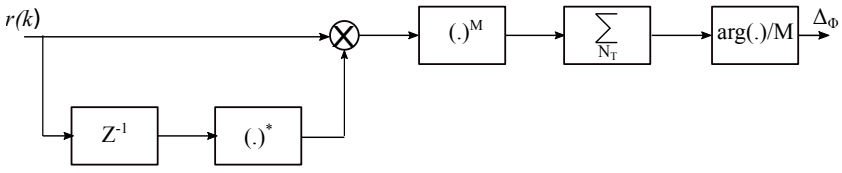

Figure 3.8 – Block diagram of time-domain differential phase based method.

The procedure shown in Figure 3.8 consists of the following steps: initially, the received sample in the k^{th} instant $r(k)$ is multiplied by the complex conjugate of the previous sample $r(k-1)$. The operation results in a complex number whose phase is equal to the phase difference between the two samples. Next, any phase modulation information

that is encoded in the signal is removed using the Mth-order power operation, with M denoting modulation order. The output of this block is then averaged over a large number of samples N_t and the argument of the resulting value is calculated. Finally, it is necessary to divide the obtained phase by M to correct for the earlier Mth-order power application. The resulting phase is an estimate of the phase difference Δ_Φ between consecutive samples (LEVEN *et al.*, 2007), (FERREIRA, 2017).

Although the time domain method can be easily used for M-PSK signals, the performance is considerably degraded for high-order QAM formats. This degradation happens because only a small portion of the constellation points has equal phase spacing, which hinders frequency offset extraction. Even for an M-PSK signal with large M, a time-domain-based method can become unstable when operating at a low optical-to-signal noise ratio region with relatively large phase noise (ZHOU, 2014).

3.2.2 Frequency domain methods

A popular method for frequency offset estimation is based on spectral analysis, in which the basic idea is to detect the frequency corresponding to the peak of the fast Fourier transform (FFT) of the signal. Since the spectrum of the Mth-order power of the signal exhibits a peak at M times the frequency offset, Δ_f can be estimated from the corresponding spectrum (FARUK; SAVORY, 2017). Figure 3.9 shows the step-by-step procedures of this technique known as Mth-order power algorithm.

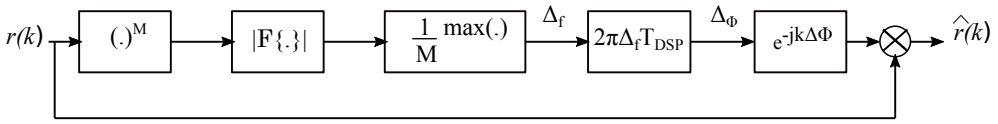

Figure 3.9 – Block diagram of frequency recovery based on spectral analysis.

The Mth-order power is carried out for the purpose of removing the phase modulation information of the transmitted signal. The frequency offset Δ_f is given by the index position of the peak of the FFT operation divided by M. The parameter T_{DSP} is the clock period of the DSP functions (FERREIRA, 2017) that can be adjusted to the time between samples. FFT-based methods can achieve much more reliable frequency offset estimation than the time-domain-based method (by using the same number of samples) but the implementation complexity is bigger, especially for higher-order QAM formats (ZHOU, 2014), (PFAU *et al.*, 2009). As highlighted previously, the key of the Mth-order power algorithm is to find the frequency offset by means of FFT application. However, if this procedure is carried out once over whole input signal, the algorithm estimates only a single frequency offset value for all time instants. In a practical context, when

the laser operating frequencies vary over with time, the frequency offset becomes a time-dependent process. Thus, in a system with CFJ, it is not enough to compensate the phase perturbations of the whole signal by the same Δ_Φ value. The above problem is a critical disadvantage of the current technique, as it represents an obvious source of performance degradation.

3.2.3 Blind frequency search methods

The blind frequency search (BFS) algorithm is a universal frequency offset estimator than uses the concept of minimum mean square distance error (MSDE) in terms of Euclidean distance as frequency selection criterion. BFS process is carried out in two stages: a coarse frequency offset estimation and subsequent a fine frequency offset estimation. Figure 3.10 shows BFS block diagram (ZHOU, 2014).

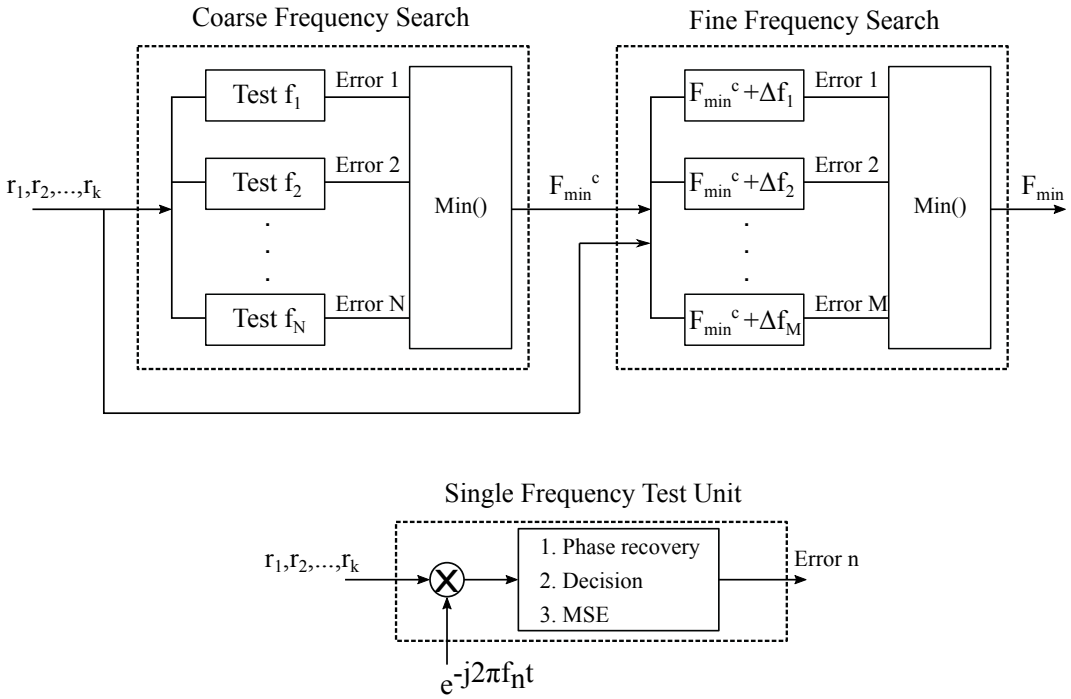

Figure 3.10 – Block diagram of blind frequency search method.

According to Figure 3.10, the first stage of BFS algorithm consists in defining a set of test frequency offset values and next to correct the input signal $r(k)$ for each one. Then, a decision stage is applied on all of the corrected samples and the resulting symbols are taken as a reference for mean squared error calculation. Finally, the optimal frequency offset value is the one that gives the minimum MSDE (ZHOU, 2014). The procedure in the second stage is the same as the previously described, however, the frequency step is smaller and the test values depend on the frequency offset found in coarse estimation. Reference (ZHOU *et al.*, 2011) presented a general description of BFS algorithm along

with its implementation, in which the frequency offset is first scanned at a coarse step size of 10 MHz and then at a fine step size of 1 MHz.

3.3 PHASE NOISE

Ideally, the laser is designed for generating light in a single frequency. In practice, however, lasers emit the signal in a band of frequencies, giving rise to what is known as phase noise. Phase noise on the received signal causes a random rotation in the constellation, which leads to a total loss of reference for the quadrature and in-phase components. Phase noise can be modeled as a Wiener process, where the phase perturbation experienced by the k^{th} symbol (PFAU *et al.*, 2009) is given by:

$$\theta(k) = \theta(k-1) + \Delta(k) = \sum_{m=0}^{k-1} \Delta(m), \tag{3.13}$$

where $\Delta(k)$ and $\Delta(m)$ are Gaussian random variables with zero mean and variance:

$$\sigma_{\Delta}^2 = 2\pi\Delta_{\nu}T_{sa}, \tag{3.14}$$

where Δ_{ν} is the sum of the transmitter and local oscillator laser linewidths, and T_{sa} the time between samples. In consequence, the higher $\Delta_{\nu}T_{sa}$, the higher the phase noise intensity. Eqs. 3.13 and 3.14 show that laser linewidth-induced phase noise in the k^{th} instant is the result of the addition of k independent and identically distributed increments. Figure 3.11 reflects the random rotation of two 16-QAM constellations of different lengths.

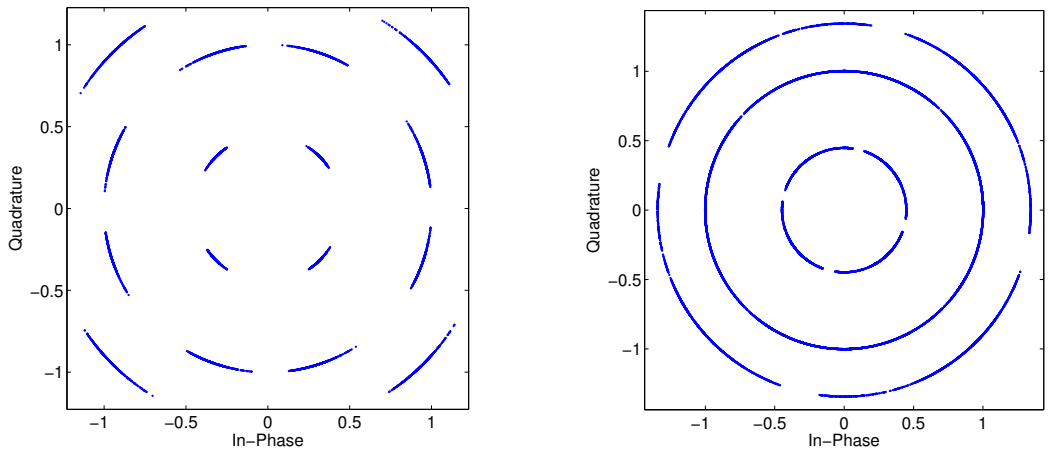

(a) 16-QAM constellation with 10000 symbols (b) 16-QAM constellation with 30000 symbols

Figure 3.11 – Constellation rotation due to Wiener phase noise.

In the DSP block, the target of the phase recovery stage is to identify the phase perturbation experienced by the samples as consequence of Wiener phase noise and

subsequently to compensate it. In the next sections, some algorithms for phase recovery are described. First, the Viterbi & Viterbi (V&V) algorithm is presented as a suitable solution for PSK and QPSK modulation formats, followed by the blind phase search (BPS) for high order modulation systems. Another important approach found in literature for phase recovery is the pilot-symbol aided estimation. Pilot-symbol-based methods exhibit more immunity to cycle slips (MEYR *et al.*, 1998), albeit at the expense of transmission overhead. In this technique, pilot symbols are time-multiplexed with data payload and are used at reception as a reference for improving the phase noise estimation. Works in (MAGARINI *et al.*, 2012) and (SPALVIERI; BARLETTA, 2011) present simple pilot-aided carrier recovery methods, while (PAJOVIC *et al.*, 2015) and (MILLAR *et al.*, 2016) incorporate an alternative technique known as multi-pilot aided carrier phase estimation.

3.3.1 Viterbi & Viterbi

The Viterbi&Viterbi phase recovery algorithm (VITERBI; VITERBI, 1983) allows accurate phase noise estimation for PSK and QPSK modulation formats. For phase recovery, it would be desirable that samples keep in their phases only the portion corresponding to noise. For this reason, the transmitted information contained in the signal must be removed. V&V algorithm principle is mainly based on applying the Mth-order power to remove phase modulation. Figures 3.12 and 3.13 present the BPSK and QPSK constellations before and after Mth-power.

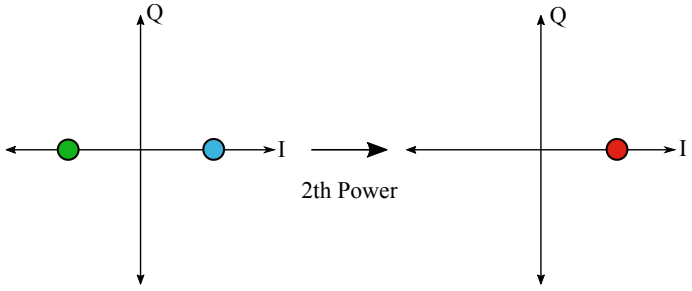

Figure 3.12 – 2th power applied to BPSK constellation.

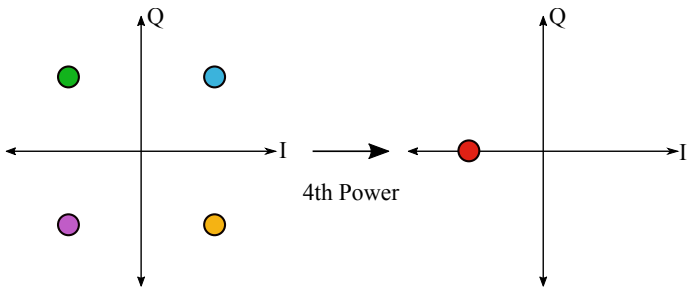

Figure 3.13 – 4th power applied to QPSK constellation.

As it can be observed in Figures 3.12 and 3.13, all symbols in the constellation are located in the same position after Mth-power. Therefore, any additional deviation from the theoretical symbol phase can be calculated through a simple *argument* operation. Let us consider for example a symbol corrupted by additive noise and phase noise. The received signal can be represented by:

$$r(k) = |r(k)|\ e^{j\left(\theta_T(k)+\theta(k)\right)} + w(k), \tag{3.15}$$

where, $|r(k)|$ and $\theta_T(k)$ are the amplitude and phase originally transmitted, $\theta(k)$ is the phase noise and $w(k)$ additive noise. After Mth-power, the signal can be expressed as:

$$[r(k)]^M = |r(k)|^M\ e^{jM\left(\theta_T(k)+\theta(k)\right)} + w_c(k), \tag{3.16}$$

where $w_c(k)$ corresponds to the cross terms between signal and noise. In Eq. 3.16 the data dependency is removed from the symbol phase since $\exp(2j\theta_T(k)) = 1$ for a BPSK signal and $\exp(4j\theta_T(k)) = -1$ for a QPSK signal. Consequently, the phase noise contribution can be estimated as the argument of the signal Mth-power, divided by M (VITERBI; VITERBI, 1983), (SAVORY, 2010), (KUSCHNEROV *et al.*, 2009b):

$$\hat{\theta}(k) = \frac{1}{M}\arg\{[r(k)]^M\}. \tag{3.17}$$

Phase noise is a process of independent Gaussian increments, where, the phase of a current sample (phase noise contribution) depends on the previous sample phase. On the other hand, as additive noise is modeled as a Gaussian process, the noise in a current sample is independent of the noise of past and future samples. Taking advantage of this fact, and in order to mitigate the additive noise effect over phase estimates, a moving average (MA) filter is incorporated (FERREIRA, 2011). Defining N_{PN} as filter window size, Eq. 3.17 results in:

$$\hat{\theta}(k) = \frac{1}{M} arg\left\{\sum_{n=0}^{N_{PN}-1}\left[r(k-n)^M\right]\right\}. \tag{3.18}$$

The V&V phase recovery algorithm requires an additional process. Phase unwrapping has to be carried out since the argument operation is limited between $-\pi$ and π radians, reducing the phase estimation into the interval -π/M and π/M. As a consequence, discontinuities in the estimate can generate errors in the decodification stage. This problem is usually addressed by a phase unwrapper, given by (IP; KAHN, 2007):

$$UN\left(\hat{\theta}(k)\right) = \hat{\theta}(k) + \left(\frac{1}{2} + \frac{\hat{\theta}(k-1) - \hat{\theta}(k)}{2\pi/M}\right)\frac{2\pi}{M}, \tag{3.19}$$

where *UN* denotes the unwrap function. Figure 3.14, summarizes the descriptive block diagram of the operating principle of V&V algorithm.

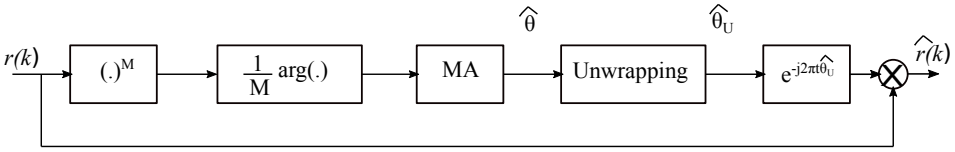

Figure 3.14 – Block diagram of Viterbi&Viterbi algorithm.

3.3.2 Blind phase search (BPS)

3.3.2.1 Conventional one-stage BPS

Phase recovery can be carried out by different methods depending on the modulation format. For QPSK, the Viterbi&Viterbi algorithm is a convenient approach due to its simplicity and effectiveness. On the other hand, for higher-order QAM signals, BPS represents an accurate technique that demands greater complexity of implementation but offers a good performance (PFAU, 2009). Figure 3.15 illustrates its implementation. After adaptive equalization and frequency recovery, the sample of the received signal at

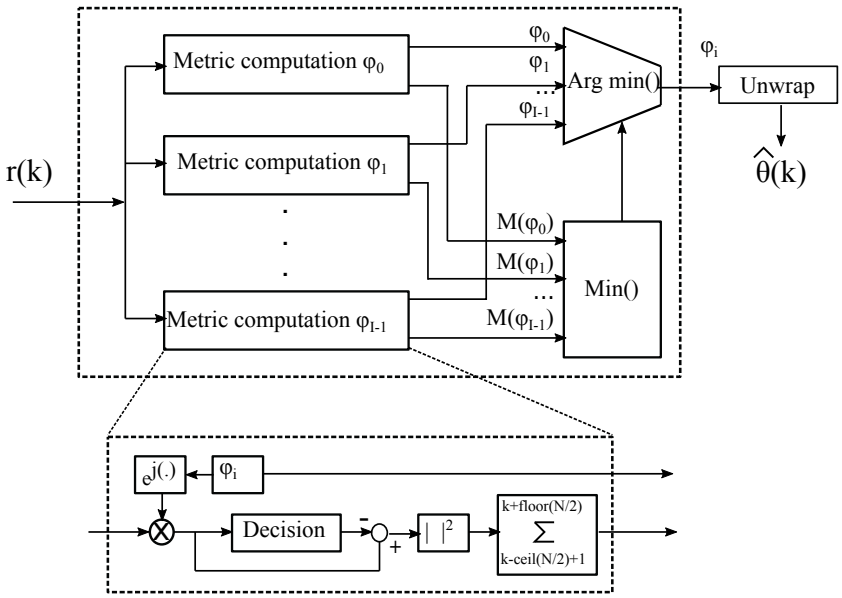

Figure 3.15 – Block diagram for the one-stage BPS algorithm.

k^{th} instant is still corrupted by phase noise and additive noise. In this way, for phase noise estimation, a distance metric $M(\varphi, k)$ is defined as:

$$M(\varphi, k) = \sum_{n=k-ceil(N_B/2)+1}^{k+floor(N_B/2)} |r(n)e^{j\varphi} - decision[r(n)e^{j\varphi}]|^2, \tag{3.20}$$

where $decision[.]$ refers to minimum distance decision in accordance with the given QAM constellation, φ represents the test phases in the range $[-\pi/4\ \pi/4)$ due to the $\pi/2$ rotational symmetry of the QAM constellations, $floor(.)$ corresponds to the flooring function,

$ceil(.)$ indicates the ceiling function and N_B is an integer denoting the length of the summing window within which the squared Euclidean distances of the symbols are summed up filter out the additive noise. With the above defined distance metric, the BPS algorithm finds a phase angle having the minimum distance metric:

$$\hat{\theta}(k) = UN\left[argmin_{\varphi\in[-\pi/4\,\pi/4)}\, M(\varphi, k)\right], \tag{3.21}$$

where $\hat{\theta}(k)$ is the phase estimate for the k^{th} symbol, $argmin_{\varphi}(A)$ refers to the search for phase φ which minimizes A and $UN[.]$ stands for the conventional unwrapping operation to overcome discontinuities. In practice, it is impossible to solve the above minimization problem over a continuous phase range. Hence, it is necessary to discretize the test phases interval into a finite set of equidistant phase angles, this way:

$$\varphi_i = \frac{i\pi}{2I} - \frac{\pi}{4}, \qquad where \quad i = 0, 1, ..., I-1, \tag{3.22}$$

where i is the index of the discrete phase angles and I is the total number of phase angles that defines the test-phase resolution (LI *et al.*, 2011). The computational complexity of the algorithm is highly dependent on the number of test phases. In order to decrease computational efforts, low-complexity phase recovery algorithms based on BPS have been proposed. For instance, in (ZHOU, 2014) a scheme called multistage hybrid blind phase search and maximum likelihood algorithm is presented. As well, a common approach for reducing the operational and computational cost is the two-stage BPS algorithm initially proposed in (PFAU *et al.*, 2009).

3.3.2.2 Two-stages BPS

Two-stage BPS is able to reach the same system performance by means of a comparable phase noise tolerance with regard to conventional BPS technique but reducing the total number of test phases (PFAU *et al.*, 2009). The block diagram of a general two-stage BPS estimator is shown in Figure 3.16.

The operation principle of this scheme is to carry out in BPS first stage a coarse phase estimation for finding a rough location of the optimal phase angle and, subsequently, to apply a fine phase search. As it can be observed in Figure 3.16, the value of phase estimate obtained in the initial stage is the reference input of the next stage, and the new test angles are calculated based on it. Thus, with $I1$ and $I2$ being the total number of test phase angles in first and second stages, respectively, the vectors $\phi_{i_j,j}$ that denote the i_j^{th} test phase angles in the j^{th} stage for $j \in (1, 2)$, are defined as (LI *et al.*, 2011):

$$\varphi_{i_1,1} = \frac{i_1\pi}{2I_1} - \frac{\pi}{4}, \quad where \quad i_1 = 0, 1, ..., I_1 - 1, \tag{3.23}$$

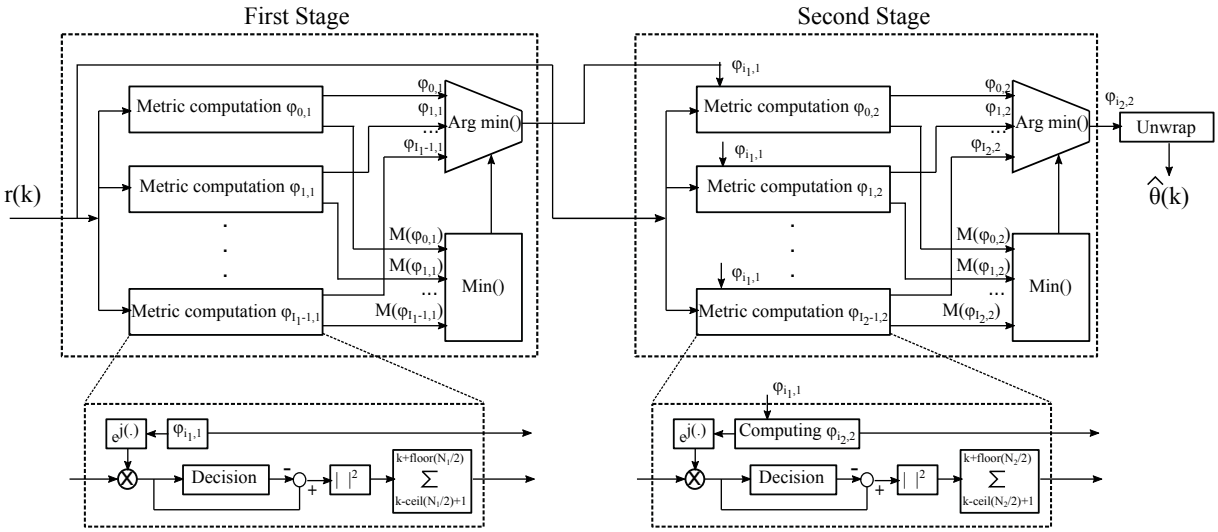

Figure 3.16 – Block diagram for the two-stages BPS algorithm.

$$\varphi_{i_2,2} = \left[\varphi_{i_1,1} - ceil\left(\frac{I_2}{2}\right)\frac{\pi}{2I_1I_2} + \frac{i_2\pi}{2I_1I_2}\right] mod\, \frac{\pi}{2}, \quad where \quad i_2 = 0, 1, ..., I_2. \tag{3.24}$$

The metric distances are calculated in the same way as in conventional one-stage BPS, using the Eq. 3.20, where N_B is replaced by $N1$ and $N2$, which correspond to the noise rejecting window length of the 1^{st} and 2^{nd} stages, respectively.

Complexity reduction is achieved when the total number of test phase angles is reduced regarding classical BPS case. In a two-stages BPS, the test-phase resolution is defined by the product of $I1$ and $I2$, and the entire complexity of an estimator is determined by the sum. For conserving a similar test-phase resolution as a one-stage BPS algorithm, the product between $I1$ and $I2$ must be approximately equal to I, and for decreasing computational efforts, the sum of these two values should be minimized. Considering the 64-QAM format, as an example, one-stage BPS needs 64 test-phase angles (LI *et al.*, 2011), in two-stage BPS, just 8 test-phase angles in each stage are required. This way, the phase estimation resolution remains constant and the total number of test angles reduces to 16, improving the algorithm complexity by a factor of 4.

4 IMPACT OF WIENER PHASE NOISE AND A SINUSOIDAL CARRIER FREQUENCY JITTER ON THE SYSTEM PERFORMANCE

After a theoretical introduction about the main coherent optical systems concepts, transmission impairments, DSP algorithms and principles of semiconductor lasers, this chapter presents the first results of the current work. CFJ has been evaluated in several previous publications (QIU *et al.*, 2013), (PIYAWANNO *et al.*, 2010), (GIANNI *et al.*, 2011), (GIANNI *et al.*, 2013), (KUSCHNEROV *et al.*, 2010), however, its impact on certain high-order modulation formats, e.g. 64 quadrature amplitude modulation (64-QAM), has not been determined. Although the problem of carrier frequency recovery can be modeled analytically in certain conditions, its performance in practical systems depends strongly on the deployed signal processing algorithms. Therefore, this chapter evaluates the impact of CFJ on system performance considering typical frequency and phase recovery algorithms. In particular, it investigates the following operating conditions: QPSK at 32 GBd (100 Gb/s), 16-QAM at 32 GBd (200 Gb/s), 64-QAM at 43 GBd (400 Gb/s) and 64 GBd (600 Gb/s). The system performance is assessed in terms of the optical signal to noise ratio (OSNR) required to achieve a BER=2.4×10^{-2}.

4.1 SYSTEM MODEL

4.1.1 Simulation setup

Figure 4.1 shows the simulation setup implemented in Matlab. The setup is a coherent optical communication system able to work in QPSK, 16-QAM, and 64-QAM. The system supports dual polarization transmission in only one WDM channel centered at $f_0 = 0$ Hertz. From a bit sequence source of variable size, the digital modulator generates an equiprobable symbol constellation according to the modulation alphabet. After that, the symbol sequence passes through a pulse shaping filter that over-samples it into two samples per symbol. In particular, the pulse shaping is performed by a raised cosine filter with a configurable roll-off. Later, the oversampled signal is converted from digital to analog domain by a digital to analog converter (DAC). The DAC output is an electric signal that modulates the laser carrier during the electro-optical conversion. Finally, the

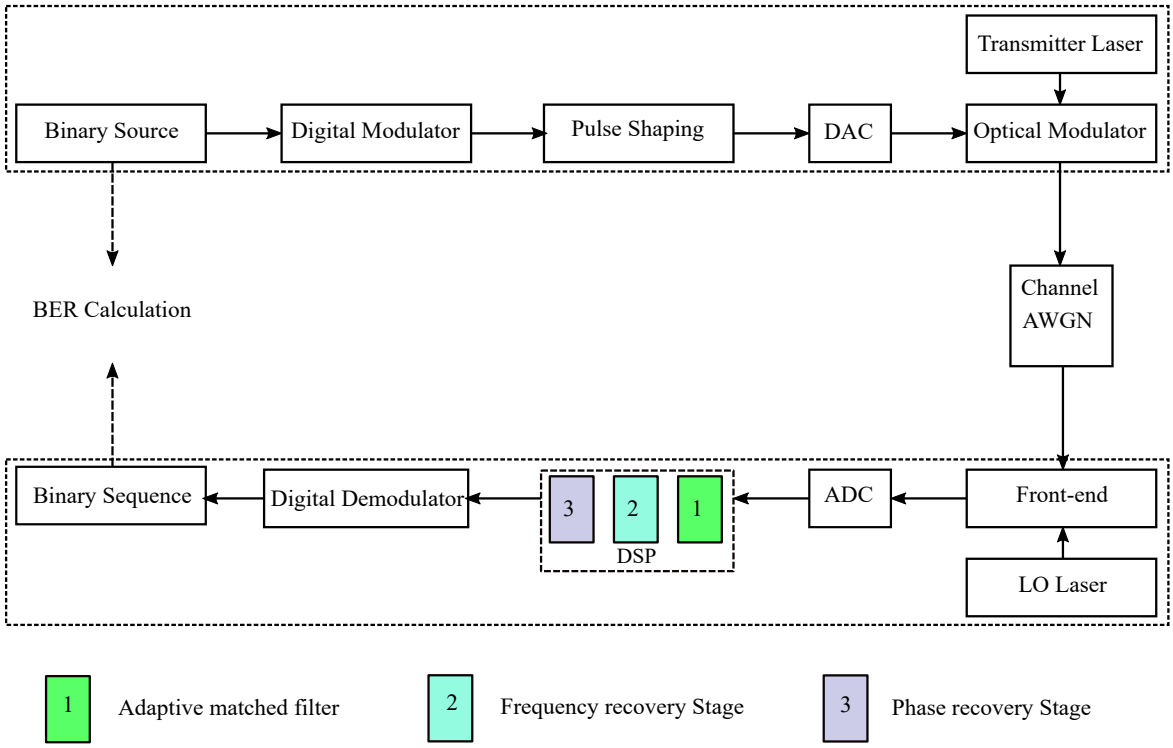

Figure 4.1 – System block diagram.

signal is amplified and, consequently, ASE noise is inserted. In the optical path, the condition of propagation is noise loading (NL), whose effect on the signal is to introduce AWGN. From Eq. 2.14, the amount of noise to add is calculated based on the OSNR value. At the receiver, the optical front-end is performed for dual polarization operation. Receiver noise is considered negligible in all simulations. Once the signals X and Y are in the electric domain, they are digitized by an analog to digital converter (ADC) and sent to the DSP stage for impairments compensation. To compensate the disturbances experienced by the signals during transmission, the DSP block has three stages. First, an adaptive butterfly equalizer is used as a matched filter whose taps are updated dynamically through the RDE algorithm. In the second step, frequency recovery is implemented using the Mth-order power technique and, finally, the two stages BPS algorithm performs the phase recovery process. It should be noted that the primary objective of the simulations is to measure the effects of CFJ on the performance of typical DSP algorithms for carrier recovery.

4.1.2 Simulation parameters

The system performance evaluation is done by means of canonical curves that relate BER with OSNR. Each curve belongs to a specific set of configuration parameters, such as the DAC/ADC bandwidth, laser linewidth, frequency offset, and CFJ. The representative configuration parameters are summarized in Tables 4.1 and 4.2.

Table 4.1 – System configuration parameters.

Binary Source			**DAC/ADC**	
Type	Random		**Bandwidth**	32 GHz
Size	$log_2(M) \times 2^{18}$		**Sample factor**	16
Digital modulator			**Optical modulator**	
Type	Gray		**Type**	IQ
Modulation format	QPSK, 16QAM, 64QAM		**Mode**	Polarization multiplexing
Symbol rate	Configurable			
Pulse shaping			**Channel**	
Type	Raised cosine		**Link**	Noise Loading
Roll-off	0.1		**Type**	AWGN
Sample factor	2 samples per symbol		**Noise variance**	Configurable
Front end			**Digital demodulator and Decisor**	
Type	Dual polarization receiver		**Type**	Gray
Photo-detection	Balanced		**Decision criterion**	Minimum distance

Table 4.2 – System impairments and DSP configuration parameters.

Transmission Impairments		**Impairments Compensation by DSP**	
Additive noise	Amplification noise	**Matched filter**	Number of taps: 15
	Channel noise	Radius directed equalization	Step size: 0.001
Frequency offset	Fixed frequency offset: 1 GHz	**Frequency recovery**	Mth-order power in frequency domain
	Carrier frequency jitter: Configurable		
Phase noise	Transmitter laser linewidth: 100 kHz	**Phase recovery**	N: 100
	Local oscillator linewidth: 100 kHz	Two-stages BPS	$I_1 = I_2$: 30

Transmitter and local oscillator carrier signals have been simulated according to:

$$S^{tx}(k) = Ae^{j\left\{\left[2\pi\left(\frac{\Delta_A}{2}sin(2\pi f_A k T_{sa})\right)\right]kT_{sa}+\theta^{tx}(k)\right\}}, \tag{4.1}$$

$$S^{LO}(k) = Ae^{j\left\{\left[2\pi\left(\Delta F_1+\frac{\Delta_A}{2}sin(2\pi f_A k T_{sa}+\phi_J)\right)\right]kT_{sa}+\theta^{LO}(k)\right\}}, \tag{4.2}$$

where $\theta(k)$ is the Wiener-distributed phase noise, ΔF_1 is the frequency offset and ϕ_j is the phase shift between transmitter and local oscillator jitters, set to π as a worst-case condition. Parameters Δ_A and f_A are the CFJ amplitude and frequency. Both values were configured according to Table 4.3, which contains representative values used by component manufacturers.

Table 4.3 – Parameter setup for the carrier frequency jitter.

Index	**Peak-to-Peak [MHz]**	**Frequency [kHz]**
1	70,711	0,00001
2	40	0,01
3	22,361	10
4	22,361	100
5	22,361	35
6	100	35
7	70,711	35
8	70,711	23
9	70,711	12
10	70,711	70
11	200	35

4.2 SYSTEM PERFORMANCE RESULTS

Figures 4.2, 4.3, 4.4 and 4.5 show the performance achieved by the four simulated operating conditions. There are twelve curves in each figure: the black solid curve indicates the theoretical performance, while the others correspond to the scenarios presented in Table 4.3.

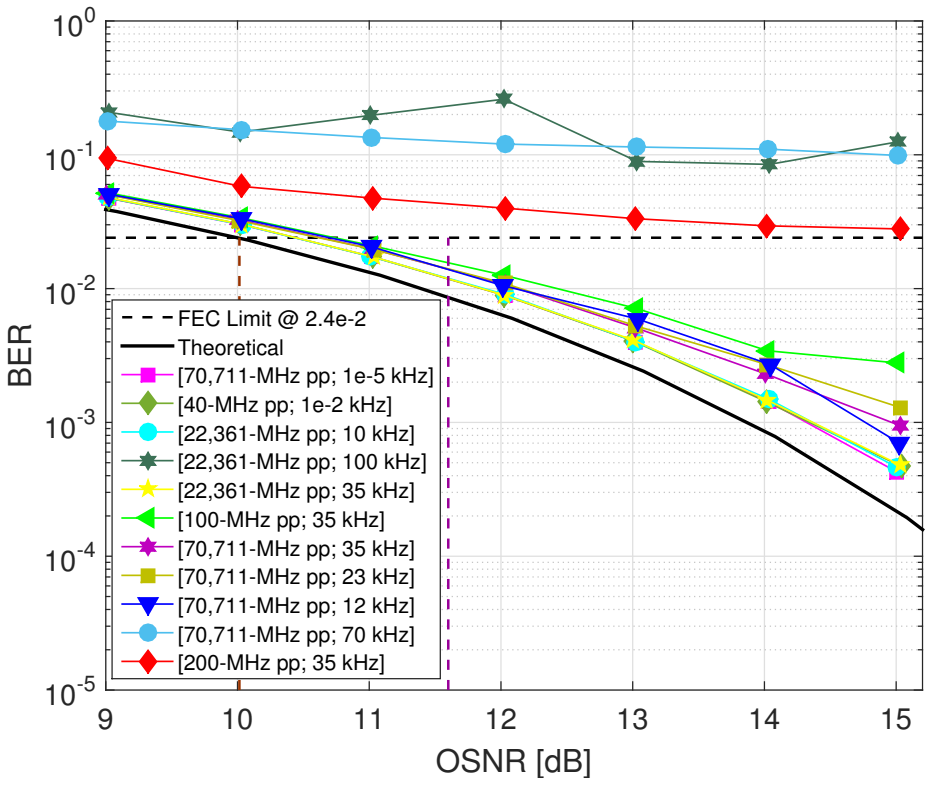

Figure 4.2 – QPSK at 32 GBd.

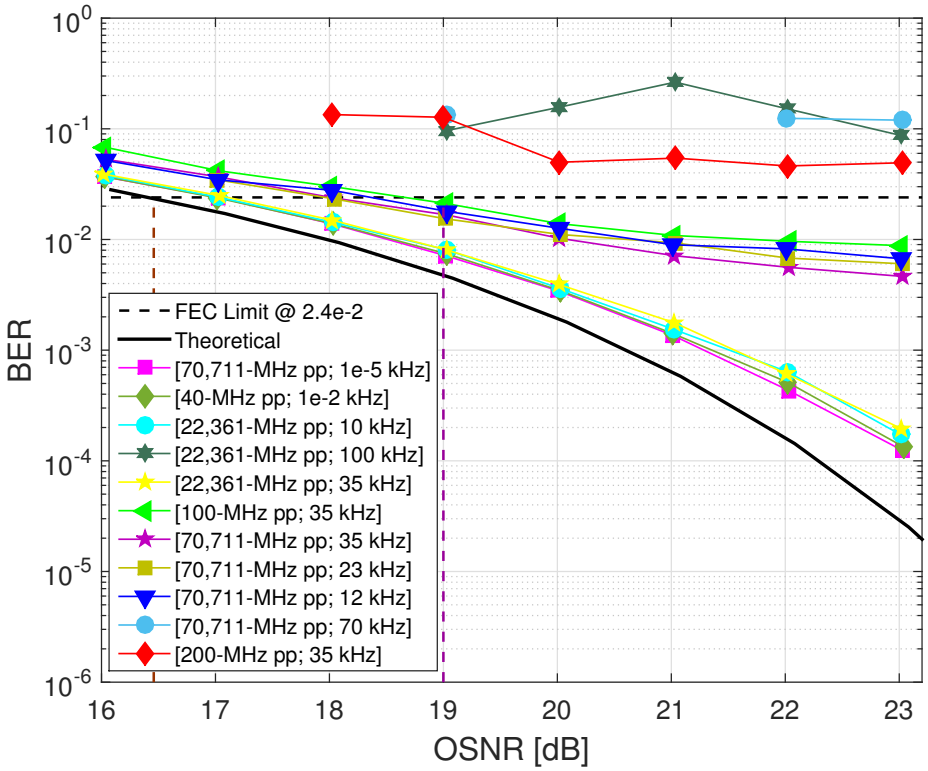

Figure 4.3 – 16-QAM at 32 GBd.

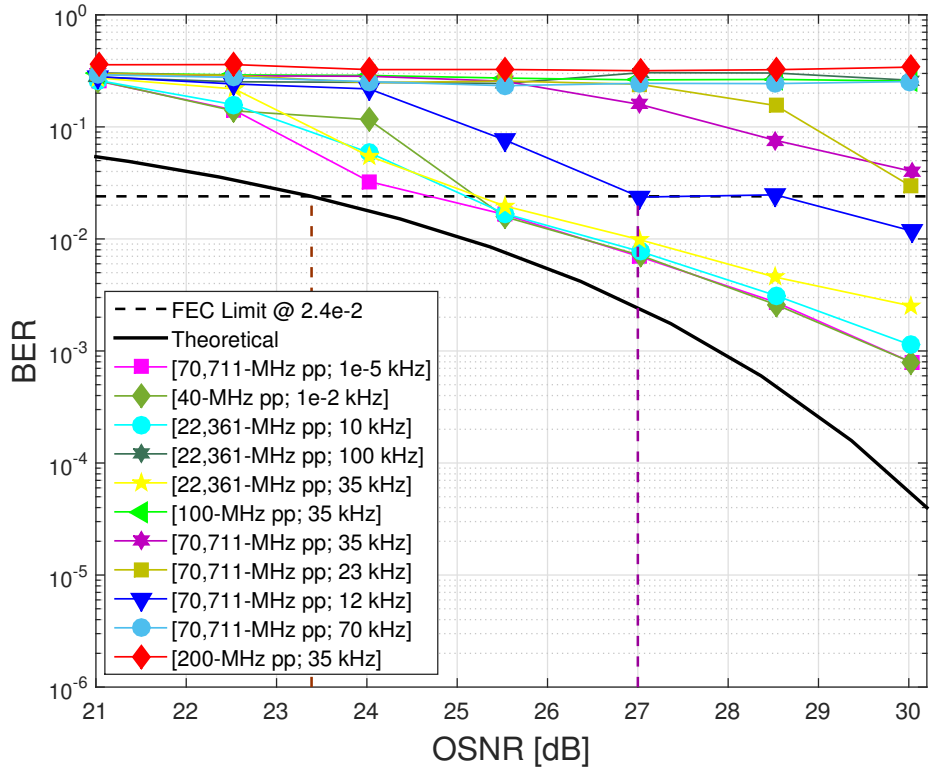

Figure 4.4 – 64-QAM at 43 GBd.

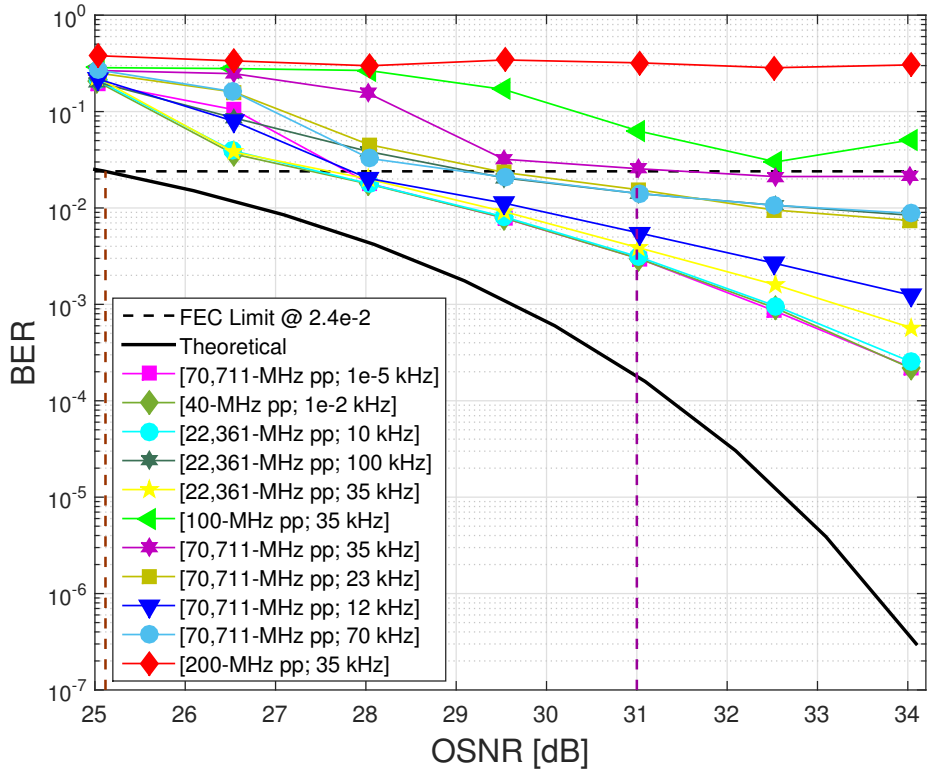

Figure 4.5 – 64-QAM at 64 GBd.

The three dashed lines represent important limits of reference. The black horizontal line points out the FEC limit at a BER=2.4×10^{-2}. The brown vertical dashed line indicates the theoretical OSNR required for this FEC limit, while the purple one corresponds to the maximum acceptable required OSNR suggested by manufacturers (J. D. Reis et al., 2015).

Figure 4.2 shows the results for QPSK modulation at 32 GBd. Three of the eleven cases exhibit OSNR penalties exceeding the OSNR limit threshold. These cases correspond to CFJ configurations with a large peak-to-peak amplitude, a high oscillation frequency, and both conditions. It is interesting to observe that a low frequency can compensate a large peak-to-peak amplitude. This is the case of a CFJ with 100 MHz amplitude and 35 kHz frequency. Unlike, a high CFJ frequency cannot be easily compensated by a low amplitude, as evidenced in the curve of 22.36 MHz amplitude and 100 kHz frequency. The simulated performance was very similar for the remaining eight cases, with penalties ranging between 0.48 and 0.73 dB. A similar behavior was observed for 16-QAM modulation at 32 GBd in which the minimum required performance was not achieved for the same three cases. For the other eight cases, although the performance degraded with respect to QPSK, the curves still attained the FEC limit in the allowed region, with penalties in the range between 0.54 to 2.24 dB.

Increasing the symbol rate and the modulation order severely degrade the system performance, as it can be observed in Figures 4.4 and 4.5. Although an increase in symbol rate alleviates phase distortions because of shorter sampling times, raising the order of the modulation format degrades the system performance due to a small Euclidean distance between constellation points. For 64-QAM at 43 GBd, only four of the eleven simulated scenarios achieved the recommended OSNRs. As expected, 64-QAM at 64 GBd is less susceptible to CFJ, and eight cases exhibited satisfactory performance.

The performance degradation due to CFJ was also evaluated using OSNR penalty curves. The OSNR penalty values are obtained for the FEC limit at BER=2.4×10^{-2} subtracting the theoretical OSNR to the simulated OSNR at this point for each curve. Figures 4.7, 4.8, 4.9, and 4.10 show the 3D graphs that relate the OSNR penalty to a certain amplitude and frequency of the jitter. The color bar of Figure 4.6 associates the color of the line with the amount of the penalty. Orange represents the cases with higher penalty and the red the cases in which the curve does not reach the BER limit in the studied OSNR range or the penalty exceeds the suggested value.

Figure 4.6 – Penalty indicator.

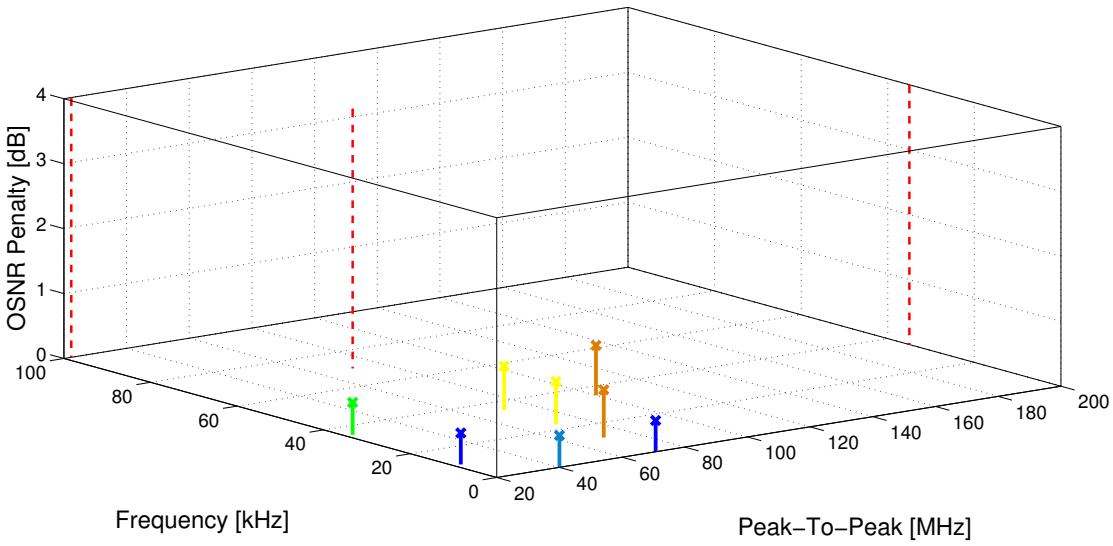

Figure 4.7 – QPSK OSNR penalty.

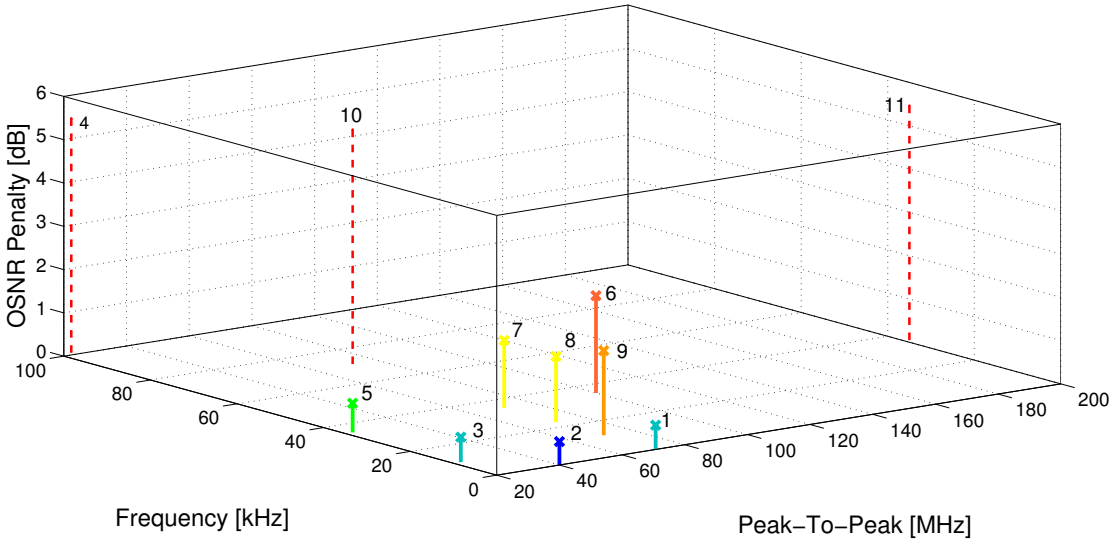

Figure 4.8 – 16-QAM OSNR penalty.

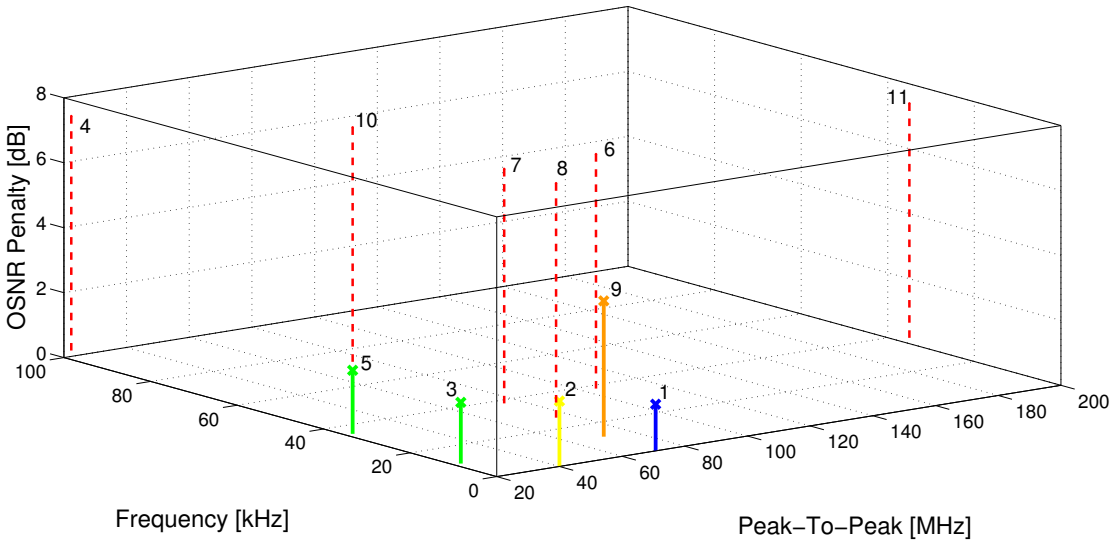

Figure 4.9 – 64-QAM at 43 GBd OSNR penalty.

Table 4.4 summarizes the OSNR penalties obtained for each case. The hyphen indicates scenarios for which the BER limit was not achieved, while the cells in red text indicate that for these scenarios the penalty exceeds the suggested value. It is possible to observe that the system behavior is critically influenced by the laser imperfections related to the frequency fluctuations. The system performance depends on the modeling and configuration of the carrier frequency jitter since the degradation is directly proportional to the peak-to-peak amplitude and to the frequency with which the laser operating frequency varies. These are not surprising results because it is reasonable to expect that the faster the frequency offset changes, the less effective are the frequency and phase recovery processes since the DSP algorithms are not intentionally designed for

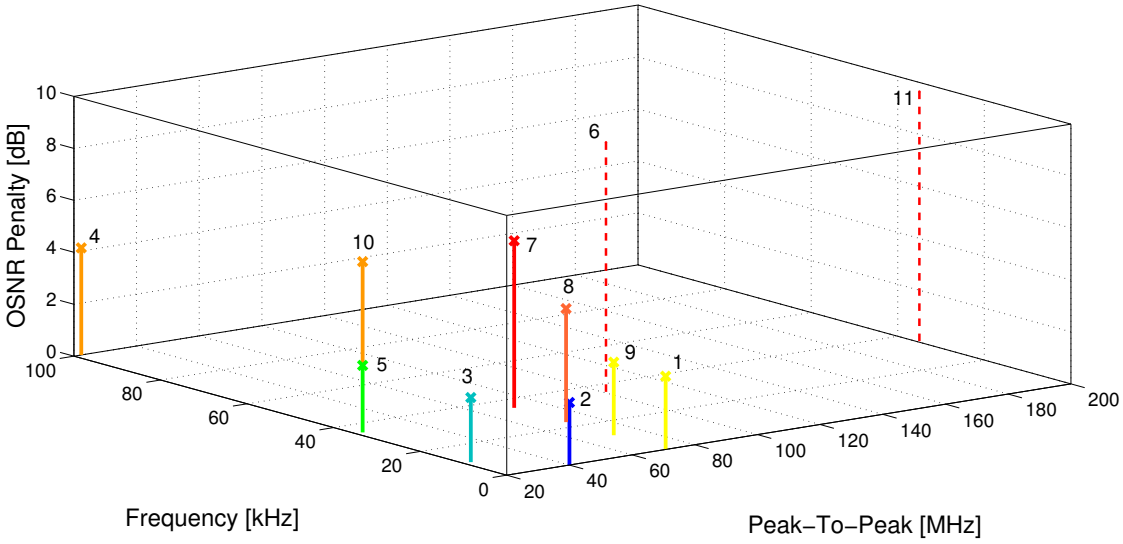

Figure 4.10 – 64-QAM at 64 GBd OSNR penalty.

Table 4.4 – Obtained OSNR penalties.

CARRIER FREQUENCY JITTER			**PENALTY AT BER = 2.4e-2**			
Number	**Peak-To-Peak [MHz]**	**Frequency [kHz]**	**QPSK**	**16-QAM**	**64-QAM at 43 GBd**	**64-QAM at 64 GBd**
1	70,711	0,00001	0,4834	0,5628	1,4369	2,8190
2	40	0,01	0,4936	0,5425	2,0158	2,4080
3	22,361	10	0,4841	0,5766	1,8852	2,4840
4	22,361	100	-	-	-	4,1230
5	22,361	35	0,4967	0,6721	1,9538	2,5760
6	100	35	0,7682	2,2471	-	-
7	70,711	35	0,6771	1,5594	-	6,4320
8	70,711	23	0,6627	1,5180	-	4,3710
9	70,711	12	0,7357	1,9536	4,1816	2,8110
10	70,711	70	-	-	-	4,0240
11	200	35	-	-	-	-

frequency offset tracking. As expected, the CFJ impact is more prominent for high-order modulation formats, which inherently have a smaller phase perturbations tolerance due to the lower spacing between adjacent constellation points. On the other hand, for the same modulation format, the higher symbol rate improved the system robustness against phase perturbations as a consequence of the proportional relation between phase noise and symbol period. It is interesting to observe that cases 4 and 10, which exhibit the highest CFJ frequency (100 and 70 kHz, respectively), could not be recovered with a QPSK constellation at 32 GBd, but were recovered with a 64-QAM constellation at 64 GBd. However, case 6, which has the highest CFJ amplitude (100 MHz), was recovered for QPSK at 32 GBd, but not for 64-QAM at 64 GBd. This indicates an improved robustness against CFJ frequency in higher rates and modulation orders, but some susceptibility to the CFJ amplitude. These preliminary results about system performance clearly show the need of taking into account the instability of the laser operating frequency, a phenomenon which

is inevitable in practical implementations. For this reason, it is imperative that the DSP algorithms be able to deal with the carrier frequency jitter for proper system operation within the established performance limits.

5 IMPACT OF EXPERIMENTAL PHASE NOISE AND CARRIER FREQUENCY JITTER ON THE SYSTEM PERFORMANCE

In Chapter 4, the impact of phase noise and CFJ on the performance of optical receivers with high-order modulation formats was carried out by simulation. Phase noise was modeled by a discrete Wiener process, while CFJ was modeled as a sinusoidal waveform. This Chaper evaluates the system impact of these two imperfections using experimental data. However, a first question is how to characterize the laser linewidth and the CFJ profile from experimental traces. Linewidth estimation for narrow-linewidth lasers is not a trivial task. Therefore, we start with a theoretical review of linewidth estimation methods. After that, we show that current linewidth estimation methods diverge when the laser is subject of a high CFJ. Lastly, we show how to combine phase noise and CFJ metrics to predict the system performance.

5.1 LINEWIDTH ESTIMATION OF SEMICONDUCTOR LASERS

Coherent optical communications increases the system spectral efficiency through the use of high order modulation formats. The incorporation of such modulation formats demands a more complex detector along with a digital signal processing stage for system impairments compensation. In addition, multilevel modulation approaches are more susceptible to phase noise, which can impair the transmission. Chapter 3 emphasized how the laser linewidth is strongly related to phase noise intensity, so that the greater the linewidth, the greater the degradation of symbol phases. As spectrally efficient modulation formats are relatively intolerant to laser phase noise, the interest in laser linewidth estimation methods raised (MATSUDA *et al.*, 2014). Optical precision metrology and high-resolution spectroscopy are other areas that require small laser linewidths (ZHOU *et al.*, 2008).

In general, in phase noise sensitive systems, the linewidth of involved lasers has an impact on the bit error rate performance, and in particular on the carrier phase recovery process of coherent optical systems. Manufacturers are focusing their efforts on the fabrication of very narrow linewidth lasers. However, accurate linewidth estimation techniques are also required. Nowadays, the laser characterization becomes considerably arduous because currently available methods for these measurements present a limited

resolution. As a consequence, manufactures of narrow linewidth lasers can only provide approximate values of their linewidths. This section presents a general review of the methods for linewidth estimation and brings up the main concepts related to this challenge.

The linewidth estimation process is typically divided into two parts. The first stage generates a photo-current from the beating between the laser under test and a copy of itself delayed by a certain time. After that, this photo-current is analyzed in detail through estimation techniques in order to obtain the final linewidth estimate. There are several mechanisms to carry out both stages, as presented below.

5.1.1 Techniques for photo-current generation

The basic idea of this stage is to convert the optical phase or frequency fluctuations into variations of light intensity in a Mach-Zehnder interferometer (LUDVIGSEN *et al.*, 1998). There are three well-known methods for obtaining such photo-current: delayed self-homodyne (DSHO), delayed self-heterodyne (DSHT) and delayed self-heterodyne with coherent receiver techniques. All of them involve the beating between an optical field and one copy of itself delayed by a certain time.

5.1.1.1 Delayed self-homodyne (DSHO)

In a DSHO setup, the laser signal is firstly split by a 3 dB coupler into two paths as shown in Figure 5.1 (HUYNH *et al.*, 2012).

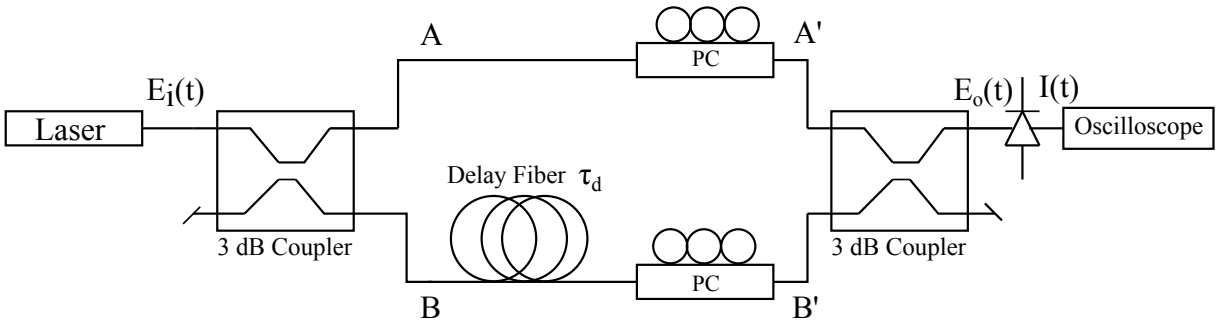

Figure 5.1 – Delayed self-homodyne setup.

As mentioned in (HUYNH *et al.*, 2012), the electric field of the optical signal from a single-mode laser $E_i(t)$, with negligible amplitude noise, can be expressed in complex notation as:

$$E_i(t) = \sqrt{P}\, e^{j[\omega_o t + \Phi(t)]}, \tag{5.1}$$

where P is the laser output power, ω_o the optical angular frequency and $\Phi(t)$ the laser phase noise in continuous time notation. After splitting, one of the two beams remains unaltered meanwhile the other passes through a fiber delay that introduces a time delay

of τ_d. Usually, the optical delay is chosen to be long enough to make the phase dynamics of the interfering fields become uncorrelated on the detector. A polarization controller (PC) is used to align the lasers polarization states at the photo-detector input. Therefore, using Eq. 2.26 for the 3 dB coupler transfer function, the fields at A' and B' in Figure 5.1 are respectively:

$$A'(t) = \frac{\sqrt{P}}{\sqrt{2}}\, e^{j[\omega_o t + \Phi(t)]}, \tag{5.2}$$

$$B'(t) = \frac{\sqrt{P}}{\sqrt{2}}\, e^{j[\omega_o (t+\tau_d) + \Phi(t+\tau_d)]}. \tag{5.3}$$

Subsequently, the two signals at A' and B' are again combined by means of a 3 dB coupler and the resulting field is photo-detected. The total input electric field on the detector E_o is given by (ZHOU *et al.*, 2008):

$$E_o(t) = \frac{1}{2}\sqrt{P}\, e^{j[\omega_o t + \Phi(t)]} + \frac{1}{2}\sqrt{P}\, e^{j[\omega_o (t+\tau_d) + \Phi(t+\tau_d)]}. \tag{5.4}$$

The intensity of the photo-detector output is:

$$I(t) = R\,|E_o(t)|^2, \tag{5.5}$$

where R is the photo-detector responsivity. Then, from Eq. 2.47 the resulting photo-current obtained by delayed self-homodyne method is as follows:

$$\begin{aligned}
I(t) &= R\left\{\frac{1}{4}P + \frac{1}{4}P + 2\,\Re\left[\frac{1}{2}\sqrt{P}\, e^{j[\omega_o t + \Phi(t)]} \times \frac{1}{2}\sqrt{P}\, e^{-j[\omega_o (t+\tau_d) + \Phi(t+\tau_d)]}\right]\right\} \\
&= R\left\{\frac{1}{2}P + \frac{1}{2}P\,\Re\left[e^{j\omega_o t}\, e^{j\Phi(t)}\, e^{-j\omega_o t}\, e^{-j\omega_o \tau_d}\, e^{-j\Phi(t+\tau_d)}\right]\right\} \\
&= R\left\{\frac{1}{2}P + \frac{1}{2}P\,\Re\left[e^{j\Phi(t)}\, e^{-j\omega_o \tau_d}\, e^{-j\Phi(t+\tau_d)}\right]\right\} \\
&= R\,\frac{1}{2}\left\{P + P\,\Re\left[e^{j(\Phi(t) - \omega_o \tau_d - \Phi(t+\tau_d))}\right]\right\} \\
&= R\,\frac{1}{2}\left\{P + P\,\Re\left[\cos(\Phi(t) - \omega_o \tau_d - \Phi(t+\tau_d)) + j\,\sin(\Phi(t) - \omega_o \tau_d - \Phi(t+\tau_d))\right]\right\} \\
&= R\,P\,\frac{1}{2}\left\{1 + 1\,\cos\left[\Phi(t) - \omega_o \tau_d - \Phi(t+\tau_d)\right]\right\}
\end{aligned} \tag{5.6}$$

DSHO presents important disadvantages. First, (ZHOU *et al.*, 2008) makes reference to low frequency noise in the detected intensity spectrum that disturbs the measurements in the region near to direct current (DC). Besides, (LUDVIGSEN *et al.*, 1998) remarks that the DSHO technique precludes the use of a standard RF spectrum analyzer to measure the spectrum of the photo-current fluctuations.

5.1.1.2 Delayed self-heterodyne (DSHT)

The DSHT method is proposed in order to avoid low frequency noise contributions that affect the spectrum visualization in the DSHO approach. In this case, an acousto-optic modulator (AOM) is used to shift the spectrum up in frequency of the non-delayed beam. The DSHT diagram is shown in Figure 5.2.

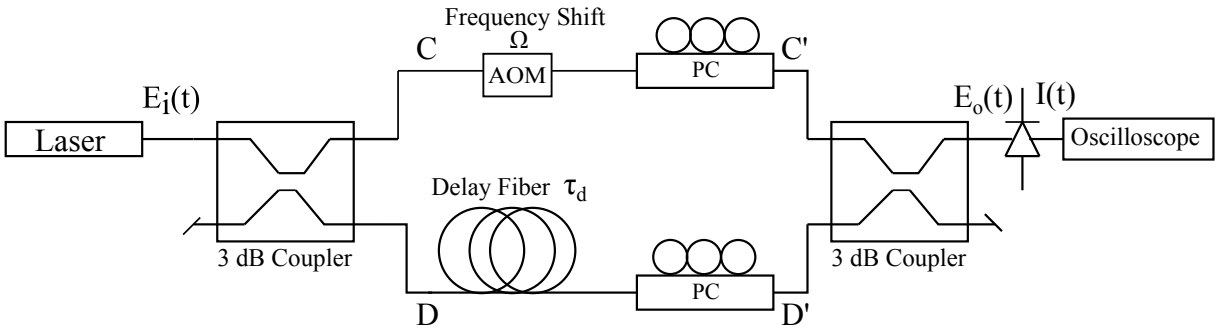

Figure 5.2 – Delayed self-heterodyne setup.

Fields at C' and D' are:

$$C'(t) = \frac{\sqrt{P}}{\sqrt{2}}\, e^{j[(\omega_o+\Omega)t+\Phi(t)]}, \tag{5.7}$$

$$D'(t) = \frac{\sqrt{P}}{\sqrt{2}}\, e^{j[\omega_o(t+\tau_d)+\Phi(t+\tau_d)]}, \tag{5.8}$$

where Ω denotes the frequency shift. From Eqs. 5.7 and 5.8 the incident field on the photo-detector is given by (ZHOU *et al.*, 2008), (RICHTER *et al.*, 1986):

$$E_o(t) = \frac{1}{2}\sqrt{P}\, e^{j[(\omega_o+\Omega)t+\Phi(t)]} + \frac{1}{2}\sqrt{P}\, e^{j[\omega_o(t+\tau_d)+\Phi(t+\tau_d)]}. \tag{5.9}$$

The current of the photo-diode output is proportional to the intensity of the incident field, therefore, using Eqs. 2.47 and 5.5 the detected photo-current is given by:

$$\begin{aligned}
I(t) &= R\left\{\frac{1}{4}P + \frac{1}{4}P + 2\,\Re\left[\frac{1}{2}\sqrt{P}\, e^{j[(\omega_o+\Omega)t+\Phi(t)]} \times \frac{1}{2}\sqrt{P}\, e^{-j[\omega_o(t+\tau_d)+\Phi(t+\tau_d)]}\right]\right\} \\
&= R\left\{\frac{1}{2}P + \frac{1}{2}P\,\Re\left[e^{j\omega_o t}\, e^{j\Omega t}\, e^{j\Phi(t)}\, e^{-j\omega_o t}\, e^{-j\omega_o\tau_d}\, e^{-j\Phi(t+\tau_d)}\right]\right\} \\
&= R\left\{\frac{1}{2}P + \frac{1}{2}P\,\Re\left[e^{j\Omega t}\, e^{j\Phi(t)}\, e^{-j\omega_o\tau_d}\, e^{-j\Phi(t+\tau_d)}\right]\right\} \\
&= R\,\frac{1}{2}\left\{P + P\,\Re\left[e^{j(\Omega t+\Phi(t)-\omega_o\tau_d-\Phi(t+\tau_d))}\right]\right\} \\
&= R\,\frac{1}{2}\left\{P + P\,\Re\left[\cos(\Omega t+\Phi(t)-\omega_o\tau_d-\Phi(t+\tau_d)) + j\,\sin(\Omega t+\Phi(t)-\omega_o\tau_d-\Phi(t+\tau_d))\right]\right\} \\
&= R\,P\,\frac{1}{2}\left\{1 + 1\,\cos\left[\Omega t+\Phi(t)-\omega_o\tau_d-\Phi(t+\tau_d)\right]\right\},
\end{aligned} \tag{5.10}$$

5.1.1.3 Delayed self-heterodyne with coherent receiver

Delayed self-heterodyne with coherent receiver adds a 2x4 90° hybrid in the receiver for beating the signal with its delayed version. After the hybrid, the fields are photo-detected by a pair of balanced photo-detector as discussed in Chapter 2. Coherent detection can, as a general principle, increase the sensitivity of measurements (PIELS *et al.*, 2015) and allows to deploy techniques that will be part of coherent optical transceivers. Figure 5.3 shows the block diagram of the method.

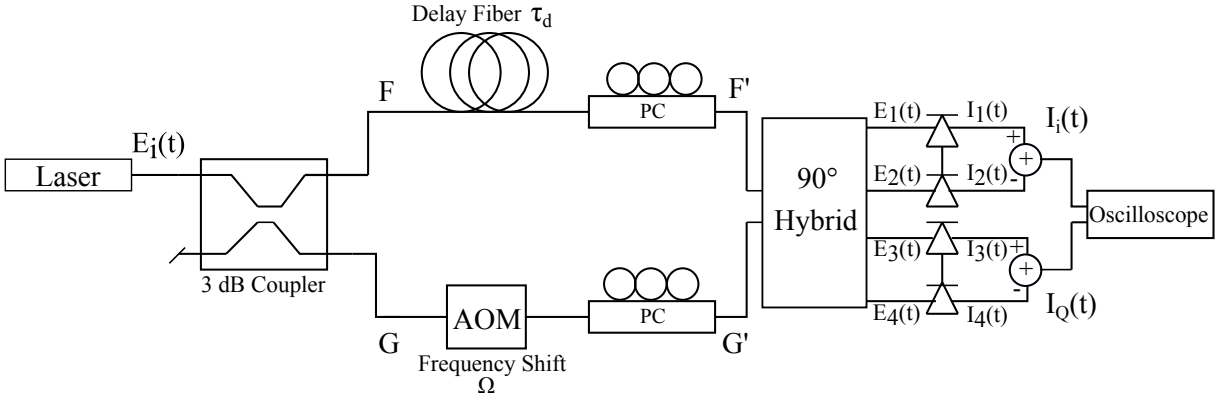

Figure 5.3 – Delayed self-heterodyne with coherent receiver setup.

The electrical fields at points F' and G' are given by:

$$F'(t) = \frac{\sqrt{P}}{\sqrt{2}}\, e^{j[\omega_o(t+\tau_d)+\Phi(t+\tau_d)]}, \tag{5.11}$$

$$G'(t) = \frac{\sqrt{P}}{\sqrt{2}}\, e^{j[(\omega_o+\Omega)t+\Phi(t)]}. \tag{5.12}$$

Thus, from Eq. 2.39 90° hybrid outputs are related to inputs as follows:

$$\begin{bmatrix} E_1(t) \\ E_2(t) \\ E_3(t) \\ E_4(t) \end{bmatrix} = \frac{1}{2} \begin{bmatrix} 1 & e^{j\frac{\pi}{2}} \\ 1 & -e^{j\frac{\pi}{2}} \\ 1 & 1 \\ 1 & -1 \end{bmatrix} \begin{bmatrix} F'(t) \\ G'(t) \end{bmatrix}. \tag{5.13}$$

Therefore, fields at E_1, E_2, E_3 and E_4 are expressed:

$$E_1(t) = \frac{1}{2}\left(F'(t) + G'(t)\, e^{j\frac{\pi}{2}}\right), \tag{5.14}$$

$$E_2(t) = \frac{1}{2}\left(F'(t) - G'(t)\, e^{j\frac{\pi}{2}}\right), \tag{5.15}$$

$$E_3(t) = \frac{1}{2}\left(F'(t) + G'(t)\right), \tag{5.16}$$

$$E_4(t) = \frac{1}{2}\left(F'(t) - G'(t)\right). \tag{5.17}$$

Through Eqs. 5.5 and 2.47, the four photo-currents are obtained as:

$$\begin{aligned} I_1(t) &= R\,|\frac{1}{2}\left(F'(t) + G'(t)\,e^{j\frac{\pi}{2}}\right)|^2 \\ &= R\left\{\frac{P}{8} + \frac{P}{8} + 2\,\Re\left[\frac{P}{8}\,e^{j[\omega_o(t+\tau_d)+\Phi(t+\tau_d)]}\,e^{-j\left[(\omega_o+\Omega)t+\Phi(t)+\frac{\pi}{2}\right]}\right]\right\} \\ &= R\,P\,\frac{1}{4}\left\{1 + \Re\left[e^{j\omega_o t}\,e^{j\omega_o\tau_d}\,e^{j\Phi(t+\tau_d)}\,e^{-j\omega_o t}\,e^{-j\Omega t}\,e^{-j\Phi(t)}\,e^{-j\frac{\pi}{2}}\right]\right\} \\ &= R\,P\,\frac{1}{4}\left\{1 + \Re\left[e^{j\left(\omega_o\tau_d+\Phi(t+\tau_d)-\Omega t-\Phi(t)-\frac{\pi}{2}\right)}\right]\right\} \\ &= R\,P\,\frac{1}{4}\left\{1 + \cos\left(\omega_o\tau_d + \Phi(t+\tau_d) - \Omega t - \Phi(t) - \frac{\pi}{2}\right)\right\}, \end{aligned} \tag{5.18}$$

$$\begin{aligned} I_2(t) &= R\,|\frac{1}{2}\left(F'(t) - G'(t)\,e^{j\frac{\pi}{2}}\right)|^2 \\ &= R\left\{\frac{P}{8} + \frac{P}{8} + 2\,\Re\left[-\frac{P}{8}\,e^{j[\omega_o(t+\tau_d)+\Phi(t+\tau_d)]}\,e^{-j\left[(\omega_o+\Omega)t+\Phi(t)+\frac{\pi}{2}\right]}\right]\right\} \\ &= R\,P\,\frac{1}{4}\left\{1 - \cos\left(\omega_o\tau_d + \Phi(t+\tau_d) - \Omega t - \Phi(t) - \frac{\pi}{2}\right)\right\}, \end{aligned} \tag{5.19}$$

$$\begin{aligned} I_3(t) &= R\,|\frac{1}{2}\left(F'(t) + G'(t)\right)|^2 \\ &= R\left\{\frac{P}{8} + \frac{P}{8} + 2\,\Re\left[\frac{P}{8}\,e^{j[\omega_o(t+\tau_d)+\Phi(t+\tau_d)]}\,e^{-j[(\omega_o+\Omega)t+\Phi(t)]}\right]\right\} \\ &= R\,P\,\frac{1}{4}\left\{1 + \Re\left[e^{j\omega_o t}\,e^{j\omega_o\tau_d}\,e^{j\Phi(t+\tau_d)}\,e^{-j\omega_o t}\,e^{-j\Omega t}\,e^{-j\Phi(t)}\right]\right\} \\ &= R\,P\,\frac{1}{4}\left\{1 + \Re\left[e^{j(\omega_o\tau_d+\Phi(t+\tau_d)-\Omega t-\Phi(t))}\right]\right\} \\ &= R\,P\,\frac{1}{4}\left\{1 + \cos\left(\omega_o\tau_d + \Phi(t+\tau_d) - \Omega t - \Phi(t)\right)\right\}, \end{aligned} \tag{5.20}$$

$$\begin{aligned} I_4(t) &= R\,|\frac{1}{2}\left(F'(t) + G'(t)\right)|^2 \\ &= R\left\{\frac{P}{8} + \frac{P}{8} + 2\,\Re\left[-\frac{P}{8}\,e^{j[\omega_o(t+\tau_d)+\Phi(t+\tau_d)]}\,e^{-j[(\omega_o+\Omega)t+\Phi(t)]}\right]\right\} \\ &= R\,P\,\frac{1}{4}\left\{1 - \cos\left(\omega_o\tau_d + \Phi(t+\tau_d) - \Omega t - \Phi(t)\right)\right\}. \end{aligned} \tag{5.21}$$

Finally, the in-phase and quadrature components are given by the following photo-currents:

$$\begin{aligned} I_i(t) &= I_1(t) - I_2(t) \\ &= R\,P\,\frac{1}{2}\cos\left(\omega_o\tau_d + \Phi(t+\tau_d) - \Omega t - \Phi(t) - \frac{\pi}{2}\right), \end{aligned} \tag{5.22}$$

$$\begin{aligned} I_Q(t) &= I_3(t) - I_4(t) \\ &= R\,P\,\frac{1}{2}\cos\left(\omega_o\tau_d + \Phi(t+\tau_d) - \Omega t - \Phi(t)\right). \end{aligned} \tag{5.23}$$

Once the photo-current is available, signal processing techniques are applied. In this work, is used the delayed self-heterodyne with coherent receiver method for all measurements. Thus, at the coherent receiver output, an optical field E_d is reconstructed from the quadrature and in-phase photo-currents. We will use this approach to estimate laser perturbations in the rest of this work.

5.1.2 Linewidth estimation from the reconstructed optical field after a coherent receiver

The laser linewidth estimation is realized in a DSP stage after the photo-detection process. Figure 5.4 shows four of the current methods for linewidth estimation based on the optical field, E_d, obtained in the previous stage (KIKUCHI; IGARASHI, 2011).

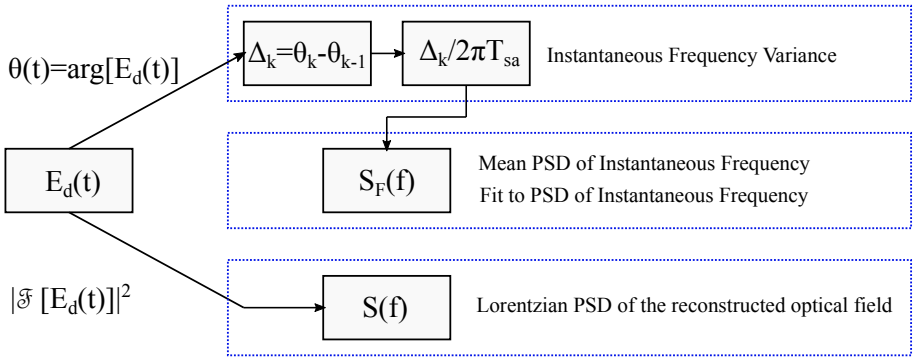

Figure 5.4 – Techniques for linewidth estimation.

5.1.2.1 Lorentzian spectrum

The first and simplest approach to obtain a coarse laser linewidth estimate is based on the power spectral density $S(f)$ of the reconstructed optical field. This method is applied to lasers under the assumption of a Lorentzian lineshape originated from a Wiener phase noise. As it is shown in figure 5.4, the PSD is obtained through the squared of the Fourier transform of the field. Once, $S(f)$ is accurately calculated, the laser linewidth corresponds to the FWHM of the spectrum. The PDS lineshape is strongly related to the time delay introduced by the fiber delay. In (RICHTER *et al.*, 1986) simulation results of the PSD for several values of τ_d can be found. According to this work, the

spectrum is strictly Lorentzian for the time delay which makes phases of the optical field become totally decorrelated. Otherwise, if the phases of the signal to beat are statistically correlated, the spectrum complexity increases due to oscillations in both lateral regions of the central peak. The Lorentzian spectrum approach presents limitations for linewidth estimation because the measurement performance depends on FFT resolution used in the DSP. The higher the FFT resolution, the greater computational effort. Figure 5.5 shows the form of a typical Lorentzian PSD.

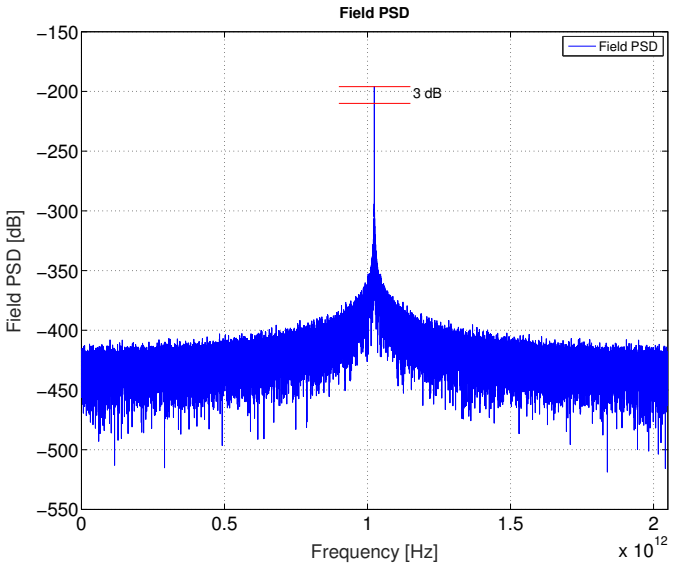

Figure 5.5 – Lorentzian power spectrum.

5.1.2.2 Instantaneous frequency variance

In this method, the introduction of the concept of frequency modulation (FM) noise is a relevant guide for phase noise characterization. As it is observed in Figure 5.4, the first step to execute is to obtain the phase noise sequence by getting the argument of the field samples. Then, the instantaneous frequency is calculated from the variations over time of the phase normalized by the time between samples. Using a discrete time notation and in concordance with (MAHER; THOMSEN, 2011), the instantaneous frequency $f_i(k)$ is defined as:

$$f_i(k) = \frac{1}{2\pi T_{sa}} \arg\left\{E_d(k)\, E_d^*(k-1)\right\}, \tag{5.24}$$

where T_{sa} is the time between samples. Then, the linewidth estimate given by the method is (MAHER; THOMSEN, 2011), (CHEN *et al.*, 2011):

$$\Delta_\nu = 2\pi T_{sa}\, var[f_i(k)]. \tag{5.25}$$

From Eq. 5.25, and taking into account that Δ_ν is twice the linewidth of the laser, the final laser linewidth estimate is:

$$\Delta_{LW} = \pi T_{sa}\, var[f_i(k)]. \tag{5.26}$$

The instantaneous frequency variance technique is suitable in the case of low additive noise.

5.1.2.3 Mean of power spectral density of instantaneous frequency

The FM spectrum $S_F(f)$ corresponds to the PSD of the instantaneous frequency, thus:

$$S_F(f) = |\mathfrak{F}[f_i(t)]|^2, \tag{5.27}$$

In an ideal context, the FM spectrum follows a white noise behavior, that is, it presents a flat PSD at all frequencies. However, the presence of different phase noise sources forces the assumption of a realistic non-white FM spectrum. At this point, it is imperative to stand out the works in (PIELS *et al.*, 2015), (OLMEDO *et al.*, 2016) and (KAKKAR., 2017), in which a detailed description about FM spectrum regimes is presented. According to (ZHOU *et al.*, 2008), (PIELS *et al.*, 2015), (OLMEDO *et al.*, 2016) and (KAKKAR., 2017), the spectrum of the instantaneous frequency is composed by three main contributions:

$$S_F(f) = S_{F1}(f) + S_{F2}(f) + S_{F3}(f) \tag{5.28}$$

where $S_{F1}(f)$ is the white noise spectrum caused by spontaneous emission, $S_{F2}(f)$ is the high frequency spectrum originated from the relaxation oscillations and, finally, $S_{F3}(f)$ is a low frequency noise source known as $1/f$ noise. If the laser phase noise is ideally described by a random walk, the linewidth enhancement is induced only by the white FM noise. Therefore, the low and high frequency noises can be neglected. In this context, the FM noise is white and its spectral density is given theoretically as (KIKUCHI; IGARASHI, 2011), (HUYNH *et al.*, 2012), (KIKUCHI, 1989):

$$S_F(f) = \Delta_v/\pi. \tag{5.29}$$

In a practical context, during the DSP stage for linewidth estimation, the available FM spectrum presents all noise contributions, as seen in Figure 5.6a for an experimental signal. Hence, two steps have to be carried out, as shown in Figure 5.6. Firstly, high frequency components are eliminated for neglecting the relaxation oscillations contribution, (see Figure 5.6b). Subsequently, the flat FM spectrum region is selected to take in consideration only white noise. This spectral window is then considered as the

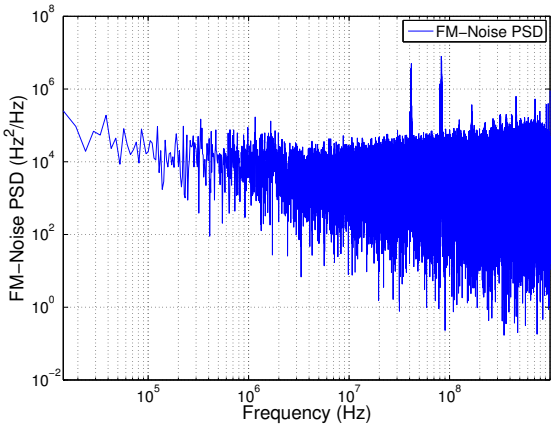

(a) Total FM-Noise spectrum

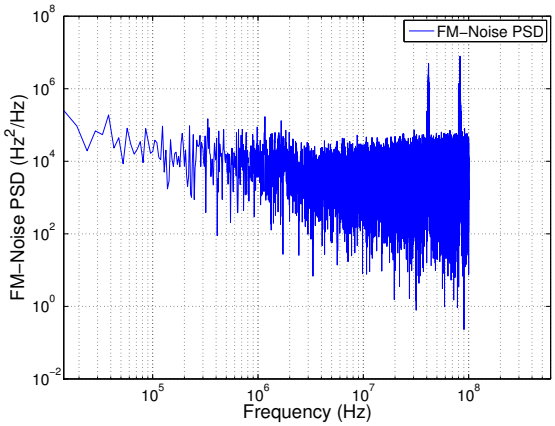

(b) Cut FM-Noise spectrum

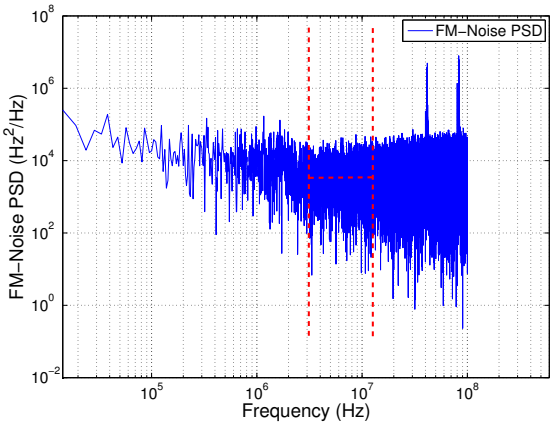

(c) Mean of FM-Noise spectrum

Figure 5.6 – Steps for mean of power spectral density of instantaneous frequency method.

complete PSD of instantaneous frequency and it can be approximated by its mean, (see Figure 5.6c). The laser linewidth estimate obtained by the method is thus calculated as:

$$\Delta_\nu = \pi \, mean(S_{F-Window}(f)), \tag{5.30}$$

Finally, from the relation between Δ_ν and Δ_{LW} , the linewidth estimate of the laser is:

$$\Delta_{LW} = \frac{\pi}{2} \, mean(S_{F-Window}(f)). \tag{5.31}$$

As a consequence of disregarding most of the spectrum, the method loses reliability. Then, the linewidth estimate can differ from the real value. A better alternative to overcome this inconvenient is presented in shortly.

5.1.2.4 Fit to power spectral density of instantaneous frequency

Under white phase noise assumption adopted in the previous method, the laser linewidth is given by:

$$\Delta_\nu = \pi \, S_F(f). \tag{5.32}$$

On the other hand, the flat region of the spectrum can be mathematically described as a constant that decreases with laser input power. Then, Eq. 5.32 is redefined as (KIKUCHI, 1989):

$$\Delta_\nu = \pi \frac{C}{P}. \tag{5.33}$$

From Eq. 5.33, it can be observed that when the output power P is increased, the linewidth decreases in proportion to P^{-1}. Then, it could be wrongly concluded that for an extremely high input power the laser presents an approximately zero linewidth. Interesting results in (KIKUCHI, 1989) show that in a high power state the linewidth can become constant (non-zero) for power increments and even it can rise again. The above makes sense because while the white noise component is power dependent, the low frequency noise ($1/f$ Noise) is not. Hence, regardless of the power, there is a residual laser linewidth originated by others sources of phase noise. Therefore, a better approximation of the FM spectrum for laser linewidth estimation is then given by:

$$S_F(f) = \Delta_\nu/\pi + \frac{k1}{f}, \tag{5.34}$$

where $k1$ is a measure of the $1/f$ noise influence. Parameter $k1$ can be obtained through a computational fitting function, from which Δ_ν can be estimated. In literature, different works consider several phase noise sources. For example, in (KOJIMA *et al.*, 2015), the FM spectrum is supposed to be the sum of three components:

$$S_F(f) = \Delta_\nu/\pi + \frac{k1}{f} + \frac{k2}{f^2}, \tag{5.35}$$

where the term $k2/f^2$ represents additional low frequency noise components. Once the FM spectrum has been mathematically defined as Eq. 5.34 or 5.35, the fit to power spectral density of instantaneous frequency method consists in carrying out a fitting process to find the most accurate values for k1 and k2 that describe the experimental FM spectrum, and subsequently extracting Δ_ν. Figure 5.7 shows the fit of the FM spectrum of an experimental signal. Finally, after Δ_ν calculation, the laser linewidth is derived from:

$$\Delta_{LW} = \Delta_\nu/2. \tag{5.36}$$

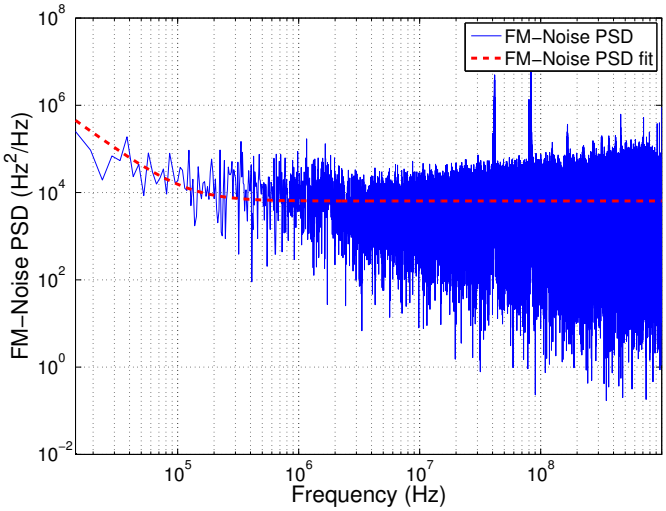

Figure 5.7 – FM-Noise spectrum fit.

5.2 EXPERIMENTAL EVALUATION OF LASER LINEWIDTH ESTIMATION TECHNIQUES

This section evaluates the performance of laser linewidth estimation techniques. The estimation process is carried out using the setup described in Section 5.1.1.3 (*delayed self-heterodyne with coherent receiver* method with $\Omega = 40$ MHz and 5 km of fiber delay) followed by offline digital signal processing. The experimental data is captured from four semiconductor lasers. Three of them are tested in normal operating conditions, while the other is tested under suboptimal operating conditions that generate three different types of phase perturbations, comprising six different sources. Table 5.1 shows the operating wavelength of the devices in the six evaluated conditions.

Table 5.1 – Available experimental data.

Laser	**1**	**2**	**3**	**4**	**5**	**6**
Wavelength	1550nm	1550nm	1550nm	1535nm	1550nm	1565nm

As it was presented in Section 5.1, in this work, the field detected by means of the *delayed self-heterodyne with coherent receiver* method is the base for laser linewidth estimation. From experimental traces, 670.000 samples are processed off-line using Matlab. As the phase perturbation experienced by the signal is the contribution of the frequency offset and the Wiener phase noise, a frequency recovery stage has to be applied before laser linewidth estimation. Frequency recovery is carried out through the *Mth-order power* method in frequency domain. Next, the three techniques for linewidth estimation described in Sections 5.1.2.2, 5.1.2.3 and 5.1.2.4 are applied to the recovered signal. Specifically, for *mean of power spectral density of instantaneous frequency* method, the PSD of

the instantaneous frequency is cut off at approximately 1 GHz, and the average is computed on the flatter region of the window. In the case of the *fit to power spectral density of instantaneous frequency* method, the fit operation is performed on the band limited by 0 Hz and 1 GHz. After these processes, linewidth estimates for the six lasers are obtained and presented in Table 5.2.

Table 5.2 – Linewidth estimates.

Laser	**Instant Frequency Variance**	**Mean of PSD of Instantaneous Frequency**	**Fit to PSD of Instantaneous Frequency**
1	28.26 kHz	33.77 kHz	33.54 kHz
2	55.63 kHz	274.91 kHz	234.59 kHz
3	33.35 kHz	136 kHz	116.76 kHz
4	28.69 kHz	30.09 kHz	30.82 kHz
5	4.1 MHz	69.89 kHz	44.54 kHz
6	1.67 MHz	43.75 kHz	37.76 kHz

Ideally, the laser linewidth values obtained through the three methods should be near, taking into account little imprecisions in the techniques. However, according to Table 5.2, in four out of the six cases (**lasers 2, 3, 5** and **6**) the three values differ in tens of kHz. Additionally, the other two cases, corresponding to **laser 1** and **laser 4**, present estimates of linewidth very similar, however, they vary in few kHz. This difference among the results gathered from different approaches limits the laser specification precision, and raises doubts about which method is the most accurate. Alternatively, we propose to compute the OSNR performance penalty from experimental traces, and later estimate an equivalent laser linewidth. To do this, impairments resulting from laser frequency fluctuations receive a special interest since, as it was shown in Chapter 4, the CFJ reduces the efficiency of the DSP algorithms.

5.2.1 System setup

As it was noted before, the available experimental data is the optical field reconstructed through the *delayed self-heterodyne with coherent receiver* method. This field has 4.000.000 samples and its phase corresponds to the phase perturbations that a received sequence of symbols would suffer if the laser tested in the setup was used in a coherent system. For experimental data application, traces with the first 670.000 samples are considered to reduce the processing time. The block diagram of the implemented simulator is shown in Figure 5.8.

To obtain the phase sequence, three procedures have to be applied to the experimental data. Initially, the *angle* operation recovers the signal phase. However, these phases can be altered coming from the limitation between $-\pi/4$ and $\pi/4$ presented by the function. Then, this process is corrected by an *unwrap* function. As the simulator works

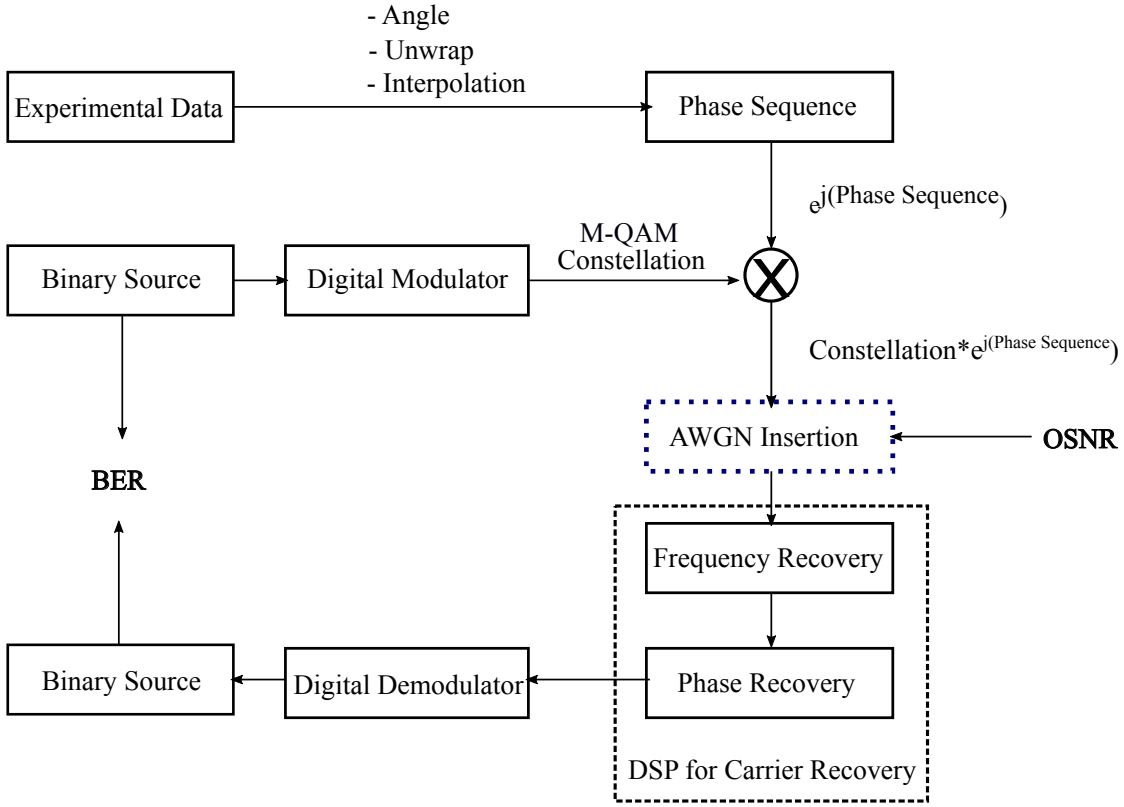

Figure 5.8 – Simulator block diagram.

with arbitrary symbol rate, the sequence of phases after unwrapping is interpolated in order to adapt its sample rate of 20 Gsps to the system symbol rate. That is, *interpolation* acts up-sampling or down-sampling depending on the required adaptation rate. At this point, the experimental sequence of phases is ready for being injected into a symbol constellation. The simulator supports the transmission of alphabets, 16-QAM and 64-QAM with a symbol rate of 32 GBd and 43 GBd, respectively. The digital modulator must produce enough quantity of symbols to multiply a sequence with 670.000 phases. Therefore, as the sampling rate of the experimental data is 20 GSps, then, for the systems at 32 GBd and 43 GBd, the phases traces are up-sampled by a factor of 1.6 and 2.15, respectively. Consequently, the 16-QAM modulator generates 1.072.000 symbols, while the 64-QAM modulator requires 1.440.500 symbols. The constellation generated at the modulator block is then multiplied by a signal $e^{j\zeta}$, where ζ denotes the sequence of experimental phases. After that, the signal is transmitted through an AWGN channel.

At reception transmission impairments are compensated by DSP. In an ideal context, in which the operating frequency of the laser is fixed in time, the *Mth-order power* algorithm described in Section 3.2.2 is efficient enough for frequency recovery. Nevertheless, practical implementations suffer the consequences of frequency fluctuations. The *Mth-order power* can be adjusted in such a way that it is possible to compensate for the additional penalties caused by fluctuations. For example, let us suppose the sinusoidal CFJ

shown in Figure 5.9a. The amplitude axis represents the different values of the frequency offset through the time. If *Mth-order power* is performed over all samples of the signal, only a single frequency offset is estimated and compensated. A considerable penalty in the algorithm performance arises as the *Mth-order power* technique does not realize frequency tracking. Accordingly, the average frequency offset given by the black line does not match the real jitter behavior drawn in blue. Accomplishing a perfect tracking of the blue curve

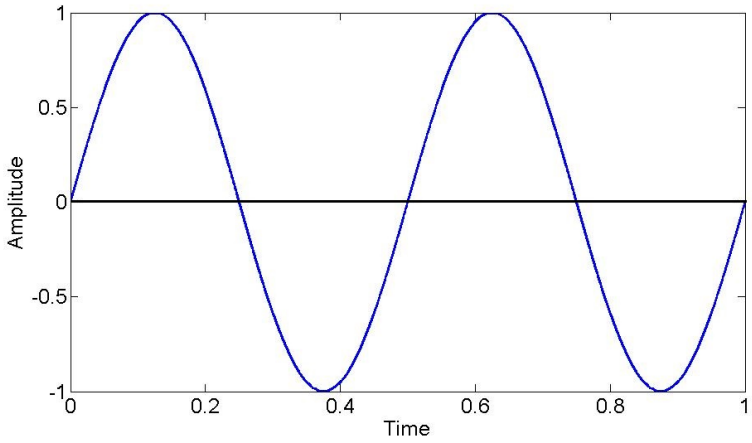

(a) Total jitter signal.

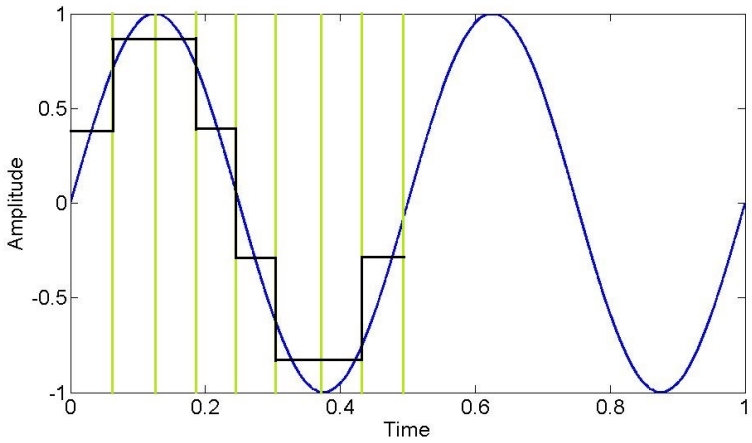

(b) Division by windows.

Figure 5.9 – Carrier frequency jitter treatment.

is computationally infeasible, nonetheless, a coarse version with reasonable resolution can be constructed. Figure 5.9 indicates that the CFJ treatment can be done not over all samples of the signal, but by means of windowing. In Figure 5.9b, the same sinusoidal CFJ is sliced in sections of fixed size. Then, *Mth-order power* algorithm computes an average frequency offset in each window. As the sections have a reduced number of samples, the average differs in a smaller amount from the extreme values. After this process, the black curve, although not being exactly the same as the blue one, is by far more accurate than the one in the previous scenario. The tracking resolution can be adapted by manipulating

the window size, that naturally depends on the CFJ intensity. The block diagram of the method applied in this work is shown in Figure 5.10. In the diagram, $r(k)$ stands for the signal at the DSP block input which already was contaminated with additive white noise and phase perturbations. When the algorithm starts, $r(k)$ is split into shorter windows denoted as $r_1(k)$, $r_2(k)$, $r_3(k)$,..., $r_n(k)$, being n the total number of windows. After that, each block goes through the stages of the classical *Mth-order power* algorithm to find the frequency offsets Δ_{f1}, Δ_{f2}, Δ_{f3},..., Δ_{fn}. Finally, the frequency offset-induced phase noises noted by $\Delta_{\phi 1}$, $\Delta_{\phi 2}$, $\Delta_{\phi 3}$,..., $\Delta_{\phi n}$ are compensated individually in each window. The blocks after frequency recovery are grouped again for obtaining $\hat{r}(k)$, that is forwarded to the phase recovery stage. In the diagram, T_{DSP} denotes the time period considered in the DSP algorithms that in this case matches with the symbol period T_s.

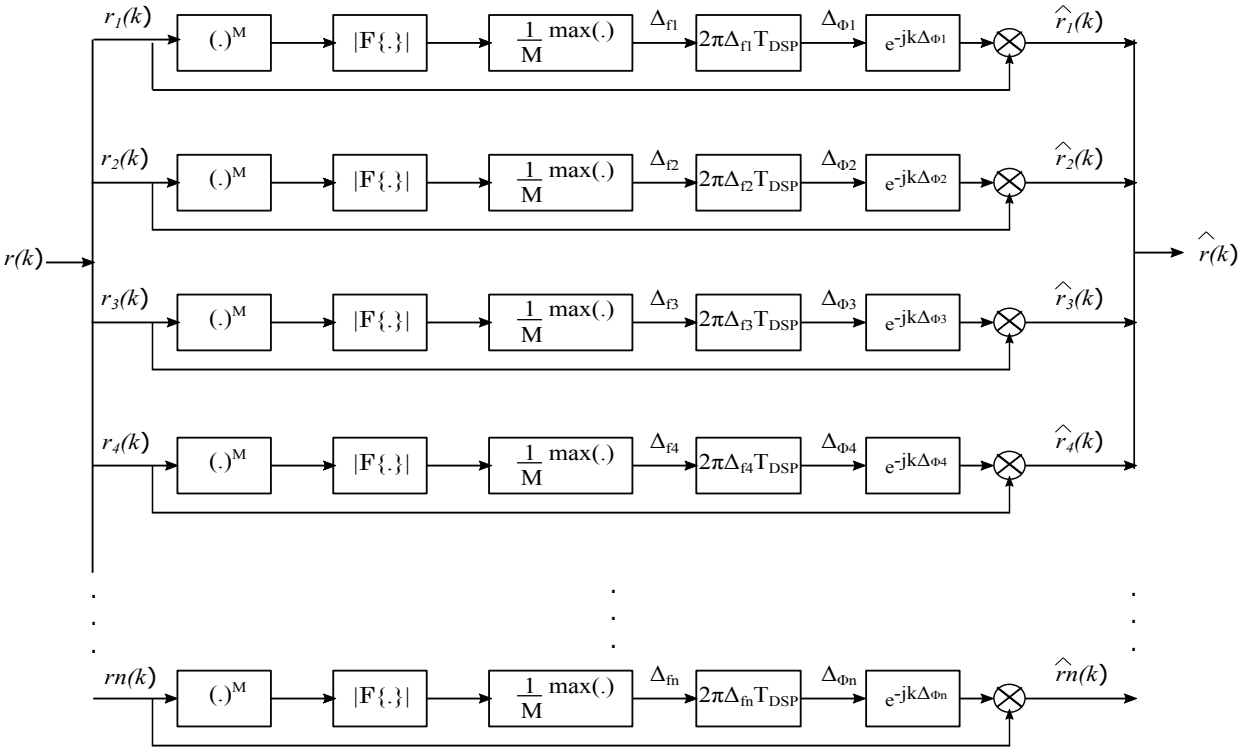

Figure 5.10 – Block diagram of the sliced Mth-oder power algorithm.

It should be noted that as the *Mth-order power* algorithm is based on the FFT, its accuracy is directly associated with the transform resolution. At the same time, the transform resolution depends on the quantity of samples in a block, so that the window size is a decisive parameter in the operation of the proposed algorithm. In other words, the technique performance depends on the equilibrium between an appropriated block size for a reasonable frequency tracking, and the number of samples needed for a good FFT resolution. Consequently, it is possible that, even after the *sliced Mth-order power* algorithm, a residual CFJ degrades the system performance.

After compensating the frequency offset and the CFJ, the Wiener phase noise

is estimated in the phase recovery stage. The simulator recovers the original phase by applying the conventional one-stage BSP algorithm to the signal. From Section 3.3.2, the configuration parameters of the algorithm are shown in Table 5.3. Finally, as the vector

Table 5.3 – Configuration of BPS for phase recovery.

BSP Configuration Parameters		
Test phases I	**Maximum phase**	**Summing window N_B**
40	$\pi/4$	82 for OSNR $<$ 16 dB 52 for 16 dB $<$ OSNR $\leq$ 18 dB 30 for OSNR $\geq$ 20 dB

of test phases is limited between $-\pi/4$ and $\pi/4$, the output of the BSP algorithm passes through an unwrapping stage.

After simulator description, the next sections consolidate the results concerning to the performance of the 16-QAM and 64-QAM coherent systems when experimental phase perturbations are applied.

5.2.2 Results for 16-QAM

To compute the OSNR performance penalty from experimental phase perturbations, the *sliced Mth-order power algorithm* was optimized for each laser. For 16-QAM system, the window size was optimized for a fixed OSNR equal to 19 dB. Different window sizes were evaluated and the block length achieving the lower BER was selected. Figure 5.11 presents the BER variation with respect to window size for the six experimental traces.

As it was expected, the curve that describes the BER variation against window size presents a different behavior for each tested laser. The curves corresponding to **lasers 1, 2, 3** and **4** experience a decreasing profile with the increase of window size values. On the contrary, the BER corresponding to **lasers 5** and **6** increase with long window sizes, reaching a BER of up to 9×10^{-2}. It should be noted, however, that for window sizes smaller than 10.000, the curves of **lasers 5** and **6** exhibit a decreasing behavior, an aspect that can be related to the low FFT resolution obtained with this number of samples in these cases. Table 5.4 summarizes the optimum window size for each laser.

Table 5.4 – Optimum window size for 16-QAM system.

Laser	**1**	**2**	**3**	**4**	**5**	**6**
Optimum WS	800.000	960.000	800.000	960.000	10.000	10.000

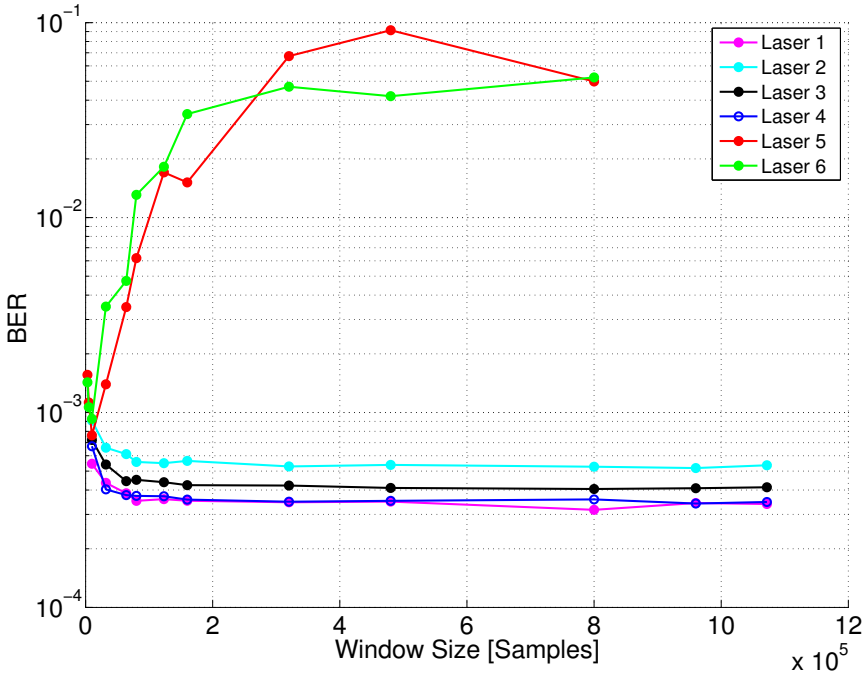

Figure 5.11 – Optimum window size for jitter correction in 16-QAM system.

From Table 5.4, it can be intuited that the six lasers present different CFJ intensities. Naturally, for higher frequency jitter variations, the window size needs to be smaller (**lasers 5** and **6**). Clearly, if the frequency offset varies in great proportions regarding the nominal value, the tracking comes more accurate for blocks with a smaller size. Otherwise, in a scenario with slow oscillations, in which the frequency offset is almost constant a wide window is enough to track the signal (**lasers 1**, **2**, **3** and **4**). After window size optimization, the *sliced Mth-order power* algorithm is configured each time depending on the experimental trace to use. It should be clarified that window size optimization does not ensure a total elimination of the CFJ effects, because even with the more appropriate block size, frequency tracking is not perfect, giving rise to residual frequency jitter.

To assess the 16-QAM format performance, the OSNR was evaluated in the interval between 16 dB and 23 dB, in steps of 0.5 dB. For each OSNR value, the simulation is repeated three times in order to average the BER and to smoothen the curve. Figure 5.12 shows the performance curves for the six experimental traces. In the figure, the black solid curve corresponds to the theoretical performance of a 16-QAM coherent system at 32 GBd operating in a single polarization mode. The remaining curves correspond to the experimental traces associated with the lasers. In addition, the horizontal dashed black line indicates the FEC limit at BER $= 1 \times 10^{-3}$, and the vertical dashed green line points to the theoretical OSNR required for this FEC limit (17.75 dB). Table 5.5 collects the OSNR values required for the curves to attain a BER $= 1 \times 10^{-3}$ as well as the OSNR

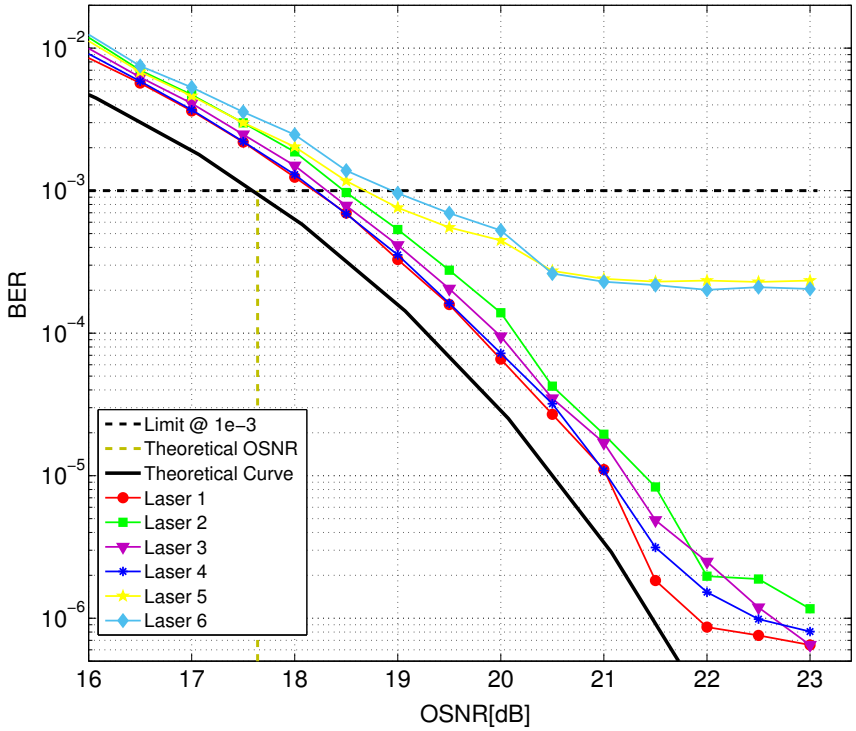

Figure 5.12 – Performance of the 16-QAM coherent optical system.

penalty at this point.

Table 5.5 – OSNR Penalties for 16-QAM coherent optical system.

Laser	**OSNR at BER = 1e-3 [dB]**	**OSNR Penalty [dB] (Theoretical OSNR = 17.75 dB)**
1	18.22	0.47
2	18.48	0.73
3	18.35	0.60
4	18.25	0.50
5	18.66	0.92
6	18.97	1.22

According to Figure 5.12 and Table 5.5, the higher performance is reached by the **lasers 1** and **4**, which present approximately the same curve. **Lasers 2** and **3** suffer a non-critical performance degradation in comparison with the previous ones, while **lasers 5** and **6** evidence a poor performance in the whole investigated OSNR region. Taking into consideration that all of the six test systems are subject to identical channel conditions, and that they use the same DSP block, the difference among the performances curves is related to the phase perturbations applied to the symbols. As previously emphasized, the phase perturbations extracted from the experimental data are a contribution of the Wiener phase noise caused by the laser linewidth, and CFJ due to the operating frequency fluctuations. In addition, starting from the fact that the device under tests (DUTs) used

for capturing the experimental measures correspond to current commercial lasers, a small linewidth is assumed. Therefore, it is valid to suppose that the Wiener phase noise associated with each laser is not high enough to be considerably harmful to a 16-QAM system which employs an efficient phase recovery algorithm. Then, one can conclude that the OSNR penalty presented by the system appears because of CFJ. After this assumption, and observing Table 5.4 and Table 5.5, it can be concluded that a high CFJ variation implies a considerable performance degradation, as it is the case of **lasers 5** and **6**. Again, here as in Chapter 4, the results show how the intensity of the laser frequency fluctuations affects negatively the DSP algorithms performance.

At this point, the OSNR penalty computed for the curves allows finding the equivalent linewidths of the lasers seen by the DSP algorithms in a 16-QAM system. For this, the simulator in Figure 5.8 is used to get the performance of the system against simulated Wiener phase noise. During the tests, 15 values of linewidth (considering transmitted and local oscillator lasers, Δ_ν) are selected between 0 Hz and 3.000 kHz. The symbol period is configured in 31.25 μs that corresponds to a symbol rate of 32 GBd. Figure 5.13 shows the 16-QAM system performance for 15 values of $\Delta_\nu Ts$.

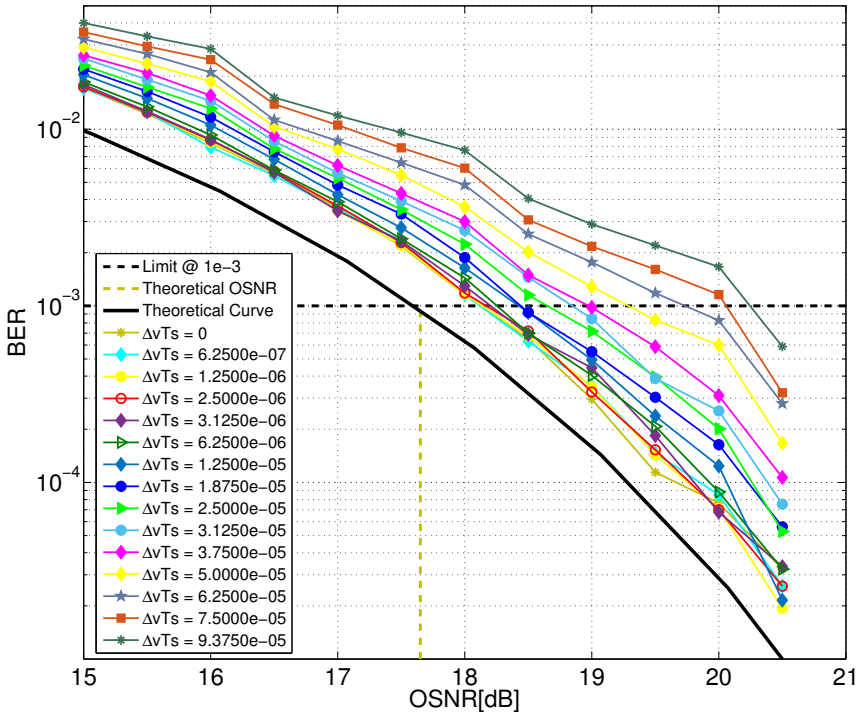

Figure 5.13 – Simulated performance of 16-QAM coherent optical system.

Analyzing the graph, one can note how a higher $\Delta_\nu Ts$ product causes a more prominent degradation in the system performance. This behavior is supported by Eq. 3.14,

in which it is observed that the variance of the phase noise increments from one symbol to other is directly proportional to $\Delta_\nu Ts$. On the other hand, it is worth mentioning that even for $\Delta_\nu Ts = 0$, the performance curve presents a penalty with respect to the theoretical one as consequence of the differential encoding. The OSNR penalty for simulated phase noise regarding the theoretical performance is calculated for every curve in the FEC limit at BER $= 1 \times 10^{-3}$. The results are summarized in Table 5.6.

Table 5.6 – OSNR Penalty for 16-QAM with simulated phase noise.

$\Delta_\nu Ts$	Δ_ν **[kHz]**	**OSNR at BER = 1e-3 [dB]**	**Penalty at BER = 1e-3 [dB]**
0	0	18.15	0.40
6.25e-07	20	18.15	0.41
1.25e-06	40	18.17	0.42
2.50e-06	80	18.20	0.45
3.12e-06	100	18.25	0.50
6.25e-06	200	18.30	0.55
1.25e-05	400	18.44	0.69
1.87e-05	600	18.45	0.70
2.50e-05	800	18.68	0.93
3.12e-05	1000	18.87	1.13
3.75e-05	1200	18.98	1.23
5.00e-05	1600	19.32	1.57
6.25e-05	2000	19.76	2.01
7.50e-05	2400	20.10	2.35
9.37e-05	3000	20.31	2.56

Once $\Delta_\nu Ts$ values and the corresponding OSNR penalties are available, a useful curve is constructed to obtain the laser linewidth from a DSP perspective. Figure 5.14 relates the OSNR penalty in dB with the $\Delta_\nu Ts$ product. The blue curve relates the values registered in the first and last column of Table 5.6. The fitted red curve correlates the parameters in a continuous interval defined between 6×10^{-7} and 1.3×10^{-4} for $\Delta_\nu Ts$ and 0.3995 dB and 2.5648 dB for OSNR penalty. Although the red curve offers a valid relation between parameters, its increasing behavior is not perceptible until $\Delta_\nu Ts = 6 \times 10^{-6}$. As consequence, it can be possible that the technique looses resolution for small Δ_ν values. To estimate the linewidth of the lasers using this tool the procedure is as follows: for each tested laser, the OSNR penalty in Table 5.5 is positioned in the vertical axis. After that, this point is projected on the red curve to finally find the corresponding $\Delta_\nu Ts$ in the horizontal axis. Once $\Delta_\nu Ts$ is known, the laser linewidth is given by:

$$\Delta_{Lw'} = \frac{\Delta_\nu Ts}{2 \times Ts} \tag{5.37}$$

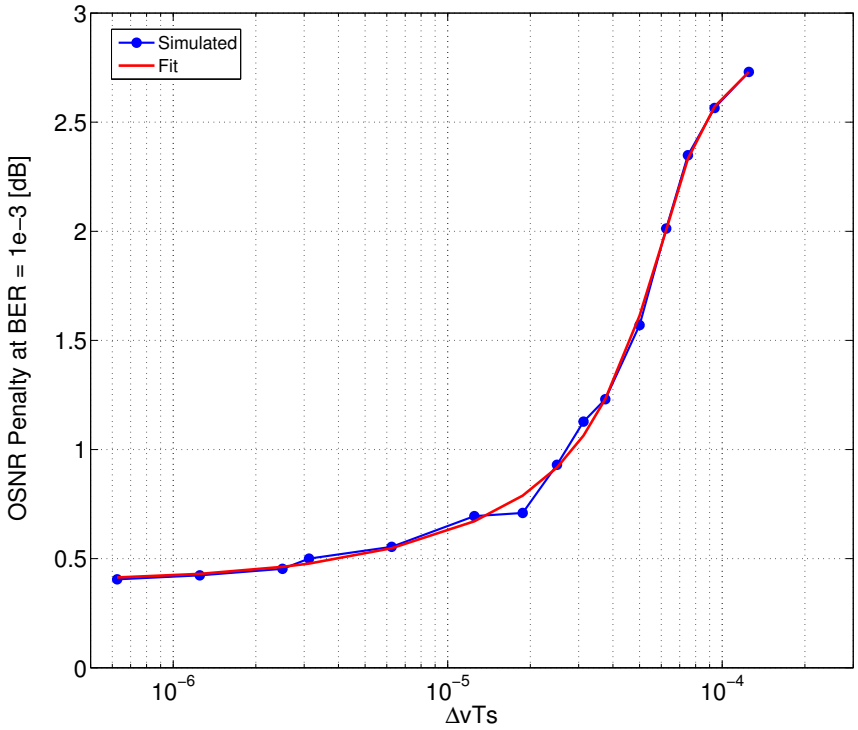

Figure 5.14 – Simulated curve for Δ_νTs vs OSNR penalty for 16-QAM coherent optical system.

where $\Delta_{Lw'}$ can be understood as the equivalent linewidth of the laser from a systemic point of view. Table 5.7 gathers the lasers linewidths obtained by means of the current estimation methods and through the DSP performance.

Table 5.7 – Linewidth estimates by four methods.

Laser	**Variance Inst. Freq.**	**Mean of PSD of Inst. Freq.**	**Fit to PSD of Inst. Freq.**	**Linewidth by performance**
1	28.26 kHz	33.77 kHz	33.54 kHz	50.7 kHz
2	55.63 kHz	274.91 kHz	234.59 kHz	253 kHz
3	33.35 kHz	136 kHz	116.76 kHz	145.5 kHz
4	28.69 kHz	30.09 kHz	30.82 kHz	66.1 kHz
5	4.1 MHz	69.89 kHz	44.54 kHz	431 kHz
6	1.67 MHz	43.75 kHz	37.76 kHz	583 kHz

Comparing the results along the rows, first, it is noted that the linewidth calculated by performance differs considerably from the estimate by instantaneous frequency variance in all cases. Secondly, for **lasers 2** and **3**, the systemic linewidth is very close to the ones found through methods *mean of PSD of instantaneous frequency* and *fit to PSD of instantaneous frequency*. In the case of **lasers 1** and **4**, the calculus of the linewidth is limited as consequence of the low resolution presented by the fitted curve for

small Δ_ν values. However, for both lasers, the systematic linewidth also tends to match the linewidths obtained by the two spectral methods. On the other hand, the equivalent linewidths corresponding to **lasers 5** and **6** differ by far from the results given by the others three estimation methods. To interpret the results, it is interesting to note that linewidth estimation by means of current techniques was carried out before CFJ compensation. In addition, it is already known that the CFJ is a low frequency effect, therefore, as spectral methods manipulate high frequencies, it is expected that they are not able to detect the jitter perturbations. Unlike spectral methods, instantaneous frequency variance is a time domain technique. Thus, calculated phase increments are a contribution not only from the Wiener phase noise that has to be measured but also from other phase noise sources and CFJ. Therefore, naturally, the accuracy of the method is negatively influenced by a high intensity of laser imperfections. The loss of reliability of the method is observed in **lasers 5** and **6**, in which, due to the high CFJ, the estimated linewidths through instantaneous frequency variance are in the range of megahertz, while the other three methods estimate linewidths in some hundreds of kilohertz. Moreover, in low CFJ scenarios, as in **lasers 2** and **3**, the method estimates are also considerably different from the equivalent linewidths found by means of system performance. That is, the method resolution is limited for both low and high CFJ because of the possible presence of other phase noise sources. In consequence, it can be concluded that, among the three evaluated estimators the most suitable are the *mean of PSD of instantaneous frequency* and *fit to PSD of instantaneous frequency* methods. Nevertheless, the above assumption loses reliability in high CFJ contexts as in **lasers 5** and **6**, in which both spectral methods designate a smaller linewidth with regard to the systematic value. In this way, it is valid to affirm that the methods commonly used by manufacturers to characterize the lasers are not accurate enough as they do not take in consideration the effect of the CFJ on the system performance. Customers are interested in obtaining from manufacturers the value of the laser linewidth associated with the performance that their systems would present when the laser is used. Therefore, the strategy here proposed is a convenient option as it characterizes the laser in both high and low CFJ context when the jitter is compensated through a frequency recovery algorithm. While it is true that laser characterization from a performance perspective presents notable advantages against the other options, at the same time this method demands a greater complexity. Obtaining the systematic linewidth as previously done required a complex simulator operation. Then, the weakness of our approach gives rise to a new question. Is it possible to predict the performance of a 16-QAM system at 32 GBd using a certain laser using low-complexity computations? This issue is going to be evaluated in future sections.

5.2.3 Results for 64-QAM

Nowadays, the exponential growth of the data traffic challenges the telecommunications infrastructure. Therefore, to keep up with the current requirements, spectrally efficient systems are required. The 64-QAM modulation format appears as an alternative to implement systems able to transmit higher volumes of information than its predecessors using the same spectral resources. On the other hand, increasing the constellation size makes the system more susceptible to phase perturbations. Thus, both the Wiener phase noise and the CFJ require special attention.

In the 64-QAM case, the window size was optimized for an OSNR of 26 dB. The window size was varied from 3.000 to 1.440.500 samples with non-uniform spacing. The results are shown in Figure 5.15. The six curves in Figure 5.15 exhibit the expected

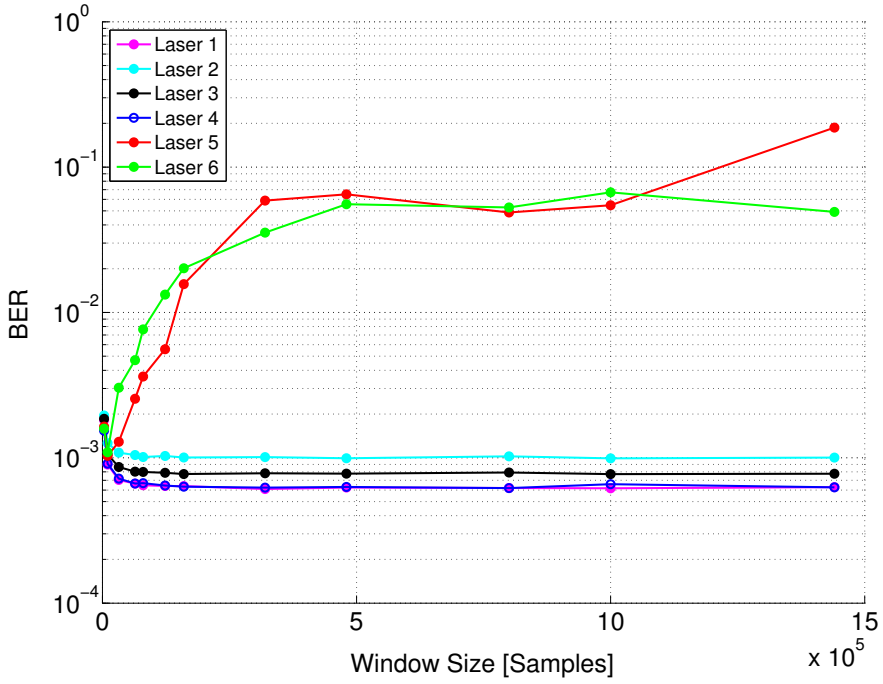

Figure 5.15 – Optimum window size for jitter correction in 64-QAM system.

behavior based on previous results. Again, the BER for **lasers 1, 2, 3** and **4** decreases with an increase in the window size. However, because of the low CFJ in these lasers, all BER values are similarly small, varying between 6×10^{-4} and 2×10^{-3}. In a different way, the BER achieved by the system when **lasers 5** and **6** are used increases for higher window sizes, varying from approximately 1×10^{-3} to 2×10^{-1}. The optimum window size for each laser is shown in Table 5.8.

From current results, a strong consistency with the previous section is observed. In a severe CFJ context as in the case of **lasers 5** and **6**, the best frequency offset tracking is achieved slicing the jitter signal in small windows of 10.000 samples. Meanwhile, for

Table 5.8 – Optimum window size for 64-QAM system.

Laser	**1**	**2**	**3**	**4**	**5**	**6**
Optimum WS	320.000	1.000.000	1.000.000	800.000	10.000	10.000

slow frequency offset fluctuations presented by **lasers 1, 2, 3** and **4**, a large window is able to go along with the signal, favoring at the same time the resolution of the FFT. Now, the simulations are carried out for every test laser and the proposed frequency recovery algorithm for CFJ compensation is configured according to Table 5.8.

The evaluated OSNR range is defined between 19 dB and 29 dB in steps of 0.5 dB. In a similar way, in order to smoothen the curves, three rounds are executed for each OSNR value. At the receiver, the DSP block keeps unaltered with exception of the window size in the *sliced Mth-order power* algorithm. The window size is configured depending on the laser to test in a specific simulation. Figure 5.16 compares the performance obtained in the 64-QAM system at 43 GBd for the six lasers. The reference points for performance

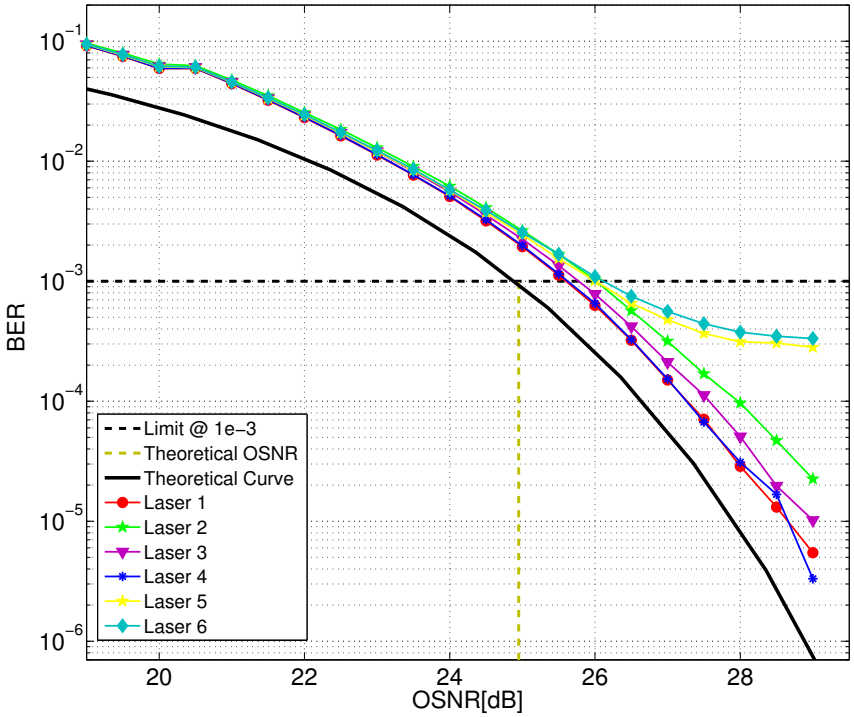

Figure 5.16 – Performance of the 64-QAM coherent optical system.

evaluation are again the FEC limit at BER $= 1 \times 10^{-3}$, the performance theoretical curve and the theoretical OSNR for this BER (25.0332 dB). Thus, it is observed from BER vs OSNR curves that the best-behaved lasers are **1** and **4** as result of the mild frequency fluctuations and/or of the low residual jitter after DSP compensation. **Laser 3** either presents a considerable performance degradation unlike **lasers 2, 5** and **6** that generate

a OSNR penalty around of 1 dB. Table 5.9 gathers the OSNR penalty computed in each case.

Table 5.9 – OSNR penalties for 64-QAM coherent optical system.

Laser	**OSNR at BER = 1e-3 [dB]**	**OSNR Penalty [dB] (Theoretical OSNR = 25.03 dB)**
1	25.63	0.59
2	26.03	0.99
3	25.81	0.78
4	25.66	0.62
5	26.07	1.04
6	26.15	1.11

The performance curves of the 64-QAM system confirm that the OSNR penalty increases for high levels of frequency offset fluctuations. For an intense CFJ, as in **lasers 5** and **6**, even after jitter compensation in the frequency recovery stage the received signal still experiences the negative effects of the residual jitter and/or of the low FFT resolution. Once the OSNR penalty generated for the six test laser are available, the systemic linewidth associated with this performance degradation is determined. For that, in the same way, the simulator deployed in Figure 5.8 evaluates the performance of the 64-QAM system against simulated Wiener phase noise. During the tests, 13 values of total linewidth (transmitted and local oscillator lasers, Δ_ν) are selected between 0 Hz and 2.000 kHz. For a symbol rate of 43 GBd, the symbol period is configured in 23.25 μs. Figure 5.17 shows the 64-QAM system performance for the different values of $\Delta_\nu Ts$.

The Wiener phase noise intensity is directly proportional to $\Delta_\nu Ts$, consequently, the system presents a higher performance degradation as the product increments. Based on these curves, a direct relation between Δ_ν and OSNR penalty in a 64-QAM system at 43 GBd can be obtained. Table 5.10 shows these OSNR penalties.

Finally, Figure 5.18 relates the OSNR penalty at BER = 1×10^{-3} with the $\Delta_\nu Ts$ product. The red fit covers the region delimited roughly by 4.5×10^{-7} and 5×10^{-5} in the $\Delta_\nu Ts$ axis. For this interval, the OSNR penalties vary from 0.5 dB to 5 dB. As the 64-QAM constellation is more susceptible to phase noise, the resolution of the curve is higher for small values of laser linewidth than in the case of Figure 5.14 for the 16-QAM system.

To characterize a device, from the OSNR penalty generated by the specific laser, the corresponding value of $\Delta_\nu Ts$ is extracted using the red curve. Later, Eq. 5.37 provides the equivalent linewidth seen from a DSP performance perspective. Table 5.11 compares the estimates of the lasers linewidths computed through the four methods in

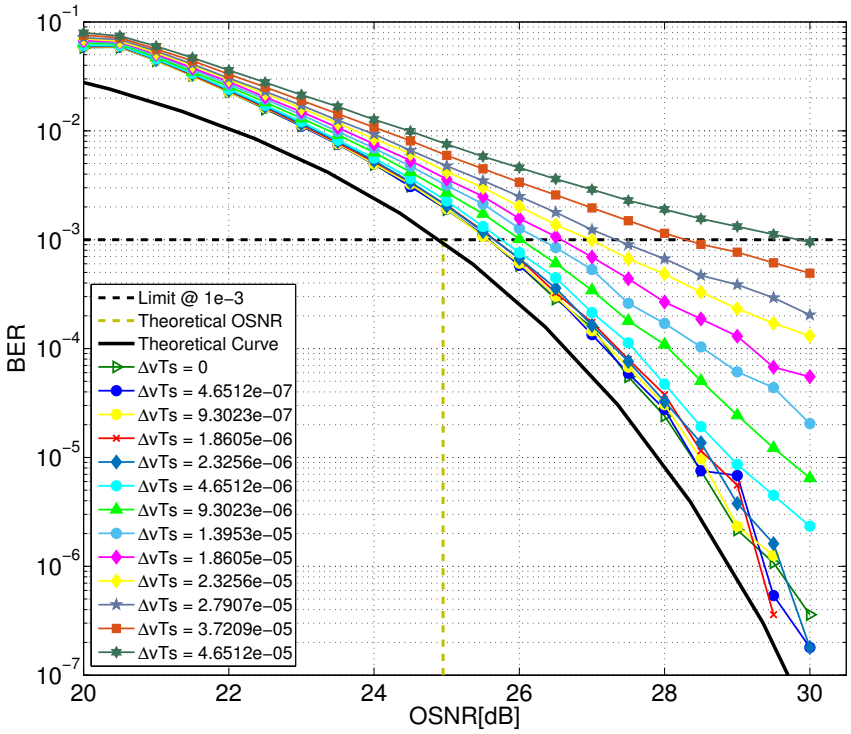

Figure 5.17 – Simulated performance of 64-QAM coherent optical system.

Table 5.10 – OSNR penalty for 64-QAM with simulated phase noise.

$\Delta_\nu Ts$	Δ_ν **[kHz]**	**OSNR at BER = 1e-3 [dB]**	**Penalty at BER = 1e-3 [dB]**
0	0	25.60	0.56
4.65e-07	20	25.61	0.57
9.30e-07	40	25.58	0.55
1.86e-06	80	25.70	0.66
2.32e-06	100	25.69	0.65
4.65e-06	200	25.79	0.76
9.30e-06	400	26.02	0.99
1.39e-05	600	26.32	1.29
1.86e-05	800	26.59	1.56
2.32e-05	1000	26.99	1.95
2.79e-05	1200	27.35	2.32
3.72e-05	1600	28.31	3.28
4.65e-05	2000	29.86	4.83

question, being one of them the approach suggested in this work.

The systemic linewidth computed for **lasers 1, 2, 3** and **4** stay in the same band as the linewidth found by means of the two spectral methods. It supports the fact that, in a low jitter scenario, analyzing the PSD of the instantaneous frequency is enough for laser characterization even when both of them do not take in consideration the CFJ ef-

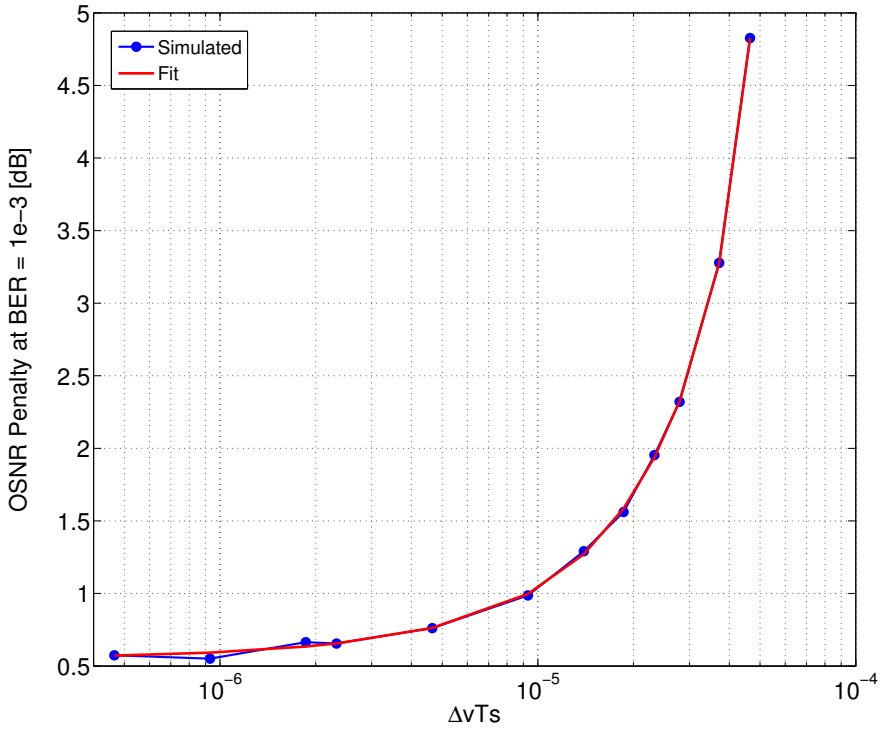

Figure 5.18 – Simulated curve for Δ_νTs vs OSNR penalty for 64-QAM coherent optical system.

Table 5.11 – Linewidth estimates by four methods with 64-QAM.

Laser	**Variance Inst. Freq.**	**Mean of PSD of Inst. Freq.**	**Fit to PSD of Inst. Freq.**	**Linewidth by performance**
1	28.26 kHz	33.77 kHz	33.54 kHz	21.72 kHz
2	55.63 kHz	274.91 kHz	234.59 kHz	199 kHz
3	33.35 kHz	136 kHz	116.76 kHz	108.26 kHz
4	28.69 kHz	30.09 kHz	30.82 kHz	36.9 kHz
5	4.1 MHz	69.89 kHz	44.54 kHz	215 kHz
6	1.67 MHz	43.75 kHz	37.76 kHz	243 kHz

fects. Nevertheless, when the device experiences a high CFJ level, the spectral approaches are not recommended since they neglect the contribution of the jitter to the phase perturbations. As result of the above statement, the equivalent linewidth of **lasers 5** and **6** differs by far from the other estimates, becoming the most realistic laser specification.

5.3 COMBINING LASER LINEWIDTH AND CFJ TO PREDICT THE SYSTEM PERFORMANCE

The phase traces extracted from experimental data bring the phase perturbation of Wiener phase noise and CFJ. Consequently, after system performance evaluation,

we try to relate the OSNR penalty with the laser imperfections intensity, with low complexity signal processing. Bringing up the fact that the OSNR penalty in the system is raised by a large laser linewidth and CFJ, in this work, we propose a convenient strategy for performance forecasting. The idea is to know beforehand the performance of a coherent optical system at a determined symbol rate when a specific laser is used as the transmitter laser and local oscillator laser. The starting point to develop a performance forecasting tool consists in understanding that the intensity of the frequency fluctuations can be quantified by the difference between two frequency offsets computed in adjacent windows (Δ_f Jump). In other words, logically, the CFJ is more severe when the jumps in frequency from one window to the next are higher. Figure 5.19 shows again the sinusoidal CFJ sliced in smaller windows. According to the previous analysis, the management of the jumps marked in red gives key information about the jitter variation, then, the first step is to capture these jumps from the experimental data.

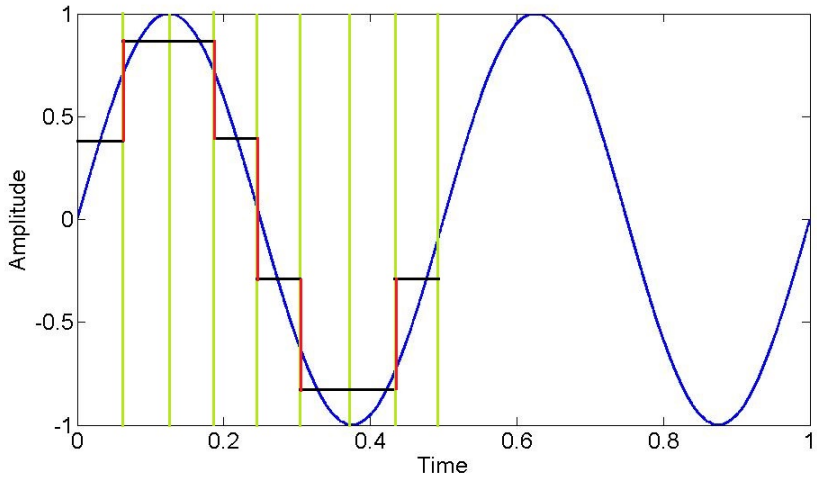

Figure 5.19 – Jumps of the sinusoidal carrier frequency jitter.

Each original experimental data is cut off at 670.000 and the resulting sequence is sent through the block of frequency offset estimation shown in Figure 5.20. The window size is configured to 10.000 samples (smaller window in Table 5.4). Then, after this process, 67 different values of the frequency offset are obtained and stored. Subtracting the values in adjacent windows results in 66 jumps, which describes the jitter behavior. The stored jumps are given in units of Hz/$(10.000 \times Ts)$.

After capturing the frequency offset jumps for all lasers, the next step to follow is to estimate the jitter probability distribution. Thus, using the Matlab function *histogram* the relative frequency of the jumps is computed. Figures 5.21 and 5.22 show the histogram for **laser 2** and **6**, respectively.

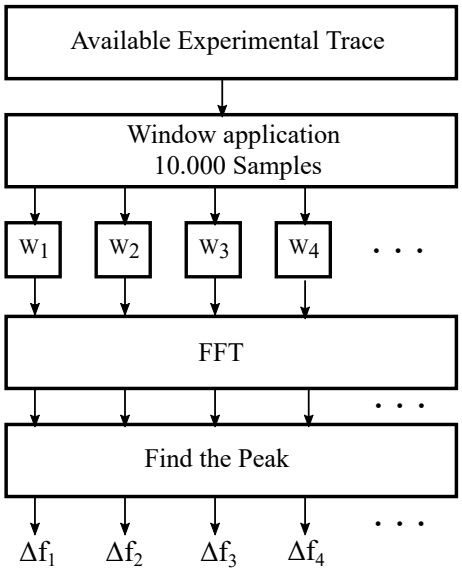

Figure 5.20 – Frequency offset estimation.

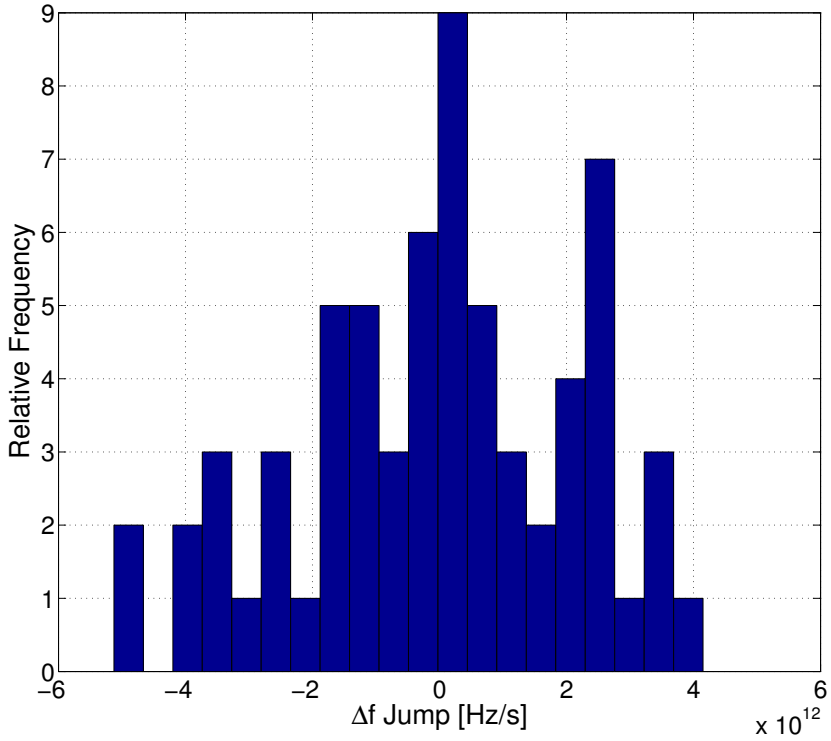

Figure 5.21 – Probability distribution of the jumps for laser 2.

From Figure 5.21, the lager jump for **laser 2** is found in approximately −5 THz/s with a relative frequency of 2/66. On the other hand, according to Figure 5.22, in the case of **laser 6**, the histogram presents one jump in 230 THz/s and another one in 540 THz/s. In general, as it was expected, within a low CFJ scenario (**laser 2**), the difference between frequency offsets from one window to the next is by far smaller when

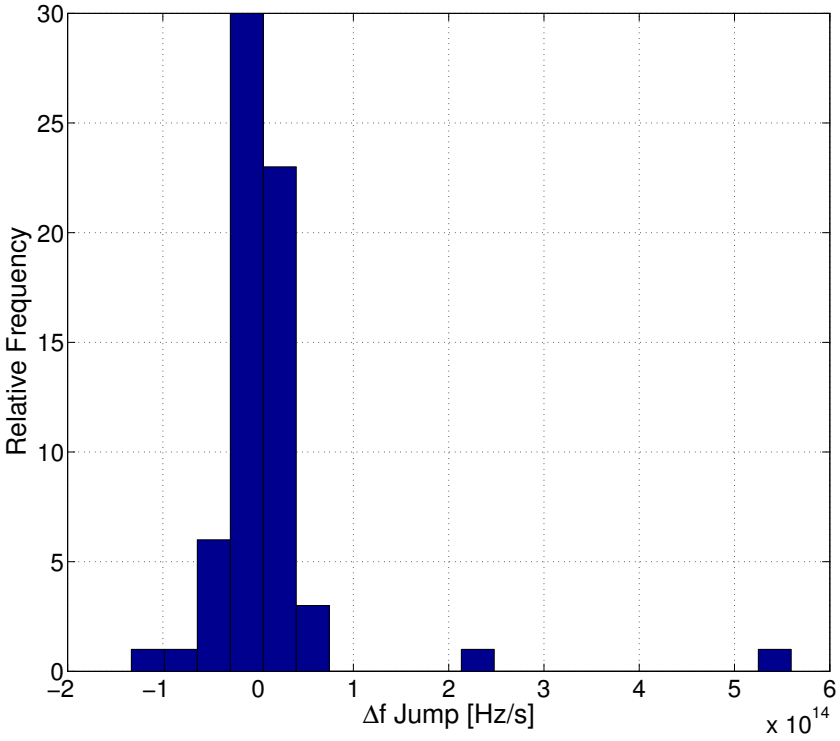

Figure 5.22 – Probability distribution of the jumps for laser 6.

compared with a context of high jitter (**laser 6**). These results support the hypothesis that the jitter characterization can be realized by means of the transitions experienced by the frequency offset through samples.

High-order modulations formats are more vulnerable to phase perturbations. Therefore, the OSNR penalty is caused not mostly by the CFJ, but also by the laser linewidth. Consequently, if the performance degradation that experiences a M-QAM coherent system is the result of the coupling of these perturbations, they should be enough to predict the impact of laser imperfections on system performance. Previously, the CFJ intensity was evaluated through the average jump of the frequency offset. On the other hand, our performance forecast tool requires the most reliable linewidth estimate obtained by the three estimation methods. As mentioned before, none of the strategies applied on the experimental traces matched the equivalent linewidth systematically estimated. However, the spectral methods presented a high accuracy in low CFJ scenarios. Therefore, the *mean of PSD of the instantaneous frequency* is selected due to its lower complexity. Table 5.12 presents the average jump of the frequency offset and the linewidth estimate for 29 experimental measurements obtained using three lasers in normal operating conditions, and a fourth laser in different operating conditions to simulate 29 DUTs in total.

Table 5.12 – Laser characterization by linewidth estimate and CFJ average jump.

Laser	**Average Jump [Hz/s]**	**Estimated LW Mean to PSD of Inst. Freq. [kHz]**	**Laser**	**Average Jump [Hz/s]**	**Estimated LW Mean to PSD of Inst. Freq. [kHz]**
1	3.18e+11	33.8	**16**	6.21e+13	87.1
2	1.73e+12	274.9	**17**	6.88e+13	89.8
3	8.58e+11	136	**18**	4.93e+13	50.2
4	3.55e+11	31.9	**19**	5.65e+13	7782.9
5	3.92e+11	30.1	**20**	4.92e+13	472.3
6	3.69e+11	31.2	**21**	7.21e+13	1335.5
7	3.96e+11	31.1	**22**	2.29e+13	740.5
8	3.77e+11	30.2	**23**	1.08e+13	821.7
9	2.80e+13	49.5	**24**	3.69e+13	929.5
10	2.88e+13	69.9	**25**	7.77e+12	570
11	2.84e+13	58	**26**	1.87e+13	642.8
12	2.82e+13	60.8	**27**	3.80e+13	662.9
13	2.75e+13	62.7	**28**	5.99e+13	903.7
14	4.99e+13	54.3	**29**	3.15e+12	267.1
15	3.38e+13	43.8			

5.3.1 Results for 16-QAM

Table 5.12 characterizes 29 devices in terms of linewidth and CFJ. Again, we can question if the measure of the laser imperfections from experimental phase perturbation traces allows forecasting the performance of a 16-QAM coherent system at 32 GBd when the laser is used in transmitter and reception. For that, the OSNR penalty for each of the 29 lasers is calculated by means of the simulator of Section 5.2.1. Table 5.13 present these OSNR penalties.

Table 5.13 – OSNR penalties for 16-QAM coherent system

Laser	**OSNR Penalty [dB]**	**Laser**	**OSNR Penalty [dB]**
1	0.48	**16**	2.39
2	0.73	**17**	2.35
3	0.60	**18**	1.61
4	0.49	**19**	-
5	0.50	**20**	1.85
6	0.47	**21**	3.28
7	0.47	**22**	1.38
8	0.52	**23**	1.17
9	0.85	**24**	1.98
10	0.92	**25**	1.02
11	0.94	**26**	1.29
12	0.92	**27**	1.50
13	0.94	**28**	2.42
14	2.02	**29**	0.64
15	1.22		

Once all DUTs are characterized by their linewidth estimate, frequency offset average jump and OSNR penalty, Figure 5.23 shows a 3D curve that allows observing the relation between both phase perturbations sources and the system OSNR penalty. The horizontal axis corresponds to laser linewidth estimate and vertical axis to average jumps. The third dimension is defined by the circle fill color which depends on the OSNR penalty as indicated in the color bar.

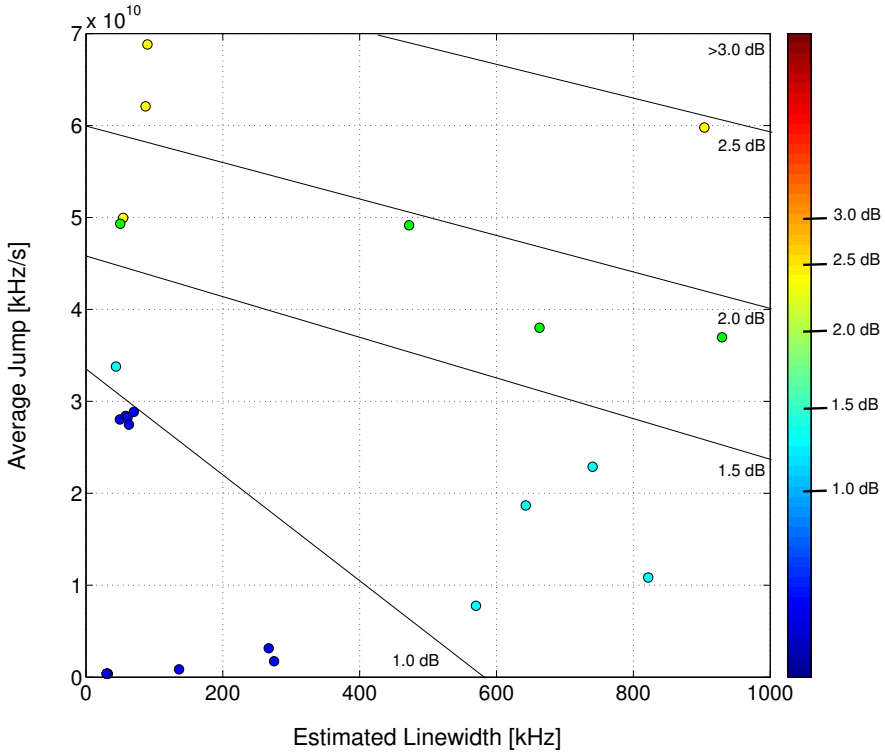

Figure 5.23 – Relation between laser linewidth estimate, average jump and OSNR penalty for 16-QAM coherent optical system.

Available data produce 29 isolated points instead of forming a surface. Consequently, it is not possible to generate a color map mesh. However, the 3D graph allows recognizing the pattern followed by the color of the circles. Note that for a laser presenting a low average jump (up to 3×10^{10} kHz/s) together with a low linewidth (up to 300 kHz), the system OSNR penalty remains smaller than 1 dB (shades of blue). Otherwise, when one of the axes increases, the OSNR penalty raises progressively to approximately 1.5 dB (shades of cyan). Naturally, in the worst case, when both parameters rise at the same time, the degradation becomes critical reaching penalties of 2 dB to 2.5 dB (shades of green and yellow). From these observations, Figure 5.23 also confirmed that exist a relation of direct proportionality between the OSNR penalty and the laser imperfections intensity. Therefore, the 3D map is able to forecast the performance of a semiconductor laser just from a phase perturbation trace without simulation procedures. The forecasting

tool is based on the identification of regions delimited by thresholds of OSNR penalty. That is, once the experimental data is available, the *mean of PSD of the instantaneous frequency* is applied to estimate the laser linewidth. At the same time, the jump collection is carried out by the process in Figure 5.20 to later computing the average jump. Finally, these both values are positioned in the horizontal and vertical axis of the map, respectively. The region of the resulting intersection point gives a reasonable estimate of the OSNR penalty that the 16-QAM coherent system would present if the evaluated laser was used as transmitter laser and local oscillator laser.

5.3.2 Results for 64-QAM

For the 64-QAM coherent system, the same procedure as previous section is performed. Table 5.14 presents the OSNR penalties for the 29 DUTs.

Table 5.14 – OSNR penalties for 64-QAM coherent system

Laser	**OSNR Penalty [dB]**	**Laser**	**OSNR Penalty [dB]**
1	0.59	**16**	1.72
2	0.99	**17**	2.12
3	0.78	**18**	1.36
4	0.66	**19**	-
5	0.63	**20**	2.25
6	0.59	**21**	-
7	0.61	**22**	1.97
8	0.59	**23**	1.89
9	0.96	**24**	3.07
10	1.04	**25**	1.42
11	0.98	**26**	1.86
12	0.96	**27**	1.92
13	0.95	**28**	3.83
14	1.29	**29**	0.90
15	1.11		

Figure 5.24 relates the laser linewidth estimates, frequency offset average jumps and OSNR penalties for the 29 DUTs. The color of the circles follows the expected behavior. Again, the OSNR penalty increase with a increase of the laser linewidth, average jump or both. However, as 64-QAM system is more susceptible to phase perturbation, the OSNR penalty is higher in comparison with 16-QAM system for the same laser imperfections intensity. For instance, lasers with a linewidth between 600 kHz and 900 kHz, and an average jump of 1×10^{10} kHz/s to 3×10^{10} kHz/s were localized in a region limited by 1.5 dB of OSNR penalty for 16-QAM. In the case of 64-QAM, the penalty of these lasers are limited by a 2 dB. The same behavior is perceived for the remaining points. In addition, there is a laser associated with a OSNR penalty grater than 3 dB in the

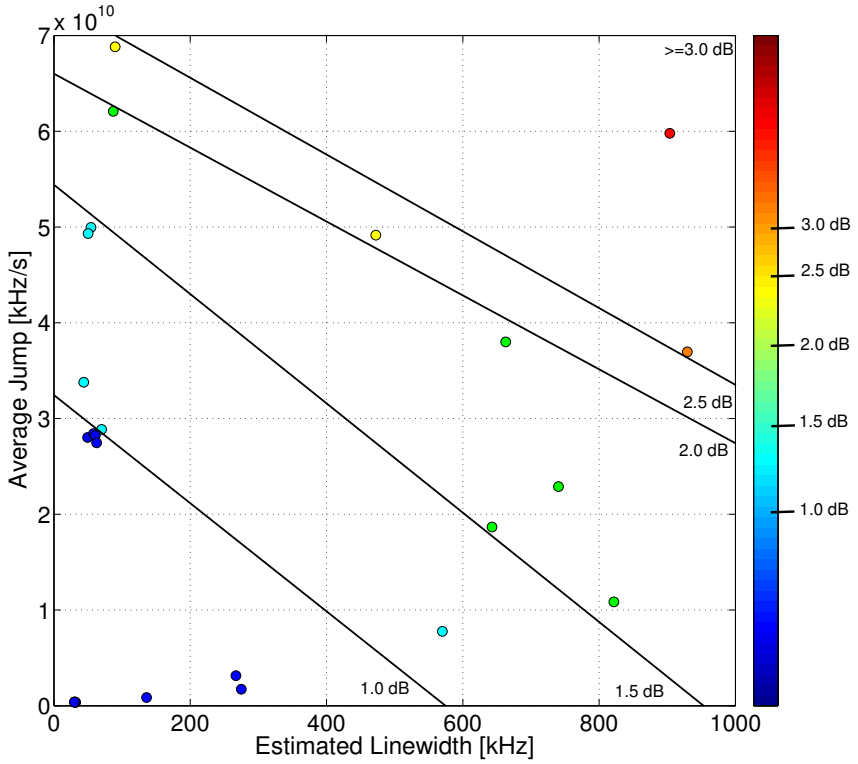

Figure 5.24 – Relation between laser linewidth estimate, average jump and OSNR penalty for 64-QAM coherent optical system.

64-QAM system. In a similar way, this color map allows forecasting the performance of a 64-QAM coherent system when an specific laser is used by means of the identification of regions limited by OSNR penalty thresholds. Once an approximate OSNR penalty is estimated, the laser can be characterized by finding the equivalent linewidth according to Sections 5.2.2 and 5.2.3.

Conclusions

Coherent optical communications systems are the current solution to keep up with the exponential growth of data traffic through the networks. Nevertheless, coherent systems are also subject to additional channel impairments. The use of two lasers in coherent systems gives rise to phase perturbations that degenerate the received signal. These phase perturbations come mainly from two laser imperfections, namely phase noise and fluctuations on the operating frequency, a phenomenon known as carrier frequency jitter (CFJ). As spectrally efficient modulation formats are more susceptible to phase perturbations, this work focused on evaluating the interplay of the laser imperfections and the performance of coherent systems with typical DSP algorithms for high-order modulation formats.

First, by simulations, the results evidenced that the OSNR penalty in a QPSK, 16-QAM and 64-QAM systems increase for higher laser linewidths and for an intensive CFJ. Performance values were obtained assuming Wiener phase noise and a sinusoidal CFJ. Later, from experimental data, we confirmed that high levels of laser imperfections critically degrade the system performance. In addition, it was shown that predicting the impact of laser imperfections on the system performance requires correlating linewidth estimation metrics with CFJ metrics. We proposed to use offset jumps between symbol sequences as a measure for CFJ.

The contributions of this thesis motivate future works to evaluate the impact of laser imperfections on a higher order modulation formats, such as as 256-QAM. On the other hand, it would be interesting to evaluate other techniques for linewidth estimation in a higher CFJ context. In addition, in future works, the robustness of the performance forecasting tools can be validated with the inclusion of additional lasers typically used in industry. Finally, as CFJ compensation was carried out through a modification of a well-known frequency recovery algorithm, novel techniques for frequency offset tracking can be developed based on the behavior of the frequency fluctuations revealed in our work.

Publications

Impact of Carrier Frequency Jitter on the Performance of Coherent Optical Systems with High-Order Modulation Formats. R. Bravo, J. D. Reis, D. A. A. Mello. Paper published in the VII Symposium of Signal Processing, Federal University of ABC, São Bernardo do Campo, SP, 2017.

Bibliography

ABRAR, S.; NANDI, A. K. Blind equalization of square-qam signals: a multimodulus approach. *IEEE Transactions on Communications*, v. 58, n. 6, p. 1674–1685, June 2010. ISSN 0090-6778. Cited on page 53.

AGRAWAL, G. P. *Fiber-Optic Communications Systems*. Third. [S.l.]: A JOHN WILEY AND SONS, 2002. Cited 16 times on pages 17, 34, 36, 37, 38, 39, 40, 42, 44, 45, 50, 57, 58, 59, 60, and 61.

AKIBA, S.; SAKAI, K.; MATSUSHIMA, Y.; YAMAMOTO, T. Room temperature cw operation of ingaasp/inp heterostructure lasers emitting at 1.56 μm. *Electronics Letters*, IET, v. 15, n. 19, p. 606–607, 1979. Cited on page 55.

ARNOLD, K. M.; MAYBURG, S. Cylindrical gaas laser diode. *Journal of Applied Physics*, AIP, v. 34, n. 10, p. 3136–3136, 1963. Cited on page 55.

BAGAD, V. S. *Optical Fiber Communications*. First. [S.l.]: Technical Publications Pune, 2007. Cited on page 38.

BANOVIC, K.; ABDEL-RAHEEM, E.; KHALID, M. A. S. A novel radius-adjusted approach for blind adaptive equalization. *IEEE Signal Processing Letters*, v. 13, n. 1, p. 37–40, Jan 2006. ISSN 1070-9908. Cited on page 53.

BARRY, J. R.; LEE, E. A.; MESSERSCHMITT, D. G. *Digital Communications*. Third. [S.l.]: Kluwer Academic Publishers, 2004. Cited 3 times on pages 31, 33, and 37.

BRILLOUIN, L. Diffusion de la lumiere et des rayons x par un corps transparent homogene: Influence de l'agitation thermique. *Annals of Physics*, v. 9, n. 17, p. 88–122, 1922. Cited on page 42.

CANTOR, G. N. *Optics after Newton: theories of light in Britain and Ireland, 1704-1840*. [S.l.]: Manchester University Press, 1983. Cited on page 39.

CHEN, X.; AMIN, A. A.; SHIEH, W. Characterization and monitoring of laser linewidths in coherent systems. *Journal of Lightwave Technology*, v. 29, n. 17, p. 2533–2537, Sept 2011. ISSN 0733-8724. Cited 2 times on pages 25 and 89.

DAWSON, J. W.; PARK, N.; VAHALA, K. J. An improved delayed self-heterodyne interferometer for linewidth measurements. *IEEE Photonics Technology Letters*, v. 4, n. 9, p. 1063–1066, Sept 1992. ISSN 1041-1135. Cited on page 25.

DEMTRöDER, W. *Atoms, molecules and photons: An introduction to atomic-, molecular- and quantum-physics*. 1. ed. Springer, 2005. ISBN 3-540-20631-0. Disponível em: <http://gen.lib.rus.ec/book/index.php?md5=F781822CB3B31D7F375ABDD694AECEDE>. Cited 2 times on pages 36 and 56.

DESURVIRE, E.; GILES, C.; SIMPSON, J.; ZYSKIND, J. *Erbium-doped fiber amplifier*. Google Patents, 1991. US Patent 5,005,175. Disponível em: <https://www.google.com/patents/US5005175>. Cited on page 24.

DUTHEL, T.; CLARICI, G.; FLUDGER, C. R. S.; GEYER, J. C.; SCHULIEN, C.; WIESE, S. Laser linewidth estimation by means of coherent detection. *IEEE Photonics Technology Letters*, v. 21, n. 20, p. 1568–1570, Oct 2009. ISSN 1041-1135. Cited on page 25.

DYMENT, J.; RIPPER, J. Temperature behavior of stimulated emission delays in gaas diodes and a proposed trapping model. *IEEE Journal of Quantum Electronics*, v. 4, n. 4, p. 155–160, April 1968. ISSN 0018-9197. Cited on page 55.

DZIEDZIC, J. M.; STOLEN, R. H.; ASHKIN, A. Optical kerr effect in long fibers. *Appl. Opt.*, OSA, v. 20, n. 8, p. 1403–1406, Apr 1981. Disponível em: <http://ao.osa.org/abstract.cfm?URI=ao-20-8-1403>. Cited on page 42.

ESSIAMBRE, R. J.; KRAMER, G.; WINZER, P. J.; FOSCHINI, G. J.; GOEBEL, B. Capacity limits of optical fiber networks. *Journal of Lightwave Technology*, v. 28, n. 4, p. 662–701, Feb 2010. ISSN 0733-8724. Cited on page 37.

ESSIAMBRE, R. J.; TKACH, R. W. Capacity trends and limits of optical communication networks. *Proceedings of the IEEE*, v. 100, n. 5, p. 1035–1055, May 2012. ISSN 0018-9219. Cited on page 37.

ETTENBERG, M. Very low-threshold double-heterojunction al x ga1- x as injection lasers. *Applied Physics Letters*, AIP, v. 27, n. 12, p. 652–654, 1975. Cited on page 55.

FARJADY, F.; PARKER, M. *Wavelength division multiplexing*. Google Patents, 2002. US Patent 6,339,664. Disponível em: <https://www.google.com/patents/US6339664>. Cited on page 24.

FARUK, M. S.; SAVORY, S. J. Digital signal processing for coherent transceivers employing multilevel formats. *J. Lightwave Technol.*, OSA, v. 35, n. 5, p. 1125–1141, Mar 2017. Disponível em: <http://jlt.osa.org/abstract.cfm?URI=jlt-35-5-1125>. Cited 4 times on pages 48, 62, 63, and 64.

FATADIN, I.; IVES, D.; SAVORY, S. J. Blind equalization and carrier phase recovery in a 16-qam optical coherent system. *J. Lightwave Technol.*, OSA, v. 27, n. 15, p. 3042–3049, Aug 2009. Disponível em: <http://jlt.osa.org/abstract.cfm?URI=jlt-27-15-3042>. Cited 2 times on pages 51 and 53.

FATADIN, I.; IVES, D.; SAVORY, S. J. Compensation of frequency offset for differentially encoded 16- and 64-qam in the presence of laser phase noise. *IEEE Photonics Technology Letters*, v. 22, n. 3, p. 176–178, Feb 2010. ISSN 1041-1135. Cited on page 30.

FATADIN, I.; SAVORY, S. J.; IVES, D. Compensation of quadrature imbalance in an optical qpsk coherent receiver. *IEEE Photonics Technology Letters*, v. 20, n. 20, p. 1733–1735, Oct 2008. ISSN 1041-1135. Cited on page 48.

FAVRE, F.; GUEN, D. le; SIMON, J. C.; LANDOUSIES, B. External-cavity semiconductor laser with 15 nm continuous tuning range. *Electronics Letters*, v. 22, n. 15, p. 795–796, July 1986. ISSN 0013-5194. Cited on page 60.

FERREIRA, H. B. *Algoritmos de recuperação de fase para Sistemas ópticos com modulação DP-QPSK*. Dissertação (Mestrado) — University of Brasilia, Brazil, 2011. Cited on page 68.

FERREIRA, R. M. da S. *Advanced Digital Signal Processing for Flexible Optical Access Networks*. Tese (Doutorado) — University of Aveiro, Portugal, 2017. Cited 3 times on pages 26, 62, and 64.

FILHO, J. M.; SILVA, M. T. M.; MIRANDA, M. D. A family of algorithms for blind equalization of qam signals. In: *2011 IEEE International Conference on Acoustics, Speech and Signal Processing (ICASSP)*. [S.l.: s.n.], 2011. p. 3388–3391. ISSN 1520-6149. Cited on page 54.

FLEMING, M.; MOORADIAN, A. Spectral characteristics of external-cavity controlled semiconductor lasers. *IEEE Journal of Quantum Electronics*, v. 17, n. 1, p. 44–59, Jan 1981. ISSN 0018-9197. Cited on page 59.

GALTAROSSA, C. R. M. A. *Polarization Mode Dispersion*. First. [S.l.]: Springer, 2005. Cited on page 40.

GIANNI, P.; CORRAL-BRIONES, G.; RODRIGUEZ, C.; HUEDA, M. R. Compensation of laser frequency fluctuations and phase noise in 16-qam coherent receivers. *IEEE Photonics Technology Letters*, v. 25, n. 5, p. 442–445, March 2013. ISSN 1041-1135. Cited 2 times on pages 26 and 72.

GIANNI, P.; CORRAL-BRIONES, G.; RODRIGUEZ, C. E.; CARRER, H. S.; HUEDA, M. R. A new parallel carrier recovery architecture for intradyne coherent optical receivers in the presence of laser frequency fluctuations. In: *2011 IEEE Global Telecommunications Conference - GLOBECOM 2011*. [S.l.: s.n.], 2011. p. 1–6. ISSN 1930-529X. Cited 3 times on pages 26, 62, and 72.

GODARD, D. Self-recovering equalization and carrier tracking in two-dimensional data communication systems. *IEEE Transactions on Communications*, v. 28, n. 11, p. 1867–1875, Nov 1980. ISSN 0090-6778. Cited 2 times on pages 50 and 51.

GOLDBERG, P.; MILONNI, P. W.; SUNDARAM, B. Theory of the fundamental laser linewidth. *Phys. Rev. A*, American Physical Society, v. 44, p. 1969–1985, Aug 1991. Disponível em: <https://link.aps.org/doi/10.1103/PhysRevA.44.1969>. Cited on page 62.

GOLDFARB, G.; LI, G. Chromatic dispersion compensation using digital iir filtering with coherent detection. *IEEE Photonics Technology Letters*, v. 19, n. 13, p. 969–971, July 2007. ISSN 1041-1135. Cited on page 50.

GRUNER-NIELSEN, L.; WANDEL, M.; KRISTENSEN, P.; JORGENSEN, C.; JORGENSEN, L. V.; EDVOLD, B.; PALSDOTTIR, B.; JAKOBSEN, D. Dispersion-compensating fibers. *Journal of Lightwave Technology*, v. 23, n. 11, p. 3566–3579, Nov 2005. ISSN 0733-8724. Cited on page 40.

HALL, R. N.; FENNER, G. E.; KINGSLEY, J. D.; SOLTYS, T. J.; CARLSON, R. O. Coherent light emission from gaas junctions. *Phys. Rev. Lett.*, American Physical Society, v. 9, p. 366–368, Nov 1962. Disponível em: <https://link.aps.org/doi/10.1103/PhysRevLett.9.366>. Cited on page 55.

HAYKIN, S. *Communication Systems*. 4th ed. ed. Wiley, 2001. ISBN 0-471-17869-1. Disponível em: <http://gen.lib.rus.ec/book/index.php?md5=0D7B2D4C12E3B9C37D94EDCFF4698458>. Cited 3 times on pages 28, 32, and 37.

HAYKIN, S. *Adaptive Filter Theory*. Fifth. [S.l.]: Pearson, 2014. Cited on page 50.

HENRY, C. Theory of the linewidth of semiconductor lasers. *IEEE Journal of Quantum Electronics*, v. 18, n. 2, p. 259–264, February 1982. ISSN 0018-9197. Cited on page 61.

HENRY, C. Theory of the phase noise and power spectrum of a single mode injection laser. *IEEE Journal of Quantum Electronics*, v. 19, n. 9, p. 1391–1397, Sep 1983. ISSN 0018-9197. Cited on page 60.

HENRY, C. Phase noise in semiconductor lasers. *Journal of Lightwave Technology*, v. 4, n. 3, p. 298–311, Mar 1986. ISSN 0733-8724. Cited on page 61.

HO, K.-P. *Phase-modulated optical communication systems*. 1. ed. Springer, 2005. ISBN 0387243925,9780387243924,0387255559,9780387255552. Disponível em: <http://gen.lib.rus.ec/book/index.php?md5=140B9EF4374170A4974A3C20474AD7E6>. Cited on page 46.

HOFFMANN, S.; BHANDARE, S.; PFAU, T.; ADAMCZYK, O.; WORDEHOFF, C.; PEVELING, R.; PORRMANN, M.; NOE, R. Frequency and phase estimation for coherent qpsk transmission with unlocked dfb lasers. *IEEE Photonics Technology Letters*, v. 20, n. 18, p. 1569–1571, Sept 2008. ISSN 1041-1135. Cited 2 times on pages 26 and 62.

HOFFMANN, S.; BHANDARE, S.; PFAU, T.; ADAMCZYK, O.; WORDEHOFF, C.; PEVELING, R.; PORRMANN, M.; NOE, R. Frequency and phase estimation for coherent qpsk transmission with unlocked dfb lasers. *IEEE Photonics Technology Letters*, v. 20, n. 18, p. 1569–1571, Sept 2008. ISSN 1041-1135. Cited on page 62.

HSIEH, J.; ROSSI, J.; DONNELLY, J. Room-temperature cw operation of gainasp/inp double-heterostructure diode lasers emitting at 1.1 μ m. *Applied Physics Letters*, AIP, v. 28, n. 12, p. 709–711, 1976. Cited on page 55.

HUTTNER, B. Differential group delay. *Fiber Measurements, 1998*, v. 1, p. 49, 1998. Cited on page 41.

HUYNH, T. N.; NGUYEN, L.; BARRY, L. P. Delayed self-heterodyne phase noise measurements with coherent phase modulation detection. *IEEE Photonics Technology Letters*, v. 24, n. 4, p. 249–251, Feb 2012. ISSN 1041-1135. Cited 3 times on pages 25, 83, and 90.

IP, E.; KAHN, J. M. Feedforward carrier recovery for coherent optical communications. *Journal of Lightwave Technology*, v. 25, n. 9, p. 2675–2692, Sept 2007. ISSN 0733-8724. Cited on page 68.

J. D. Reis et al. *Technology Options for 400G Implementation*. [S.l.], 2015. Cited on page 77.

JOHNSON, R.; SCHNITER, P.; ENDRES, T. J.; BEHM, J. D.; BROWN, D. R.; CASAS, R. A. Blind equalization using the constant modulus criterion: a review. *Proceedings of the IEEE*, v. 86, n. 10, p. 1927–1950, Oct 1998. ISSN 0018-9219. Cited on page 51.

JONES, R. C. A new calculus for the treatment of optical systems. iv. *J. Opt. Soc. Am.*, OSA, v. 32, n. 8, p. 486–493, Aug 1942. Disponível em: <http://www.osapublishing.org/abstract.cfm?URI=josa-32-8-486>. Cited on page 41.

KAKKAR., A. Laser frequency noise in coherent optical systems: Spectral regimes and impairments. 2017. Disponível em: <https://www-ncbi-nlm-nih-gov.ez88.periodicos.capes.gov.br/pmc/articles/PMC5429818/>. Cited on page 90.

KAMINOW, I. P.; NAHORY, R. E.; POLLACK, M. A.; STULZ, L. W.; DEWINTER, J. C. Single-mode c.w. ridge-waveguide laser emitting at 1.55 Â¿m. *Electronics Letters*, v. 15, n. 23, p. 763–765, November 1979. ISSN 0013-5194. Cited on page 55.

KEISER, G. *Optical fiber communications*. 3. ed. McGraw-Hill, 2000. ISBN 0072360763,9780072360769. Disponível em: <http://gen.lib.rus.ec/book/index.php?md5=5E42449649FCA219A2E013AACF8E96D4>. Cited on page 38.

KERR, J. Liv. a new relation between electricity and light: Dielectrified media birefringent (second paper). *The London, Edinburgh, and Dublin Philosophical Magazine and Journal of Science*, Taylor & Francis, v. 50, n. 333, p. 446–458, 1875. Cited on page 42.

KIKUCHI, K. Effect of 1/f-type fm noise on semiconductor-laser linewidth residual in high-power limit. *IEEE Journal of Quantum Electronics*, v. 25, n. 4, p. 684–688, Apr 1989. ISSN 0018-9197. Cited 2 times on pages 90 and 92.

KIKUCHI, K.; IGARASHI, K. Characterization of semiconductor-laser phase noise with digital coherent receivers. In: *2011 Optical Fiber Communication Conference and Exposition and the National Fiber Optic Engineers Conference*. [S.l.: s.n.], 2011. p. 1–3. ISSN pending. Cited 2 times on pages 88 and 90.

KIM, J. W.; HAHN, J. W.; YOO, Y. S.; LEE, J. Y.; KONG, H. J.; LEE, H.-W. Measurement of the linewidth of a continuous-wave laser with a cavity-length modulation technique. *Appl. Opt.*, OSA, v. 38, n. 9, p. 1742–1745, Mar 1999. Disponível em: <http://ao.osa.org/abstract.cfm?URI=ao-38-9-1742>. Cited on page 25.

KOGELNIK, H.; SHANK, C. Coupled-wave theory of distributed feedback lasers. *Journal of applied physics*, AIP, v. 43, n. 5, p. 2327–2335, 1972. Cited on page 58.

KOJIMA, K.; HORIGUCHI, Y.; KOIKE-AKINO, T.; SHIMAKURA, Y.; ENOKI, K.; YAGYU, E. Separation of semiconductor laser intrinsic linewidth and 1/f noise using multiple fiber lengths with the delayed self-heterodyne method. In: *2015 Optical Fiber Communications Conference and Exhibition (OFC)*. [S.l.: s.n.], 2015. p. 1–3. Cited 2 times on pages 25 and 92.

KRUGER, U.; PETERMANN, K. The semiconductor laser linewidth due to the presence of side modes. *IEEE Journal of Quantum Electronics*, v. 24, n. 12, p. 2355–2358, Dec 1988. ISSN 0018-9197. Cited on page 61.

KUSCHNEROV, M.; HAUSKE, F. N.; PIYAWANNO, K.; SPINNLER, B.; NAPOLI, A.; LANKL, B. Adaptive chromatic dispersion equalization for non-dispersion managed coherent systems. In: *2009 Conference on Optical Fiber Communication - incudes post deadline papers*. [S.l.: s.n.], 2009. p. 1–3. Cited on page 50.

KUSCHNEROV, M.; HAUSKE, F. N.; PIYAWANNO, K.; SPINNLER, B.; ALFIAD, M. S.; NAPOLI, A.; LANKL, B. Dsp for coherent single-carrier receivers. *J. Lightwave Technol.*, OSA, v. 27, n. 16, p. 3614–3622, Aug 2009. Disponível em: <http://jlt.osa.org/abstract.cfm?URI=jlt-27-16-3614>. Cited 3 times on pages 49, 50, and 68.

KUSCHNEROV, M.; PIYAWANNO, K.; ALFIAD, M. S.; SPINNLER, B.; NAPOLI, A.; LANKL, B. Impact of mechanical vibrations on laser stability and carrier phase estimation in coherent receivers. *IEEE Photonics Technology Letters*, v. 22, n. 15, p. 1114–1116, Aug 2010. ISSN 1041-1135. Cited 2 times on pages 26 and 72.

LAVERY, D.; PASKOV, M.; MAHER, R.; SAVORY, S. J.; BAYVEL, P. Modified radius directed equaliser for high order qam. In: *2015 European Conference on Optical Communication (ECOC)*. [S.l.: s.n.], 2015. p. 1–3. Cited on page 54.

LEVEN, A.; KANEDA, N.; KOC, U.-V.; CHEN, Y.-K. Frequency estimation in intradyne reception. *IEEE Photonics Technology Letters*, v. 19, n. 6, p. 366–368, March 2007. Cited 2 times on pages 43 and 64.

LI, J.; LI, L.; TAO, Z.; HOSHIDA, T.; RASMUSSEN, J. C. Laser-linewidth-tolerant feed-forward carrier phase estimator with reduced complexity for qam. *Journal of Lightwave Technology*, v. 29, n. 16, p. 2358–2364, Aug 2011. ISSN 0733-8724. Cited 2 times on pages 70 and 71.

LUDVIGSEN, H.; TOSSAVAINEN, M.; KAIVOLA, M. Laser linewidth measurements using self-homodyne detection with short delay. *Optics Communications*, v. 155, n. 1, p. 180 – 186, 1998. ISSN 0030-4018. Disponível em: <http://www.sciencedirect.com/science/article/pii/S0030401898003551>. Cited 3 times on pages 25, 83, and 84.

MAGARINI, M.; BARLETTA, L.; SPALVIERI, A.; VACONDIO, F.; PFAU, T.; PEPE, M.; BERTOLINI, M.; GAVIOLI, G. Pilot-symbols-aided carrier-phase recovery for 100-g pm-qpsk digital coherent receivers. *IEEE Photonics Technology Letters*, v. 24, n. 9, p. 739–741, May 2012. ISSN 1041-1135. Cited on page 67.

MAHER, R.; THOMSEN, B. Dynamic linewidth measurement technique using digital intradyne coherent receivers. *Opt. Express*, OSA, v. 19, n. 26, p. B313–B322, Dec 2011. Disponível em: <http://www.opticsexpress.org/abstract.cfm?URI=oe-19-26-B313>. Cited 2 times on pages 25 and 89.

MATSUDA, K.; BESSHO, H.; HASEGAWA, K.; YOSHIDA, T.; ISHIDA, K. A study of laser white and brownian fm noise in coherent qpsk signals. In: *OFC 2014*. [S.l.: s.n.], 2014. p. 1–3. Cited on page 82.

MEYR, H.; MOENECLAEY, M.; FECHTEL, S. A. *Digital Communication Receivers*. First. [S.l.]: John Wiley and Sons, Inc., 1998. Cited 3 times on pages 29, 30, and 67.

MILLAR, D. S.; MAHER, R.; LAVERY, D.; KOIKE-AKINO, T.; PAJOVIC, M.; ALVARADO, A.; PASKOV, M.; KOJIMA, K.; PARSONS, K.; THOMSEN, B. C.; SAVORY, S. J.; BAYVEL, P. Design of a 1 tb/s superchannel coherent receiver. *Journal of Lightwave Technology*, v. 34, n. 6, p. 1453–1463, March 2016. ISSN 0733-8724. Cited on page 67.

MOORADIAN, A. *External cavity semiconductor laser*. [S.l.]: Google Patents, 1991. US Patent 5,050,179. Cited on page 60.

MROZIEWICZ, B.; BUGAJSKI, M.; NAKWASKI, W. *Physics of semiconductor lasers*. [S.l.]: Elsevier, 2017. Cited on page 58.

NAGAYAMA, K.; KAKUI, M.; MATSUI, M.; SAITOH, I.; CHIGUSA, Y. Ultra-low-loss (0.1484 db/km) pure silica core fibre and extension of transmission distance. *Electronics Letters*, v. 38, n. 20, p. 1168–1169, Sep 2002. ISSN 0013-5194. Cited on page 38.

OE, K.; ANDO, S.; SUGIYAMA, K. 1.3 µm cw operation of gainasp/inp dh diode lasers at room temperature. *Japanese Journal of Applied Physics*, v. 16, n. 7, p. 1273, 1977. Disponível em: <http://stacks.iop.org/1347-4065/16/i=7/a=1273>. Cited on page 55.

OKOSHI, T.; KIKUCHI, K. *Coherent optical fiber communications*. [S.l.]: Springer Science & Business Media, 1988. v. 4. Cited on page 42.

OKOSHI, T.; KIKUCHI, K.; NAKAYAMA, A. Novel method for high resolution measurement of laser output spectrum. *Electronics Letters*, v. 16, n. 16, p. 630–631, July 1980. ISSN 0013-5194. Cited on page 25.

OLMEDO, M. I.; PANG, X.; SCHATZ, R.; OZOLINS, O.; LOUCHET, H.; ZIBAR, D.; JACOBSEN, G.; MONROY, I. T.; POPOV, S. Effective linewidth of semiconductor lasers for coherent optical data links. *Photonics*, v. 3, n. 2, 2016. Cited on page 90.

O'MAHONY, M. J.; HENNING, I. D. Semiconductor laser linewidth broadening due to 1/f carrier noise. *Electronics Letters*, v. 19, n. 23, p. 1000–1001, November 1983. ISSN 0013-5194. Cited on page 62.

OU, N.; FARAHMAND, T.; KUO, A.; TABATABAEI, S.; IVANOV, A. Jitter models for the design and test of gbps-speed serial interconnects. *IEEE Design Test of Computers*, v. 21, n. 4, p. 302–313, July 2004. ISSN 0740-7475. Cited on page 62.

PAJOVIC, M.; MILLAR, D.; KOIKE-AKINO, T.; KOJIMA, K.; ARLUNNO, V.; PARSONS, K. Multi-pilot aided carrier phase estimation for single carrier coherent systems. In: *Advanced Photonics 2015*. Optical Society of America, 2015. p. SpT4D.4. Disponível em: <http://www.osapublishing.org/abstract.cfm?URI=SPPCom-2015-SpT4D.4>. Cited on page 67.

PANISH, M. B.; HAYASHI, I.; SUMSKI, S. Double-heterostructure injection lasers with room-temperature thresholds as low as 2300 a/cm2. *Applied Physics Letters*, v. 16, n. 8, p. 326–327, 1970. Disponível em: <https://doi.org/10.1063/1.1653213>. Cited on page 55.

PAULI, W. Einstein's contribution to quantum theory. *Enz C.P., von Meyenn K. (eds) Writings on Physics and Philosophy*, 1994. Cited on page 36.

PFAU, T. *Development and real-time implementation of digital signal processing algorithms for coherent optical receivers*. Tese (Doutorado) — Paderborn University, 2009. Cited on page 69.

PFAU, T.; HOFFMANN, S.; NOE, R. Hardware-efficient coherent digital receiver concept with feedforward carrier recovery for m -qam constellations. *Journal of Lightwave Technology*, v. 27, n. 8, p. 989–999, April 2009. ISSN 0733-8724. Cited 4 times on pages 30, 64, 66, and 70.

PIELS, M.; OLMEDO, M. I.; XUE, W.; PANG, X.; SCHäFFER, C.; SCHATZ, R.; JACOBSEN, G.; MONROY, I. T.; MØRK, J.; POPOV, S.; ZIBAR, D. Laser rate equation-based filtering for carrier recovery in characterization and communication.

J. Lightwave Technol., OSA, v. 33, n. 15, p. 3271–3279, Aug 2015. Disponível em: <http://jlt.osa.org/abstract.cfm?URI=jlt-33-15-3271>. Cited 2 times on pages 86 and 90.

PIYAWANNO, K.; KUSCHNEROV, M.; ALFIAD, M. S.; SPINNLER, B.; LANKL, B. Effects of mechanical disturbance on local oscillators and carrier synchronization. In: *OECC 2010 Technical Digest*. [S.l.: s.n.], 2010. p. 124–125. ISSN 2166-8884. Cited 2 times on pages 26 and 72.

POOLE, C. D.; WAGNER, R. E. Phenomenological approach to polarisation dispersion in long single-mode fibres. *Electronics Letters*, v. 22, n. 19, p. 1029–1030, September 1986. ISSN 0013-5194. Cited on page 40.

QIU, M.; ZHUGE, Q.; XU, X.; CHAGNON, M.; MORSY-OSMAN, M.; PLANT, D. V. Simple and efficient frequency offset tracking and carrier phase recovery algorithms in single carrier transmission systems. *Opt. Express*, OSA, v. 21, n. 7, p. 8157–8165, Apr 2013. Disponível em: <http://www.opticsexpress.org/abstract.cfm?URI=oe-21-7-8157>. Cited 2 times on pages 26 and 72.

RAMACHANDRAN, S. *Fiber based dispersion compensation*. 1. ed. Springer, 2007. (Optical and fiber communications reports 5). ISBN 0387403477,9780387403472,9780387489483. Disponível em: <http://gen.lib.rus.ec/book/index.php?md5=1AC1A2D0E1A919DD56FEBB97828E6C6A>. Cited on page 24.

RAMAN, C. V. A change of wave-length in light scattering. *Nature*, v. 121, p. 619, April 1928. Cited on page 42.

RAMASWAMI, R.; SIVARAJAN, K. N.; SASAKI, G. H. *Optical Networks, A Practical Perspective*. Third. [S.l.]: ELSEVIER Inc, 2010. Cited 9 times on pages 17, 34, 36, 39, 42, 57, 58, 59, and 60.

RASHLEIGH, S. C.; ULRICH, R. Polarization mode dispersion in single-mode fibers. *Opt. Lett.*, OSA, v. 3, n. 2, p. 60–62, Aug 1978. Disponível em: <http://ol.osa.org/abstract.cfm?URI=ol-3-2-60>. Cited on page 40.

READY, M. J.; GOOCH, R. P. Blind equalization based on radius directed adaptation. In: *International Conference on Acoustics, Speech, and Signal Processing*. [S.l.: s.n.], 1990. p. 1699–1702 vol.3. ISSN 1520-6149. Cited on page 53.

RICHTER, L.; MANDELBERG, H.; KRUGER, M.; MCGRATH, P. Linewidth determination from self-heterodyne measurements with subcoherence delay times. *IEEE Journal of Quantum Electronics*, v. 22, n. 11, p. 2070–2074, Nov 1986. ISSN 0018-9197. Cited 2 times on pages 85 and 88.

RIPPER, J. E.; LEITE, R. C. C. Tunneling-assisted radiative recombination in gaas-diffused junctions. *Proceedings of the IEEE*, v. 53, n. 2, p. 160–160, Feb 1965. ISSN 0018-9219. Cited on page 55.

ROMANO, J. M. T.; ATTUX, R. de F.; CAVALCANTE, C. C.; SUYAMA, R. *Unsupervised Signal Processing: Channel Equalization and Source Separation*. 1. ed. CRC Press, 2010. ISBN 0849337518,9780849337512. Disponível em: <http://gen.lib.rus.ec/book/index.php?md5=99ED9EEB3170E9E34B3312109050B677>. Cited on page 50.

SABRA, A. I. *Theories of Light - From Descartes to Newton*. Cambridge University Press, 1981. ISBN 9780521284363. Disponível em: <http://gen.lib.rus.ec/book/index.php?md5=3240E97754F9312E8DBCB224921D50C2>. Cited on page 39.

SALEH, M. C. T. B. E. A. *Fundamentals of photonics*. 1st. ed. Wiley, 1991. (Wiley series in pure and applied optics). ISBN 0471839655,9780585321479,9780471839651. Disponível em: <http://gen.lib.rus.ec/book/index.php?md5=323CF22AA48243FC4ADAB2D63E31EE60>. Cited 2 times on pages 38 and 49.

SAVORY, S. J. Digital filters for coherent optical receivers. *Opt. Express*, OSA, v. 16, n. 2, p. 804–817, Jan 2008. Disponível em: <http://www.opticsexpress.org/abstract.cfm?URI=oe-16-2-804>. Cited 2 times on pages 49 and 50.

SAVORY, S. J. Digital coherent optical receivers: Algorithms and subsystems. *IEEE Journal of Selected Topics in Quantum Electronics*, v. 16, n. 5, p. 1164–1179, Sept 2010. ISSN 1077-260X. Cited 2 times on pages 53 and 68.

SAYED, A. H. *Adaptive Filters*. First. [S.l.]: John Wiley and Sons, Inc., 2008. Cited on page 51.

SCHAWLOW, A. L.; TOWNES, C. H. Infrared and optical masers. *Phys. Rev.*, American Physical Society, v. 112, p. 1940–1949, Dec 1958. Disponível em: <https://link.aps.org/doi/10.1103/PhysRev.112.1940>. Cited on page 55.

SELMI, M.; JAOUEN, Y.; CIBLAT, P. Accurate digital frequency offset estimator for coherent polmux qam transmission systems. In: *2009 35th European Conference on Optical Communication*. [S.l.: s.n.], 2009. p. 1–2. ISSN 1550-381X. Cited 2 times on pages 26 and 62.

SHAPIRO, A. E. Newton's definition of a light ray and the diffusion theories of chromatic dispersion. *The University of Chicago Press Journals*, v. 66, n. 2, p. 194–210, June 1975. Cited on page 39.

SJOLANDER, J. *Equalization of Fiber Optic Channels*. [S.l.], 2011. Cited on page 52.

SPALVIERI, A.; BARLETTA, L. Pilot-aided carrier recovery in the presence of phase noise. *IEEE Transactions on Communications*, v. 59, n. 7, p. 1966–1974, July 2011. ISSN 0090-6778. Cited on page 67.

SPINNLER, B.; HAUSKE, F. N.; KUSCHNEROV, M. Adaptive equalizer complexity in coherent optical receivers. In: *2008 34th European Conference on Optical Communication*. [S.l.: s.n.], 2008. p. 1–2. ISSN 1550-381X. Cited on page 50.

SUNTER, S.; ROY, A. On-chip digital jitter measurement, from megahertz to gigahertz. *IEEE Design Test of Computers*, v. 21, n. 4, p. 314–321, July 2004. ISSN 0740-7475. Cited on page 62.

SUTILI, T.; FIGUEIREDO, R. C.; CONFORTI, E. Laser linewidth and phase noise evaluation using heterodyne offline signal processing. *J. Lightwave Technol.*, OSA, v. 34, n. 21, p. 4933–4940, Nov 2016. Disponível em: <http://jlt.osa.org/abstract.cfm?URI=jlt-34-21-4933>. Cited on page 25.

TROPPER, A. C.; FOREMAN, H. D.; GARNACHE, A.; WILCOX, K. G.; HOOGLAND, S. H. Vertical-external-cavity semiconductor lasers. *Journal of Physics D: Applied Physics*, v. 37, n. 9, p. R75, 2004. Disponível em: <http://stacks.iop.org/0022-3727/37/i=9/a=R01>. Cited on page 60.

TSUCHIDA, H. Simple technique for improving the resolution of the delayed self-heterodyne method. *Opt. Lett.*, OSA, v. 15, n. 11, p. 640–642, Jun 1990. Disponível em: <http://ol.osa.org/abstract.cfm?URI=ol-15-11-640>. Cited on page 25.

VITERBI, A.; VITERBI, A. Nonlinear estimation of psk-modulated carrier phase with application to burst digital transmission. *IEEE Transactions on Information Theory*, v. 29, n. 4, p. 543–551, July 1983. ISSN 0018-9448. Cited 2 times on pages 67 and 68.

WEI, X.; XIAONIU, Y.; ZHAOYANG, Z. A variable step size blind equalization algorithm for qam signals. In: *2010 International Conference on Microwave and Millimeter Wave Technology*. [S.l.: s.n.], 2010. p. 1801–1804. Cited on page 53.

WEINBERGER, P. John kerr and his effects found in 1877 and 1878. *Philosophical Magazine Letters*, Taylor & Francis, v. 88, n. 12, p. 897–907, 2008. Cited on page 42.

WINFUL, H. G. Polarization instabilities in birefringent nonlinear media: application to fiber-optic devices. *Opt. Lett.*, OSA, v. 11, n. 1, p. 33–35, Jan 1986. Disponível em: <http://ol.osa.org/abstract.cfm?URI=ol-11-1-33>. Cited on page 50.

XU, T.; JACOBSEN, G.; POPOV, S.; LI, J.; VANIN, E.; WANG, K.; FRIBERG, A. T.; ZHANG, Y. Chromatic dispersion compensation in coherent transmission system using digital filters. *Opt. Express*, OSA, v. 18, n. 15, p. 16243–16257, Jul 2010. Disponível em: <http://www.opticsexpress.org/abstract.cfm?URI=oe-18-15-16243>. Cited 2 times on pages 49 and 50.

YEN, H.; NAKAMURA, M.; GARMIRE, E.; SOMEKH, S.; YARIV, A.; GARVIN, H. Optically pumped gaas waveguide lasers with a fundamental 0.11 μ corrugation feedback. *Optics Communications*, Elsevier, v. 9, n. 1, p. 35–37, 1973. Cited on page 58.

ZHANG, X. *Digital Signal Processing for Optical Coherent Communication Systems*. Tese (Doutorado) — Technical University of Denmark, Denmark, 2012. Cited 3 times on pages 17, 25, and 39.

ZHOU, W.; CHONG, K. M.; GUO, H. Linewidth measurement of littrow structure semiconductor laser with improved methods. *Physics Letters A*, v. 372, n. 23, p. 4327 – 4332, 2008. ISSN 0375-9601. Disponível em: <http://www.sciencedirect.com/science/article/pii/S0375960108004982>. Cited 4 times on pages 82, 84, 85, and 90.

ZHOU, X. Efficient clock and carrier recovery algorithms for single-carrier coherent optical systems: A systematic review on challenges and recent progress. *IEEE Signal Processing Magazine*, v. 31, n. 2, p. 35–45, March 2014. ISSN 1053-5888. Cited 3 times on pages 64, 65, and 70.

ZHOU, X.; YU, J.; HUANG, M.-F.; SHAO, Y.; WANG, T.; NELSON, L.; MAGILL, P.; BIRK, M.; BOREL, P. I.; PECKHAM, D. W.; LINGLE, R.; ZHU, B. 64-tb/s, 8 b/s/hz, pdm-36qam transmission over 320 km using both pre- and post-transmission digital signal processing. *J. Lightwave Technol.*, OSA, v. 29, n. 4, p. 571–577, Feb 2011. Disponível em: <http://jlt.osa.org/abstract.cfm?URI=jlt-29-4-571>. Cited on page 65.